TEMPERATURE DEPENDENCE OF DISLOCATION DYNAMICS DURING NANO-INDENTATION IN METALS

A thesis submitted in partial fulfillment of the requirements
for the Degree of Doctor of Philosophy

By

Rathinam Murugavel

Department of Electronic and Information Engineering

The Hong Kong Polytechnic University

June 2004

Certificate of Originality

I hereby declare that this thesis is my own work and that, to the best of my knowledge and belief, it reproduces no material previously published or written, nor material that has been accepted for the award of any other degree or diploma, except where due acknowledgement has been made in the text.

Rathinam Murugavel

Abstract

Temperature dictates mechanical properties of materials. In present day applications, materials are rarely utilized at room temperature alone. Meanwhile, temperatures may have drastic effects on the mechanical responses of materials, such as the deformation and fracture properties at different temperatures. Nanoscale testing of materials at non-ambient temperatures is now possible. The ability to perform nanotest measurements at elevated temperatures opens up significant new possibilities in nanotechnology. Sub-zero and high temperature analysis using nanoindentation technology is the first of its kind. Materials behave differently in real-life environments due to thermal loading. The objective of this thesis is to investigate the response of metals to nanoindentation at temperatures above and below the normal room temperature, using a combination of experiments and computer simulations. The metals studied include both face-center-cubic (FCC) and body-center-cubic (BCC) elements, and dislocation dynamics is the focus of this mechanics study.

The experiments are performed with tailor-made Berkovitch tip of radius 100 nm at temperatures of 265 K, 388 K, 348 K, 473 K and 623 K. Single-crystals of tungsten, gold, Aluminum and polycrystalline copper are considered for the investigation. The indentation is done for BCC tungsten on the (111) and (110) crystallographic surfaces, FCC gold on the (111) and (110) crystallographic surfaces, single crystal aluminum with (100) crystallographic orientation and polycrystalline copper at different temperatures. Both the

behaviour of material during loading and unloading are analyzed, and the processes are examined both experimentally and by computer simulations. Emphases are placed on the defects generation mechanisms during the elastic plastic contact of crystals. Special attention has been devoted to the elastic response before the onset of plastic yield.

The temperature dependency experiments and computer simulations yield very interesting results. The complete elastic range is found. The onset of the first burst is measured. The onset of plastic deformation is noticed from the periodic bursts. The strain hardening effects, softening effects, strain release effects are noticed at this temperature. Pile up is also noticed. The new phenomena of material under the indenter bouncing back at the end of unloading were clearly noticed. From the difference in penetration depth for different temperatures, it is noticed that there is significant increase in penetration depth at higher temperatures. The hardness and elastic modulus also dropped at higher temperatures. The results are also analyzed at different loading rate for various temperatures. A theory can be established in future for the relationship between the temperature and mechanical properties of metals helping in design and selecting suitable materials for real-life environments depending on the thermal loading.

Publications Arising from the Thesis

1. Murugavel, R., Woo, C. H., Hanchen Huang, Nano-indentation of copper at various temperatures (submitted to Journal of physics-condensed matter).
2. Murugavel, R., Woo, C. H., Hanchen Huang, property characterization of Tungsten under thermal loading (yet to be submitted)
3. Murugavel, R., Woo, C. H., Hanchen Huang, Effect of temperature on the properties of Gold (yet to be submitted).
4. Murugavel, R., Woo, C. H., Hanchen Huang, Temperature effects on aluminium during nano-indentation (yet to be submitted).

Acknowledgements

I would like to express my most grateful thanks to my Chief Supervisor, Prof. C. H. Woo, Chair professor of Solid-State Electronics for his invaluable guidance, timely encouragement, and great support throughout this research. His constant help influenced me greatly for the successful completion of this research. I am also most thankful and grateful to my Co-supervisor, Prof. Hanchen Huang of Rensselaer Polytechnic Institute for his guidance and support. I am also thankful to Prof. Alex P. K. Wai, Head of the Electronic and Information Engineering Department.

I take this opportunity to express my grateful thanks to Dr. Shi San Qiang, Associate Professor of Mechanical Engineering for his constant help and stimulating scientific discussions during this research. I am also thankful to my colleagues at HK Polytechnic University, and other Universities, whose names are too numerous to list here, for their constant support during this research.

Table of contents

List of Symbols and Abbreviations

h_c	Contact depth
h_{max}	Maximum depth
A	Projected contact area
$A(h_c)$	Tip area function
l	Horizontal distance
a	Contact radius
CL	Constant load testing method
C	Unloading slope
C_c	Contact compliance
C_m	Machine compliance of indentation testing system
C_{total}	Total compliance of the testing system
CRL	Constant rate of loading testing method
CRL/L	Constant ratio-of-load-rate-to-load testing method
D_{gb}	Grain boundary self-diffusion coefficient
D_{SD}	Self-diffusion coefficient through grain interior
E	Elastic modulus
E_i	Elastic modulus of the indenter
E_s	Elastic modulus of standard specimen
E_r	Reduced modulus (indentation modulus)
H	Hardness
h	Indentation displacement
h^{th}	Displacement due to thermal drift

P	Indentation load
P_{max}	Maximum indentation force
S	Contact stiffness
T	Temperature
t	Time
T_d	Thermal drift factor
T_m	Melting temperature
ν	Poisson's ratio
ν_s	Poisson's ratio of standard sample
ν_i	Poisson's ratio of indenter
μ	Shear modulus
τ	Shear stress
ε	Strain
σ	Stress
σ_i	Internal stress
σ_y	Yielding stress
T_o	Desired temperature
$T(t)$	Instantaneous temperature
K	Kinetic energy
b	Magnitude of burgers vector
R	Radius of the indenter
r	Distance of the substrate atom from indenter sphere center.
m_i	Atom mass
i	Atom i
F_i	Force acting upon each atom

a_i	Acceleration of each atom
s	Slip vector
k	Boltzmann constant
N	Total number of atoms
$U(n_i)$	Function giving the energy
x, X	Vectors linking the atom α with all its nearest neighbours β in the current and reference positions
n_s	Number of slipped neighbours
n	Number of nearest neighbours to atom α

Chapter 1 Introduction

On the night of April 24, 1912 the ship that many said to be unsinkable hit an iceberg and sunk about 2 hours and 40 minutes later. When the Titanic was built in 1912 it was the largest ship of its time with a length of 882 feet. On the maiden voyage the luxurious ship had 1320 Passengers and 907 crew members. If the right precautions were taken this disaster could have been avoided and many lives saved. Many "shortcuts" were taken in the engineering and construction of the ship.

A metallurgical analysis of steel taken from the hull of the titanic wreckage reveals that it had a high ductile-brittle transition temperature, making it unsuitable for service at low temperatures; at the time of the collision, the temperature of the sea water was -2°C. The steel was not made by the Bessemer process; such steel would have a high nitrogen content that would have made it very brittle, particularly at low temperatures.

At higher temperatures, the hull plate in the longitudinal direction has substantially better impact properties than for the transverse specimens. At low temperatures, the impact energy required to fracture the longitudinal and transverse specimens is essentially the same. The severe banding is certainly the cause of the differences in the impact energy to cause fracture at elevated temperatures. The specimens made from ASTM A36 steel have the best impact

properties. The ductile-brittle transition temperature determined at impact energy of 20 joules is -27°C for ASTM A36, 32°C for the longitudinal specimens made from the titanic hull plate, and 56°C for the transverse specimens. At low temperatures where the impact energy required for fracture is less, a faceted surface of cleaved planes of ferrite is observed, indicating brittle fracture. At elevated temperatures, where the energy to cause fracture is greater, a ductile fracture with a shear structure is observed.

Ultimately the temperature dependence of the materials properties at the nanoscale becomes very important. There are many direct applications of materials at nanoscale in Solid-State Electronics. The recent developments in nanotechnology can be utilized to test the materials to analyze the suitability of the materials for real-life applications.

Nanomechanical test is a completely low load system, ideal for measuring the hardness and elastic modulus of thin films and coatings. Indentation tests are suitable methods to study the mechanical properties of the material in the nanoscale. It is one of the simplest experimental techniques for measuring a material's ductility and embrittlement behaviour at the nanoscale. Nanoindentation allows for the determination of elastic modulus, yield strength, strain hardening, internal stresses, and deformation mechanisms. Also it provides quantitative information about the nucleation of defects like abrupt bursts. Computer simulations and nanoindentation measurements help to identify the controlling parameters in the behaviour of the materials.

Typical nanoindentation consists of three steps: increasing the load on the indenter until a particular load or depth is reached, holding the load constant for a pre-defined period, and finally decreasing the load on the indenter back to zero. The displacement of the stylus relative to the initial surface position is monitored continuously. This allows both hardness and Young's modulus data to be derived. In the scanning module, a static or increasing load is applied as the specimen is moved perpendicularly to the stylus axis. Variations in topography, scratch resistance or frictional force are indicated.

The hardness and elastic modulus of the material are derived from the resultant depth vs. load curve. The elastic modulus is derived from the slope of the unloading curve and the contact area between the indenter and plastically deformed material at maximum load. Contact areas are determined automatically from the depth vs. load data. The maximum load can be maintained for 20 s in order to eliminate time-dependent effects.

The disadvantage of the nanoindentation test so far is the unavailability of the full capability to carry out the temperature dependency experiments. Recent developments in nanoindentation technology allow the investigation of the temperature dependent properties of materials within limited temperature range. To perform the experiments at high temperatures, insulating material has to be provided to protect the piezoelectric setup of the indenter. A tiny heater capable of maintaining a constant temperature is developed. The hot stage itself consists of a thermally insulating ceramic block, which is attached to the Nanotest sample holder. With the heater at high temperature, the increase in

temperature behind the ceramic block is typically less than 1 degree. The sample is placed on the temperature stage, which can be maintained at different temperatures. In case of Micro materials Nanotester, tiny heater capable of maintaining 773 K and a miniature thermocouple have been added to the diamond stub, close to the tip itself. With both the diamond and sample at the same temperature, heat flow between them does not occur upon contact, thus preventing instantaneous dimensional changes due to thermal expansion.

In present day applications, materials are rarely utilized at room temperature alone. Meanwhile, temperatures may have drastic effects on the mechanical properties and behaviors of materials. Materials behave differently in real-life environments under different thermal Loading.

Many applications such as precision cutting process increase the demand for achieving sub-micron tolerances without sacrificing the reliability of ingenious components [50]. Temperature, which increases during machining, is expected to impact materials responses. In engineering precision cutting processes, from the point of view of micro/meso mechanics, a detailed microscopic picture of material failures, such as surface and near surface defects initiation and evolution mechanisms are still lacking [50]. The need for research also arises due to the emergence of microelectromechanical systems. High tolerance parts with dimensional tolerance of a few tens of nanometers are currently being produced using the advanced diamond tools [50]. Surface contacts or indentation may occur in grain boundaries or within a single grain [50].

High temperature applications of materials also include surface engineered engine components and bearings; optimized mechanical properties at the service temperature. Temperature has influence on complex modulus. There are many applications of nanoscale processing of materials like tungsten coating on the hard disc of computer, tungsten filament in lights. The surface of the hard disc coated with tungsten protective layer is subjected to temperature higher than the normal room temperature. The copper replaces the aluminum in printed circuits. There are many other applications of metals in every industry. Single-Point Diamond Turning (SPDT) is a machining process making use of a single-crystal diamond cutting tool that possesses nanometric edge sharpness, form reproducibility and wear resistance. The process is capable of producing components with surface roughness in nanometer range. Applications of SPDT include, insertion for injection moulding plastic lenses for box camera; the complex infrared lenses and domes in germanium, silicon, and zinc sulfide; reflective mirrors in copper, gold, silver, electroless nickel and aluminum alloys; canner mirror, photoconductor drums in copiers and substrates for memory disks; lenses, windows and prisms in an assortment of polymers (e.g. PMMA); ultra-precision mould in electroless nickel plate, brass and other non-ferrous metals.

Studies of the mechanical response of materials to indentation have not been fully undertaken as a function of temperature. The ability to perform nanotest measurements at elevated temperatures opens up significant new possibilities. The behaviour of materials changes when subjected to temperatures

deviating from the normal room temperature. Thorough study of the behaviour of the materials at different temperatures is very important for the design and applications of materials under different operating conditions. Understanding the critical relationships between the temperature and mechanical properties of metals is very important in design and selecting suitable materials for real-life environments depending on the thermal loading.

Mechanical properties are temperature dependent. The nanoscale analysis of materials is important to understand the behaviour of material and improve the process. Our experiment and simulation methods aim to study the behaviour of FCC and BCC structures in general. The behaviour of the material during loading and unloading are analyzed to understand the recovery of the material after the removal of load. The results of experiment and simulation at various temperatures are compared.

The objective of the research project is to investigate the response of metals to nanoindentation at temperatures above and below the normal room temperature. Single-crystals of tungsten, gold, Aluminum and polycrystalline copper are considered for the investigation. The indentation is done for BCC tungsten on the (111) and (110) crystallographic surfaces, FCC gold on the (111) and (110) crystallographic surfaces, single crystal aluminum with (100) crystallographic orientation and polycrystalline copper at different temperatures. Behaviours of material during both loading and unloading are analyzed to understand the reconstruction of the material during the removal of load. The results are compared with experiment and simulation at various temperatures.

Emphases are placed on the defects generation mechanisms during the elastic plastic contact of crystals. Special attention has been devoted to the elastic response before the onset of plastic yield.

Chapter 2 Literature Review

The following sections cover a comprehensive literature review of work done to study the behaviour of mechanical properties using the nanoindentation technique using computer simulations and experimental methods. Section 2.1 deals with the experimental literature review and Section 2.2 deals with the simulation literature review.

2.1 Nanoindentation Experiments

The literature review clearly shows that not much research has been focused on temperature dependence of materials response under nanoindentation.

William et al [45] performed the experimental work on (100) tungsten. This paper explains that the yielding under contacts can produce a 250 nm displacement excursion. Oliver et al [33] have done nanoindentation experiment on tungsten. This research explains that the load displacement is not linear. They presented an analytic technique to establish the contact area at peak load. The maximum displacement for 10,000 μN is 260nm. The curve is smooth without any periodic bursts. At higher peak loads, the indentation contact in tungsten is not just elastic. As per this experiment, the experimental modulus is 410 GPa. Tungsten is chosen to illustrate the behaviour because of its unique elastic behaviour at low loads. The indenter is held still for 3s after full loading to find any final time dependent plastic effects.

Suresh et al [41] performed nanoindentation experiment on Copper (111) surface and Silicon (100) substrates. The sample film thickness is about 300 to 1000 nm. The indentation penetration depth is approximately 10% of film thickness. The indenter tip radius is 50 nm. Maximum load applied for the indentation is 0.1mN. Suresh et al., explains that the first elastic response is only before h=4.5 nm. Occurrence of first burst and elastic response is independent of film thickness. The indenter radius R=50nm influences the elastic deformation only to a penetration depth of approximately 5 nm. During this time the response is similar to that of a spherical indenter of R=50 nm. The periodic bursts are proportional to the thickness of the film.

The outset of first burst is independent of the film thickness. One burst causes further bursts. As the film thickness increases, the depth increases for a given load. The relationship between P and h is influenced by berkovitch pyramid tip indenter's tip radius R, only in the early stages of elastic deformation. The periodic bursts are due to the nucleation of dislocations. Sometimes nickel tip for gold surface is also used.

Gouldstone et al [17] performed experiment on aluminum (111) surface on silicon substrate. This research considers polycrystalline and single crystal aluminum for the experiment. From this experiment, it is explained that the onset of first burst is independent of film thickness, displacement burst are due to nucleation of dislocations. They had presented a simple model to estimate the

size of the dislocation loops. Tunneling electron microscopy and Atomic force microscope were used in this experiment.

Fraxedas et al [15] performed experiments on single crystal ionic materials. The ultra sharp tips with R<10nm were used. Special attention has been devoted to the elastic response before the onset of plastic yield. In-plane interactions play a key role in the indentation process performed with ultra sharp tips leading to a non-hertzian response of the elastic region of the nanoindentation curve. The interatomic and intermolecular interactions in solids could be directly studied if undeformable tips with radius in the order of these interatomic distances could be produced.

The load displacement curves exhibit periodic bursts in indenter penetration depth, which is interpreted chiefly to be a consequence of the nucleation of dislocations. The first burst occurs when the maximum shear stress at the tip of the indenter reaches the theoretical shear strength. This critical condition is independent of film radius. The average yield strength of the thin film increases with decreasing film thickness. Overall elastoplastic response of the film is sensitive to film thickness. Resistance to nanoindentation systematically decreases with film thickness. The first burst is independent of the film thickness. Elastic deformation obtained in polycrystalline cu films clearly reveals the existence of a significantly higher density of dislocations around the nanoindentation than in the other areas. The rotation of the lattice during nanoindentation accounts for the pile up of material around the indentation. The total elastic energy stored in the film at the onset of the first displacement fully

accounts for the energies of interaction among the dislocation loops punched out during the displacement burst. The resistance to overall micro plasticity is greater at smaller film thickness. Elastic response of metals is unaffected by film thickness. The elastoplastic response is seen to be a strong function of film thickness. The length of displacement bursts is approximately between 15 nm to 30 nm. Kiely et al [23] present the experimental work on Au (111) surface. This paper gives a detailed explanation for the interpretation of scan line graph.

Corcoran et al [8] present the nanoindentation experimental results on Au(111), Au(110), and Au(100). The yielding phenomenon is composed of series of discrete yielding events separated by elastic deformation. The onset of this behaviour is in agreement with the calculations for the theoretical shear strength of gold.

De La Figuera et al [12] observed thermally induced dislocation glide in monolayer Cu films on Ru (0001) at room temperature using scanning tunneling microscopy. The motion is governed by a Peierls barrier that depends on the detailed structure of the dislocations, in particular upon whether the threading dislocations that are dissociated or not. The calculations also reproduce the threading dislocation structure.

Tokushi kizuka [43] shows the results of experiments on point contact of gold with high-resolution transmission electron microscope. It is found that an atomistic pillar like elongated neck is formed by lattice slip and structural relaxation during retraction.

Rodriguez de la fuente et al [36] present the results of study of the emission of dissociated dislocation loops by nanoindentation on a (001) FCC surface using experiments and simulation methods. The dissociated loops, which intersect the surface are shown to originate from loops of interstitial character emitted along the <110> directions and are usually located at hundreds of angstroms away from the indentation point. Computer simulations also show the similar results.

Swain et al [42] present the results of mechanical property characterization of thin films using spherical tipped indenters. The use of very small spherical tipped indenters provides more tractable solution to the contact problem. Also, it is possible to follow the elastic to plastic or brittle behaviour during indentation more clearly than pointed indenters. Actual behaviour of the indented materials may be obtained by complementary micro structural observations of the indented region. The role of substrate and interface adhesion on the force-displacement behaviour of thin films indented with spherical tipped indenters is also presented.

Gerberich et al [16] presents results of Fe3wt%Si single crystals when contacting the surface with sharp diamond tips. It is demonstrated that a unique point in the load-displacement curve can be associated with the first dislocation nucleated. This occurs at loads in the vicinity of 100 PN for a 66 nm radius tip. Subsequently, this produces an avalanche of dislocations estimated to range from about 15 to 74 in number depending on the magnitude of the yield point load. A

model, based upon discretized dislocations is proposed for both the initiation of yielding at an upper yield point (UYP) and the arrest of the indenter at a lower yield point (LYP). The UYP is interpreted in terms of Rice's unstable stacking energy concept, previously applied to crack tips, and accounts for tip radius, oxide film thickness and image force effects. The LYP is interpreted in terms of the back forces provided by previously emitted shielding dislocations. These two approaches provide first order solutions of the upper and lower yield points which both vary from test to test by as much as a factor of four. The large variation in nucleation load is proposed to be due to point-to-point differences in oxide thickness, which might range from 4.5 to 8.5 nm.

Krystyn et al [26] report the analytical formulation of the elastic limit that predicts the location and slip character of a homogeneously nucleated defect in crystalline metals, and extend this formulation to the atomic scale in the form of an energy-based local elastic stability criterion. Also reports results on the three-dimensional molecular dynamics simulation in several face-centered cubic systems that elucidate the transition from the initiation to the early stages of plasticity during nanoindentation of metals, as characterized by homogeneous and heterogeneous nucleation of up to hundreds of dislocations.

Ju Li et al [20] present a fundamental framework for describing incipient plasticity that combines results of atomistic and finite-element modeling, theoretical concepts of structural stability at finite strain, and experimental analysis. The two key features of the nucleation and subsequent evolution of defects are studied. Detailed interpretation of the experimentally observed

sequence of displacement bursts is proposed to elucidate the role of secondary defect sources operating locally at stress levels considerably smaller than the ideal strength required for homogeneous nucleation. These findings provide a self consistent explanation of the discontinuous elastic-plastic response in nanoindentation measurements, and a guide to fundamental studies across many disciplines that seek to quantify and predict the initiation and early stages of plasticity.

Hebbache, M. [18], report the investigation of the behaviour of elastic and mechanical properties of silicon. The study is focused on the behaviour of the hardness. The depth dependence of the hardness up to about 90 nm is taken in to account. At this depth, the semiconductor-metal phase transition occurs. The validity of the theoretical approach was checked by determining the force-depth indentation curve.

Dawn A. Bonnell [11] summarizes the advancements in making low dimensional structures from inorganic and organic compounds, determining the resulting, and necessarily local properties and assembling complex structures.

Lorenz et al [30] observed the homogenous nucleation of dislocations in dislocation-free single crystals. This is related to a sudden jump in the force-displacement curve. The mechanical stress for the set-in of this pop-in effect has been estimated with the Hertzian elastic contact theory. Experimental results of dislocation loop nucleation show good agreement with the continuum theory of dislocations.

Bradby et al [4] used electrical characterization technique to study details of the deformation behaviour of crystalline silicon during nanoindentation. For spherical indentation, the onset of a transformation to a metallic Si-II phase is observed before the so-called "pop-in" event occurs during loading. The electrical measurements have provided considerable insight in to the evolution of deformation processes during indentation loading and unloading of Si.

Carrasco et al [6] found that the dislocations with a screw component are shown to glide across {111} planes and by a cross-slip mechanism giving rise to revolving terraces in the neighborhood of the nanoindentation trace with their edges parallel to compact <110> directions.

Ma et al [48] MD simulation results shows that the burst and arrest of stacking faults are the key factors for the plastic deformation of nanocrystalline Cu under nanoindentation. Z. Q. Zou et al [42] studied Cu (100) by scanning tunneling microscopy in ultrahigh vacuum at room temperature. The experimental and simulations results of Al on Si by Yoonjoon Choi et al [43] shows that the early stage plasticity is strongly size dependent. Y. M. Wang et al [44] found that the yield strength for nanostructured Cu increases at low temperatures and also the tensile ductility and uniform strains also increases at cryogenic temperatures. The yield strength for Cu with ultrafine grain size is temperature and strain-rate dependent. But the conventional FCC metals are insensitive to temperature and strain-rate. The nanoindentation experiments on Fe at different orientations by Roger Smith et al [45] shows that the defect

generation and motion causes the plastic and elastic deformation, which is reflected in the pile up patterns. The pop-ins shown by the *P-h* curves corresponds to the formation of dislocations. The contact pressure (nanohardness) increases with decreasing indentation depth. Mao S X [47] performed indentation on nanocrystalline copper by Atomic Force Microscope (AFM) diamond tip. Also Lu L et al [48] studied the superplastic extensibility of nanocrystalline copper at room temperature. Yu I. Golovin et al [49] studied the stepwise transition from elastic to elastoplastic deformation at the initial stage of nanoindentation. I. Yonenaga et al [51] performed the temperature dependency studies for the hardness of Bulk Single Crystal GaN in comparison with other wide-gap materials. Vickers indentation method was used to determine the hardness of crack-free GaN samples. D J Branagan et al [52] investigated the Low-Temperature super plasticity in a nanocomposite iron alloy derived from a metallic glass Nanotechnology. Mechanical deformation studies on the nanocomposite structures at room temperature revealed that although they exhibited high yield strength, they were brittle and exhibited no tensile elongation. Results revealed that the main mechanism for elevated temperature deformation was grain boundary sliding/rotational processes. Xiao Dong Zhang et al [54] performed a detailed study on the structure and mechanical response of Ti-Si-N coatings deposited at low and high temperatures. Coating mechanical properties and mechanical properties was obtained by nanoindentation technique. By increasing the deposition temperature from 523 K to 973 K lead to significant increase in hardness.

Richard et al [35] study the mechanical behaviour of 1 μm Cu thin films capped with a 100 nm thick $Si_3 N_4$ layer. This result explains the early yield phenomenon. It is reported that the preferential diffusion of oxygen in copper grain boundaries or interfaces is the likely cause of the early yield behaviour. If a dislocation is prevented from reversing direction on the same slip plane, then the early yield will not be observed. The early yield occurs when copper is contaminated with oxygen. The maximum temperature tested is up to 773 K.

Bahr et al [2] reports high temperature indentation on Fe-3%Si. The nanoindentation experiment was carried out on Fe-3% Si at room temperature and at 379 K. The lack of a clear dependence of the load at which the yield point occurs with temperature in this system lends support to the fact that while the rate of nucleation may be altered the basic criteria to initiate a loop remains independent of temperature. The data from their experiment suggests that the load at which yielding occurs is independent of temperature between room temperature and 379 K.

High temperature nanotesting, micro materials measuring technology [19] is an article explaining the technique for higher temperature nanoindentation technique. A tiny heater capable of maintaining a constant temperature has been added to the stage. The hot stage itself consists of a thermally insulating ceramic block, which is attached to the nanotest sample holder. With the heater at high temperature, the increase in temperature behind the ceramic block is typically less than 274 K. The experiments performed show that significant softening occurred at the higher temperatures, as it is observed

from the penetration depths read from the curves. It is also noted that the elastic recovery reduces at higher temperatures. Also it is noted that a reduction in modulus occurred as the temperature increases. Also, the creep occurred during the 60s hold period at maximum load. The amount of creep increased as the temperature increases. Investigation of thin film and surface creep is an important application of high temperature nanotesting.

Kim et al [24] present the experimental results of the nanoindentation of a bulk amorphous metal alloy at room temperature. The experimental evidence shows that the highly confined and controlled local contact at the ultrafine scale in the form of quasi-static nanoindentation of a bulk glassy metal alloy at room temperature also causes nanocrystallization. The nanocrystallites nucleate in and around shear bands produced near indents and they are same as crystallites formed during annealing without deformation at 783 K.

Ben et al [3] describes a new high-temperature stage for small-scale mechanical property testing. This allows the determination of the load-penetration curve of a diamond tip in a temperature range extending from room temperature to 673 K. Nanoindentation results are presented for gold, soda-lime glass, fused silica and a polyimide. Results from fused silica show that its mechanical properties exhibit completely different temperature dependence from those of soda-lime glass, as expected since fused silica is an anomalous glass.

Smith et al [40] performed the small scale hardness and elastic modulus measurements on glass, gold, and single crystal silicon at room temperature and

473 K. The results show that at 473 K the hardness and elastic modulus of soda lime glass and gold are lower than at room temperature. In contrast, indentation testing of Si(100) at 473 K produced a similar hardness value to that obtained at room temperature, although the modulus was again reduced, from 140.3 to 66.0 GPa. The 'pop out' event observed during unloading of a silicon indentation at room temperature, disappeared at 473 K.

The literature review of nanoindentation experiments shows that research on the analysis of materials, as a function of temperature is very limited, despite the importance of such studies. Many researchers have highlighted the importance of this issue in the past. Attempts were made to study of the properties and structural behaviour during nanoindentation at normal temperature. The structural behaviour and property changes during the thermal loading become equally important. Facilities are now available to explore this new topic. This work attempts to explore the complete behaviour of metals at various temperatures, including the initial burst, the complete elastic recovery, the softening effect and the modulus and Hardness.

2.2 Computer Simulations

Komanduri et al [25] performed MD simulation of nanoindentation on aluminum on various crystal orientations to investigate the anisotropy in hardness and friction. Depending on the crystal orientation, the atoms near the surface were found to be disturbed to different degrees due to the repulsive forces between them as the indenter approaches the work material. The hardness is found to increase significantly as the indentation depth is reduced to atomic dimensions. The simulation is done at various indentation velocities such as 1, 10, 100 m/s. They have also performed the simulation for a scratch test. The Morse potential is used. The simulation is performed to determine the friction, hardness and wear characteristics. The atoms near the surface are found to be disturbed to different degrees due to repulsive forces. The occurrence of a critical yielding phenomenon and a significant load drop after the tip had penetrated approximately 1.5 layers in the substrate is noted. The total number of atoms in the work material range from 4382 to 5131 depending on the crystal setup. Simulated indenter tip has 2551 total atoms. In Aluminum, [110] is the closed packed direction and have minimum atomic density, (111) has maximum atomic density. The width of the work material is 6-lattice spacing. The maximum indentation depth is 0.81nm just prior to the initialization of the scratch process. It is seen that force interactions commence at 0.2nm as the indenter approaches the work piece. The solution is obtained using the fourth order Runge Kutta algorithm with a fixed integration step size of 0.1 atomic time units. The zone of disturbed material is 8 layers from the surface. The result

shows practically negligible initial disturbance on the top layers of the work material.

Shenderova et al [39] has done simulation on (111) surface. They have chosen gold as the sample. The depth of indentation is 0.75 nm and 1.7nm. The shape of the indenter tip is spherical with a radius of 3.2 nm. Two sets of simulation were done. In one case, the potential for substrate embedded atom method (EAM). Potential for tip surface interaction is modeled with the repulsive region of a Lennard Jones potential. This model excludes strong tip substrate adhesive interactions. In second set of simulation, the depth is 2 A° for 40 points. The load displacement curves measured by nanoindentation can be altered by stresses in the sample. Strained gold lattice containing 24576 atoms in an FCC lattice with a thickness 5.4nm, and periodic lateral dimensions of 9.2 nm by 8 nm and (111) surface orientation were considered. The pile up area atoms have stress approximately half of that of bulk substrate. At deeper indentation depth of $10A^{\circ}$ a raised lip of atoms surrounding the indenter was observed. Tip surface interaction was modeled with the repulsive region of a Lennard-Jones potential. The loading curve is obtained by summing the forces on the tip at a given indentation depth. The maximum indentation depth of 7.5 A°, (absence of raised lip) and $17A^{\circ}$ were modeled. The constant time step of 1fs is applied. The tip moves at a constant rate of 10^{-4} nm per time step in to the surface.

Yongsheng Leng et al [50] performed simulation on (001) surface. The substrate material is crystal copper slab. Indenter direction is [001]. The indenter has a blunted rigid tip. The indenter is cleaved by two (110) planes and two

(001) planes from the FCC structure, which makes the tip infinitely wide in the [010] direction. The indenter contains 140 atoms. Two static bottom layers and 18 dynamic layers. Each layer consists of 320 atoms. The total number of atoms in the substrate is 6400. Periodic boundary conditions are imposed on [100] and [010] directions. The size of the MD cell in the y direction, which is [001], is $9.5a_o$. a_o is the equilibrium lattice constant (for FCC copper, a_o= 0.3615 nm). The size of the MD cell in the x [100] and z direction [010] are $40a_o$ and $4a_o$, respectively. Periodic boundary conditions are imposed on [100] and [010] directions. The temperature is controlled around 0.1 K via Brownian dynamics method. It is considered as a cold crystal slab. The tip moves towards the substrate with increments of $0.02a_o$ over 200 per time steps (Δt). Time step = 3fs. This corresponds to the indentation speed of 12 m/s. For perfect crystals at low temperature, the longitudinal sound speed is usually in the order of 10^3 m/s. The focus of the research in this paper is on engineering precision cutting process. Due to increased demand for achieving the sub micrometer tolerances without sacrificing the reliability of ingenious components, this problem has to be studied. In engineering precision cutting processes, high tolerance parts with dimensional tolerance of a few tens of nanometers are currently produced using the advanced diamond tools. From the point of view of micro/meso mechanics, a detailed microscopic picture of material failures, such as surface and near surface defects initiation and evolution mechanisms in friction and wear processes is still lacking. This paper gives the complete description of the tip-to-substrate approach. However, the emphases are placed on the atomic stress analyses, load approach and system potential energy variations and the defects generation mechanisms during the elastic plastic contact of crystals, which have

considerable practical relevance to the micro hardness of ultra-thin films and the material failure modes. The potential for the substrate is EAM. But in practice, Yongsheng Leng et al [50] adopt Johnson's first neighbour modifications. (Johnson's simple nearest-neighbour analytic model). The cut off distance is between the first and second neighbours (which makes the force calculations quite fast) and cutoff distance is equal to $0.8a_o$. Prior to indentation, the distance between the bottom layer of the tip and the topmost layer of the substrate is set to be $0.8a_o$ and the corresponding tip approach is denoted by zero.

During the initial contact stage, the attractive force between the tip and the substrate increases dramatically and the energy curve decreases. This instability corresponds to the jump-to-contact (JC) phenomenon. Our simulations show that during the JC process, the kinetic temperature of the system increases from 0.1 K to 0.35 K due to the bulging of the surface atoms, and then this temperature rise is dissipated to the ambiance in a time span of 1ps through stochastic collisions. At onset of contact formation, where the tip approach is approximately $0.04a_o$, the maximum attractive force, or the adhesion force F_y attains a value of 16nN. The copper atoms in the region of the surface under the tip displace by approximately 0.15 nm toward the tip in a short time span of 0.6ps. As the tip approach continues to increase, the load curve starts to go up. However, the potential energy continues to drop down until it reaches a local minimum at $0.32a_o$, where the contact load equals approximately to zero. At this point, the system is stable, where the metal bonding between the tip and the substrate is constructed without bond stretching. Further indentation of the substrate by the rigid tip reveals that the contact load increases monotonically,

indicating that the strain energy is stored in the strained substrate due to the inter-atomic interactions between the tip and the sample. The corresponding atomic configuration for tip approach is $1.3a_o$, which notably depicts the surface elastic deformation of the substrate. Here we see that the topmost layer of the tip reaches the second layer position of the dynamic substrate, and the sample surface atoms are indented approximately to the third layer position. Upon retraction of the tip, we observe that the unloading curve is almost along the loading path, Suggesting that the response of the material is linearly elastic. Simulations also indicate that the temperature rise in plastic instability. The corresponding kinetic temperature increases from 0.1 K to 0.6 K due to the release of the substrate strain energy, and then it comes back to the ambient temperature through the stochastic collisions via the Brownian dynamics. The retraction shows that the unloading curve is almost parallel to the loading one, resembling to the macroscopic behaviour of an elastic-plastic bar under uniaxial loading and unloading cases. The complexity of the material plasticity for FCC crystals may explain the macroscopic phenomenon where some ductile materials elastic limits are greater than their yielding stresses. It is mentioned that their findings could also explain to some extent the micro-mechanisms of material softening, such as rock material yield under compression.

Cynthia et al [9] present the simulation on (111) surface of gold sample. Indenter shape is spherical and the radius is 8nm. The potential for the substrate is EAM. The tip surface interaction is frictionless, and the indenter tip is represented by a repulsive potential. This avoids the numerical problems during energy minimization caused by a perfectly hard sphere potential. The substrate

material, gold (Au), is represented by a slab of dimension 240x210x160A°, containing 470000 atoms. Periodic boundary conditions were used parallel to the substrate. The bottom layer was held fixed. The important point is that when the indenter is retracted after reaching the first yield point, the force at small displacements matches that during indentation. This indicates that the plastic deformation created at the first yield point has healed during retraction. In contrast, the force profile during retraction from the second yield point indicates permanent deformation after retraction. All of the defects in this system lie on {111} planes that are the energetically preferred slip planes in the FCC lattice. From the (111) surface, there are three unique {111} planes extending in to the bulk. In this structure, defects can be seen parallel to only two of these three planes.

Zimmerman et al [53] simulate the indentation on (111) surface of gold sample. The size of the sample is 19 nm wide by 40 nm long by 12.5nm thick. The shape of the indenter tip is spherical with a radius of 4 nm. The simulation temperature is 0° K. This paper explains that the dislocation mechanism is due to the release of compression beneath the indenter and due to the conservation of volume in the thin film during micro plastic deformation (bursts). This paper also finds that the rotation of the lattice during nanoindentation may account for the pile up. The first burst occurs when the maximum shear stress at the tip of the indenter reaches the theoretical shear strength. The pile up also causes the change in slope of the indentation curve.

Chung et al [7] report the nanoindentation simulation technique based on the finite element method. This paper explains the effect of tip radius on nanoindentation hardness tests. The sample is an aluminum film on the silicon substrate. They found that the hardness is relatively insensitive to the tip radius. For silicon layer on the aluminum substrate, the hardness is much more sensitive to the tip radius. This method uses the blunt indenter. A cone with a spherical cap with various radii models the blunt indenter. The emphasis is put on the stress and strain distribution in the specimen. The indenter and the specimen are treated as bodies of revolution to avoid the difficulty of modeling the real pyramidal indenter with nonzero tip radius. Maximum depth is 90 nm. Maximum Load is 400 μN. When the indentation depth is less than d_o, the indenter is simply a sphere. Where d_o is the distance of indenter from the tip. For indentation depths less than 40 nm, the hardness decreases somewhat with increasing tip radius. However the variation is less than 10%. The hardness for indentation depths larger than 60nm is not sensitive to either the tip radius or the indentation depth. For spherical indenters with different radii, the hardness increases with the ratio of the contact radius to the tip radius. For larger indentation depths, the effect of the tip radius is negligible and the indenter can be treated as a cone. MD simulations show that the nanoscale plastic deformation due to point indentation takes place through the creation and motion of point defects. Various thickness values of 20, 40, 80 nm are considered.

From load displacement data as found by Shenderova et al [39], it is possible to obtain both local elastic moduli and hardness of thin films. The load displacement curves can be altered by stresses in the sample. For example, for

Aluminium and Aluminium alloys, there is an increase in slope of the unloading curve for compressive stress. The stiffness of the material increases with compressive stress. Hence the hardness and elastic modulus (effective modulus) increases with compressive stress and decreases with tensile stress. This is consistent with properties of bulk materials. For tensile stress, there is decrease in slope. For most FCC metals, the Young's modulus decreases for tensile strain along <111> and <110> directions. But the modulus increases along <100>. The pile up of material surrounding the indenter causes a change in the slope of the indentation curves. This pile up is apparently promoted by the compressive stress and diminished by tensile stress. As the stress state of a film influences nanoindentation load displacement curves, appropriate analysis of shallow indentation curves measured at different points could in principal be used to map local residual surface stress distributions. This is very useful for characterizing the influence of surface features like dislocations and steps on residual surface stresses. This type of analysis requires a detailed understanding of the relationship between these stresses and the indentation data. Atomistic modeling is a powerful tool to calculate the local atomic stresses in the indentation point prior and during the indentation.

David Christopher et al [10] present the results of their experimental and theoretical investigations results of nanoindentation in iron and silver. The effect near the grain boundaries was investigated. The molecular dynamics simulations also exhibit the similar results. It shows the plastic deformation of the Substrates with piling-up of the work material along the indenter sides. A simulation also shows the formation of defects.

Kallman, Jeffrey S et al [22] uses nonequilibrium molecular dynamics technique to model the nanoindentation of pure silicon to study the dependence of phase transformations on crystal temperature and indenter speed. The position of the atoms in the material was calculated and atomic images of the crystal structure were displayed as a function of time. Several diagnostic imaging techniques were developed to aid the analysis of phase transformations.

Fivel et al [14] report results on the 3D simulation of the dynamics and interactions of dislocations in FCC metals based on discretization of both time and space at a mesoscopic scale. A method to implement complex boundary conditions on a 3D finite elastic medium including discrete dislocations is proposed. The obtained heterogeneous stress field is computed through a finite element resolution. The dislocation segments can then move in a 3D FCC network depending on this heterogeneous stress field. A method to deal with the plastic relaxation through the strain produced by the segment glide is proposed. An application to the simulation of the bowing of a loop under an indentation is shown. The particular case of a (001) indentation axis induces cross slip events on some screw parts of the loop where the stress is very high. Image stresses are not very important compared to the stresses due to the indentation.

Rodriguez de la Fuente et al [37] present the results of study of the emission of dissociated dislocation loops by nanoindentation on a (001) FCC surface using experiments and simulation methods. The dissociated loops, which intersect the surface are shown to originate from loops of interstitial character

emitted along the <110> directions and are usually located at hundreds of angstroms away from the indentation point.

Computer simulation also shows the similar results. It is found that the initial stages of plastic deformation around the nanoindentation result in the emission from near the contact point of dislocation half-loops intersecting the surface. They can alternatively be created by accretion of irradiated-in interstitials. These loops are split into pairs of Shockley partial dislocations giving rise to peculiar configurations at the surface (hillocks), involving four Shockley partial dislocations and a stair rod. Our computer simulation results on copper also show the similar results. Our simulation results on copper also show the similar results. Dissociated loops glide across compact planes, and this provides a novel mechanism for matter transport away from nanoindentations.

Liang et al [27] performed the Molecular Dynamics simulation to study the microstructure origin of the elastic–plastic deformation due to nanoindentation on the (100) surface of a Cu substrate. It is found that for small indentation depths, the response is elastic but is found to deviate from the Hertzian solution, mostly due to the small tip radius used in the simulation. In case of depths, the deformation is complex leading to an inhomogeneous dislocation structure. Different mechanisms are found to be responsible for the deformation of different parts of the contact surface, some elastically, some via the dislocation bow-out and some via the nucleation and growth of Shockley partials and their subsequent interaction to form locks. The combined effect accounts for the observed complexity of the quasi-elastic behaviour, with

interspersed minor yields on the load–displacement curve. As evident from the experimental results, the stair-rod lock formation explains the observed time-delayed occurrence of pop-in below the spontaneous pop-in load from their simulation results. Our computer simulation result also inline with their simulation results for a particular temperature. But our simulation is extended also to study the effect of temperature on the structure.

Liang et al [28] carried out the Molecular Dynamics simulation to study the loading and unloading behaviour of nanoindentation on copper surface as a function of crystallographic orientation. The deformation and recovery are found to be attributable to the different underlying dislocation structures resulting from the crystallographic anisotropy. It is found that, at small indentation depths, dislocation-induced plasticity can sometimes be completely recovered upon unloading. The origin and implication of this recovery is also explained.

Liang et al [29] report the results of molecular dynamics simulation studies of crystalline plasticity during nanoindentation. The elastic-plastic response of three copper substrates with surfaces (001), (110), and (111) crystallographic planes are compared. The reduced modulus of (111) surface is largest and (001) is the lowest. The elastic stress distribution is calculated from finite element method and is qualitatively consistent with the MD simulation results. The reduced modulus, dislocation nucleation, and subsequent microstructure evolution are investigated. Differences are found to exist in the deformation behaviour. Yielding platforms exist in the load displacement curve of Cu (001), which can be attributed to effective resistance of dislocation locks.

Load drops are found in Cu (111) and Cu (110) due to more mobile dislocation structure.

Krystyn et al [26] report the analytical formulation of the elastic limit that predicts the location and slip character of a homogeneously nucleated defect in crystalline metals, and extend this formulation to the atomic scale in the form of an energy-based local elastic stability criterion. They also report results on the three-dimensional molecular dynamics simulation in several face-centered cubic systems that elucidate the transition from the initiation to the early stages of plasticity during nanoindentation of metals, as characterized by homogeneous and heterogeneous nucleation of up to hundreds of dislocations.

Feichtinger et al [13] performed atomistic simulations to investigate the nanoindentation deformation properties of model nanocrystalline gold with grain diameters of 5 and 12 nm, using both conjugate gradient and molecular dynamics. It is found that grain boundaries act as efficient sinks for dislocation nucleation below the indenter and the intergranular sliding occurs. It is established that at the 5nm grain diameter regime there is a decrease in the Young's modulus.

Ju Li et al [20] present a fundamental framework for describing incipient plasticity that combines results of atomistic and finite-element modeling, theoretical concepts of structural stability at finite strain, and experimental analysis. The two key features of the nucleation and subsequent evolution of defects are studied. Detailed interpretation of the experimentally observed

sequence of displacement bursts is proposed to elucidate the role of secondary defect sources operating locally at stress levels considerably smaller than the ideal strength required for homogeneous nucleation. These findings provide a self consistent explanation of the discontinuous elastic-plastic response in nanoindentation measurements, and a guide to fundamental studies across many disciplines that seek to quantify and predict the initiation and early stages of plasticity.

Anil Gannepalli et al [1] present the results of atomistic mechanisms of plastic deformation during nanoindentation of a Au (001) surface with a noninteracting indenter. The defects structures formed during the initial plastic yield are identified. As evident from our experimental results, their simulation results also show that during the indentation, the accumulated elastic energy in the indented region is partially relieved by the nucleation of a pyramid defect structure. Mechanism of defect also found from our simulation results of copper. While unloading the indenter after the first yield, the pressure due to compressive strain in the defect induces restoring forces that heal the plastic deformation. But further indentation causes stair locks as also seen from copper simulation results. Then the indentation results in a permanent deformation after second yielding. They also proposed a three step mechanism based on dislocation theory, which explains that the defects produced depend on the crystallography of the indented surface.

Reith et al [34] explains the methodology to be followed for complex nanomachines. Simple nano objects are only of minor interest. The structures

with complex shapes or interactions (cluster-cluster or surface-cluster) under various conditions play an important role. For nanomachines the MD models have to contain moving parts. The present work includes the setup of the initial values according to the rotational or transitional movements and for the construction of individual objects. The paper also discusses the difference between nanoengineering and common mechanical engineering. The synthesis of real nanomachines has not yet been performed, but it is a most interesting topic to perform molecular dynamics studies. It is also emphasized that the properties of nanosystems vary strongly with temperature.

Xavier Lafontan et al [46] studied the effect of temperature on RF switches with metallic membranes. The expected thermal effects on RF switches are discussed. The results of simulation and experiment are presented. In the metallic switches, the structural layers can be gold, copper, or aluminum. When the membrane in the switch is heated, the stresses in the flexure joints will change significantly the mechanical parameters and design parameters such as actuation voltage and communication speed may be modified drastically. The elongation of metal will introduce compressive stress that may buckle the membrane. If the metal length decreases then its elongation capability will be reduced and the critical temperature will be higher. When the temperature increases, the metallic layer dilates and if this one is clamped, a compressive stress appears. Consequently, the temperature acts mainly on the intrinsic stress. So, basic stress-monitoring test structures are well suited for the study of the temperature influence in metallic layers. The studied structural layer I electroplated gold. Electroplating process creates low tensile stress than other

deposition techniques like evaporation or sputtering. It is demonstrated that stress test structures can monitor the variation of stress versus temperature. Moreover, finite element simulations can estimate the critical buckling temperature. The design of stress relaxation structures in the membranes can reduce the actuation voltage while decreasing the sensitivity to high temperature.

Kalia et al [21] presents their results of simulation at high temperature. The mechanical energy release rate corresponding to the onset of fracture increases significantly with an increase in temperature because of dissipative effects such as dislocations, micro pore formation and coalescence and crack deflection. At room temperature, we observe large shear stresses close to the crack tip, which cause cleavage fracture. At 1500 K, tensile and compressive stresses are in all regions throughout the system due to enhanced mobility. Refractory metal intermetallics represent the most promising metal alloy technology for temperatures above 1473 K. This explains the use of repulsive potential between substrate and tip.

Chapter 3 Theory

3.1 Theory on Experimental Research

Nanoindentation testing system

A typical nanoindentation system involves mechanism in which the load on the indenter can be increased until a particular load or depth is reached, then holding the load constant for a pre-defined period, and the final unloading. The displacement of the diamond relative to the initial surface position is monitored continuously. The hardness and elastic modulus of the material are derived from the resultant depth vs. load curve. The elastic modulus is derived from the slope of the unloading curve and the contact area between the indenter and plastically deformed material at maximum load. Contact areas are determined automatically from the depth vs. load data. The maximum load can be maintained for up to 20 s to eliminate time-dependent effects.

The complete low load nanomechanical test system is ideal for measuring the hardness and elastic modulus of thin films and coatings. The Hysitron TriboIndenter® provides quantitative nanomechanical testing capabilities with the convenience of modern automation. Available in normal and lateral force loading configurations, the TriboIndenter® revolutionizes the sub-micron scale testing arena with real-time data collection and nanometer resolution with the optical viewer. The patented transducer technology provides X, Y, Z and Z piezo positioning. TriboIndenter® provides testing based on quantitative, controlled nanoindentation of surfaces. Automated precision

testing, staging and sample positioning allows maximum throughput of samples. It has been built on a single platform designed to support the numerous nanomechanical characterization techniques. This high-performance staging system offers superior stability and flexibility to accommodate a wide range of applications, sample types and sizes. The TriboIndenter® needed to carry out measurements in this thesis incorporates the three-plate capacitive transducer technology known for its sensitivity and stability along with superior staging design to deliver outstanding performance in nanomechanical characterization. Test placement on surface features or material phases is accomplished using high-performance top-down optics or in-situ imaging. Hysitron's exclusive in-situ imaging capability provides unparalleled precision in placement of the indenter probe. Automated testing patterns, such as lines, grids and circles, allow tests to be designed based on the interface or sample geometry. Methods can be designed that will run a variety of tests on multiple samples without any user intervention.

The acoustic/thermal enclosure provides the Environmental Isolation. Potential problems, which test stability and accuracy such as ambient noise and vibrations, are damped through active and passive damping. Passive damping of noise is accomplished by means of the acoustic enclosure. The enclosure also assists in minimizing the effects of thermal gradients that can cause instabilities that affect the repeatability of test results. Piezoelectric vibration control stages actively damped vibrations under 200 Hz and passively damped vibrations over 200 Hz. Utilization of a granite frame yields exceptional dimensional stability during the testing process in any environment.

The heart of Hysitron's testing instruments is the patented three-plate capacitive transducer that is used as both the actuator and sensor of the instrument. The force is applied electrostatically while the displacement is simultaneously measured by the change in capacitance. Electrostatic actuation requires virtually no current, which results in virtually no drift due to heating during actuation. This provides superior drift characteristics to many competing designs, such as electromagnetic devices, that realize significant heating during actuation due to high current requirements. Low drift means that data can be acquired faster with more accuracy and repeatability.

The sensitivity and dynamic characteristics of the transducer allow high frequency testing for investigation of viscoelastic materials. The low mass of the indenter probe and driving transducer plate, combined with low damping make this a versatile tool for testing over a wide range of frequencies

Top-down optics with a CCD camera have been incorporated into the TriboIndenter® for high magnification and visual observation of sample surfaces and selection of testing locations. Motorized zoom optics allows selection of magnification and field-of -view to accommodate virtually any sample size. The optics utilizes bright-field illumination and polarized light to view the sample surface and allows differentiation of phases within many materials. With the ability to resolve one-micron features and sub-micron stage resolution, the tip can be placed within a micron of the desired surface feature or test location

optically. For greater precision in probe placement, in-situ imaging can be used to refine the probe position.

The optics specifications are as follows:

Maxfield of view: 560μm x 420μm.

Min field of view: 80μm x 60μm.

Magnification: 500X – 3500X.

In-situ imaging allows Scanning Probe Microscope (SPM) imaging of the sample surface with the same tip used for testing and has been incorporated into the TriboIndenter® to allow pre and post-test observation of the material surface. This feature provides the capability to position the indenter probe within ten nanometers of the desired test location. This provides a level of precision not offered by instruments that rely on stages to translate the sample from the optics or SPM to the probe position. Identification and characterization of phases in multiphase materials or fine surface features can only be reliably carried out by employing in-situ imaging. Posttest imaging also provides the ability to verify that the test was performed in the anticipated location, which maximizes the reliability of data and aids in explanation of unexpected test results.

Quantification of material deformation features is necessary for many analyses that have been derived to interpret nanoindentation and nanoscratch tests. In-situ imaging allows observation and quantification of deformation, such as pileup, wear volume or crack length, incurred by testing. A versatile software package has been developed for the in-situ imaging capability that offers features such as pattern recognition for patterned testing. The software package also

includes real-time and off-line image processing and analysis tools for the quantification of deformation incurred by testing.

The thermal stage that allows nanoscale testing of materials at non-ambient temperatures is now available. Temperature control is accomplished by incorporating a Peltier thermal element that is located beneath the sample specimen. The temperature of the sample stage is controlled by a Melcor controller to < 0.002°. A simple to use Graphical User Interface (GUI) allows the user to dynamically change temperatures during testing. The indenter probe shaft has been replaced by an insulating, low thermal expansion ceramic that minimizes the effect of the temperature differential between the tip shaft and the sample. Insulating and heat removal components have been added to isolate the temperature. To minimize the condensation on the sample, a user specified gaseous delivery system was developed. The thermal stage specifications are as follows:

Practical thermal operating range from -10°C to 100°C

1.2" x 1.2" copper thermal energy distribution element

Minimized sample platform thermal drift to 0.3nm/s at set point

100°C reached in 10 minutes

10°C reached in 20 minutes

Virtually zero added noise

Thermal energy transfer

Ethylene glycol/Water cooling system

Chiller unit dimensions 19"x17"x7"

Melcor controller dimensions 10.5"x7"x5"

Analyzing a Single Indentation

1. Use the Upper and Lower Fit %'s to select the portion of the unloading curve to fit to the power law relation,

$$P = A\,(h\text{-}h_f)^m$$

2. The unload point is the index of the data point of maximum load.

3. The following procedure is used to calculate the hardness and reduced Modulus E_r.

   a. The selected portion of the unloading curve is fit to the power law relation,

$$P = A\,(h\text{-}h_f)^2\ .$$

   b. The derivative of the power law relation with respect to h is evaluated at the maximum load to calculate the contact stiffness S.

   c. The contact depth, h_c, is calculated with the following

$$h_c = h_{\max} - 0.75\frac{P_{\max}}{S}$$

   d. The hardness is calculated with

$$H = \frac{P_{\max}}{A(h_c)}$$

   e. The reduced modulus is calculated with

$$E_r = \frac{\sqrt{\pi}}{2\sqrt{A(h_c)}}S$$

   f. The area function $A\,(h_c)$ used in all calculations is the currently defined area function.

The tip area function $A\ (h_c)$ for the selected indenter tip is generated by fitting the following equation by using the reduced modulus of the standard material.

$$A(h_c) = C_0 h_c^{\ 2} + C_1 h_c + C_2 h_c^{\ 1/2} + C_3 h_c^{\ 1/4} + C_4 h_c^{\ 1/8} + C_5 h_c^{\ 1/16}.$$

The stiffness is calculated from the eqn. $S = \frac{2}{\sqrt{\pi}}\left(E_r \sqrt{A}\right)$

Yield stress is calculated from the eqn. $r = \sqrt{\frac{3P}{2\pi\sigma_y}}$

Where P is the maximum indentation load, r is the horizontal distance (radius of the elastic-plastic boundary)

$$P = h\text{-}h_f$$

Loading rate (μN/s) = peak force /segment time.

For Berkovich tip (pyramidal geometry tip), the projected area to depth relationship is $A = 24.5 h_c^2$

For berkovitch tip, $h_c = h_f - \frac{P_{\max}}{S}$

Tip Area Function Calibration

The following is a step-by-step procedure for calibrating a tip of any shape using the Hysitron TriboIndenter. Before following this procedure, a machine compliance correction must be made. It is also best to have a method that can be set up using the method editor, to automatically perform the indentations.

Tip-shape calibration is performed by determining the area function of the indenter tip. The method is based on the assumption that Young's modulus of elasticity is constant and independent of indentation depth. Fused quartz with Young's modulus of 72 GPa is used as a standard sample for calibration purpose. An area function relating the projected contact area (A) to the contact depth (h_c) is obtained. For an ideal pyramidal geometry tip (Berkovich), the projected contact area to depth relationship is given by

$$A = 24.5 h_c^2$$

The initial unloading contact stiffness, $S = (dP/dh)$ i.e. the slope of the initial portion of the unloading curve is given by

$$S = \frac{dP}{dh} = \frac{2}{\sqrt{\pi}} E_r \sqrt{A}$$

Rearranging the above eqn. we get

$$A = \frac{\pi}{4}\left(\frac{S}{E_r}\right)^2$$

Where the reduced modulus E_r accounts for the fact that the measured displacement includes contribution from both the specimen and the indenter. The reduced modulus is given by

$$\frac{1}{E_r} = \left(\frac{1-\nu_s^2}{E_s}\right) + \left(\frac{1-\nu_i^2}{E_i}\right)$$

Where E_s , ν_s and E_i , ν_i are the elastic modulus and Poisson's ratio of the specimen and the indenter respectively. The hardness has the normal definition

$$H = \frac{P_{max}}{A}$$

Where P_{max} is the maximum indentation force and A is the resultant projected contact area at that load. To determine the area function, a series of indents at various contact depths (normal loads) are performed on fused quartz specimen and the contact area (A) calculated using eqn.

$$A = \frac{\pi}{4}\left(\frac{S}{E_r}\right)^2$$

A plot of the computed area as a function of contact depth is plotted and a fitting procedure is employed to fit the (A) versus (h_c) to a sixth order polynomial of the form

$$A(h_c) = C_0 h_c^{\,2} + C_1 h_c + C_2 h_c^{\,1/2} + C_3 h_c^{\,1/4} + C_4 h_c^{\,1/8} + C_5 h_c^{\,1/16}$$

C_0 for a Berkovich tip is 24.5 while for a cube corner (90°) tip is 2.598. The constants for this equation can then be entered into the Define Area functions section.

The standard procedure for nanoindentation analysis is to use the unloading data for analysis. This has been proven to be a reliable and accurate method for determining contact hardness and stiffness values. The slope of the unloading portion of the curve changes depending upon the number of data points used to fit it. Generally the region between 95% and 20% of the unloading portion of the curve is used to determine the slope and hence the stiffness.

Soft materials behave in a different manner. For instance, aluminium will accommodate almost all of the tip displacement as plastic deformation with no elastic recovery. In such cases linear fitting can be employed. The TriboIndenter

software always fits the unloading curve to a power function. If the data is truly linear, the value for "m" will be 1.000.

After finding the parameters like contact depth, contact stiffness (S), Max Force; equations $A = \frac{\pi}{4}\left(\frac{S}{E_r}\right)^2$ and $\frac{1}{E_r} = \left(\frac{1-\nu_s^2}{E_s}\right) + \left(\frac{1-\nu_i^2}{E_i}\right)$ are employed to find the contact area of each indent. The Elastic modulus of the indenter (E_i) is 1140GPa, and Poisson's ratio (ν_i) is 0.07. If the calibration material is fused Quartz, the elastic modulus (E_s) is 72GPa, and Poisson's ratio (ν_s) is 0.170. The reduced modulus is then 69.6GPa. These values are automatically found when the data is loaded in to the Calculate Area Function section of the software.

The next step is to plot the area verses h_c from the indents. The curve should continually increase with increasing contact depth. Again, this is done automatically in the "Calculate Area Function" section of the software.

Once the data have been plotted in the software, the coefficients (C_1-C_5) for the function can be found. This is done by selecting the "Execute Area Fit". The parameters for the number of coefficients, and C_0 should be set before this is clicked. For 90 degree tips, C_0= 2.598. For Berkovich tips, C_0= 24.5. For area function calibrations done at small displacements, the tip may not be very close to the ideal shape. In these instances, C_0 can also be a fitted parameter.

The software will overlay a plot of the "Tip Area Function" on the actual plotted data to make sure the fit is satisfactory. The points are actually measured

areas using stiffness and elastic modulus. The line is the fitted area function with the following coefficients:

$$Area = 24.5h_c2 + 4.7125e2\ h_c + 6.8042e3\ h_c\ \frac{1}{2} - 7.1121e3\ h_c\ \frac{1}{4}$$

The correct area function parameters may be used for any further indents made at depths in the calibration range.

Machine Compliance

In a typical depth sensing nanoindentation hardness apparatus, the position of the indenter relative to the surface of the specimen, i.e. the depth of an indent during an indentation process is monitored. The measured displacements are the sum of the indentation depth in the specimen and the displacement associated with the measuring instrument, termed as the load-frame compliance. It is important that we measure the load-frame compliance, since at large indentation depths with high modulus; the load-frame displacement can be a significant fraction of the total displacement.

The relationship for the compliance (inverse of stiffness) of the contact between any axisymmetric indenter and an elastically isotropic half-space is given by:

$$C_c = \frac{dh}{dP} = \frac{\sqrt{\pi}}{2}\frac{1}{\sqrt{A}}\frac{1}{E_r}$$

Where E_r is the reduced modulus described by the earlier relationship. E and ν are Young's modulus and Poisson's ratio respectively. Here 'h' is the displacement of the indenter relative to the specimen, P is the load, and 'A' is the

projected area of contact between the specimen and the indenter. To account for elastic displacements of the load-frame of the instrument, the machine compliance, C_m must be added to the contact compliance C_c. We then have the total compliance of the testing system as

$$C_{total} = C_m + C_c = C_m + \frac{\sqrt{\pi}}{2}\frac{1}{E_r}\frac{1}{\sqrt{A}}$$

The hardness of a sample is given by the relationship

$$H = \frac{P_{\max}}{A}$$

Where H is the Hardness, P_{max} is the maximum applied force, and A is the projected contact area. Combining the above two eqns. the following relationship is found:

$$C_{total} = C_m + \frac{\sqrt{\pi}}{2}\frac{\sqrt{H}}{E_r}\frac{1}{\sqrt{P_{\max}}}$$

For Fused Quartz, it is a fair assumption that Hardness and Reduced Modulus are constant at large indentation depths (h_c > 1/3 tip radius) when indented with a Berkovitch indenter, and no cracks are formed. If this assumption is made, a graph of 1/measured stiffness vs. $1/\sqrt{P_{\max}}$ for a series of indents performed in Fused Quartz will yield a straight line with a y intercept of the machine compliance. There are many factors, which can affect the machine compliance of a system. The most common factors are:

Transducer: Different transducers will have different values of compliance. The bridge on Lateral Force transducers makes them more compliant than 1D transducers. Also, other things, such as stiffness of center plate, or thickness of epoxy holding parts together can cause different amounts of compliance.

Indenter tip: The indenter tips can have different amounts of compliance in them as well. Most are hand made, so depending on the amounts of epoxy, or lengths of the shank on the tip, the added compliance can be different.

Sample mounting: If different techniques of mounting samples are used, it is possible that the sample itself could add compliance. Never use a soft material, such as putty or double-sided tape to mount a sample. If a thin layer of stiff glue or epoxy is used, the added compliance is negligible.

Transducer mounting: The transducer must be mounted to the TriboScanner in the same way each time. The transducer should also be level, and seated as well as possible.

Using the above guidelines, the machine compliance should be checked for each transducer-tip configuration. The majority of the time, the same transducer is used, so the machine compliance needs to be checked for each tip. This can be done in conjunction with calculating the tip area function.

Troubleshooting Analysis Problems

There are many types of problems that can be encountered with indentation tests. They can be related to the sample or sample preparation, analysis problems, and occasionally faulty instrumentation. To find out if the problem is instrumentation or sample related, it works best to go back to the standard sample and make indentations on it. In the case of nanoindentation, this sample is fused quartz.

Many imaging related problems are found to be either a contaminated sample or contaminated tip. In this case, clean the tip and the sample and try the image again. If the image is still not correct, check to be sure that the system can image the fused quartz sample. If the fused quartz sample images correctly, then there is some other issue with the particular sample that is being tested. Many softer materials such as polymers will give noisier images, and some cannot be imaged at all.

A different and more subtle problem is inconsistent hardness/modulus results. Many different issues can cause inconsistent results at a constant load. These inconsistencies are usually exaggerated at lower loads, and are usually caused by drift and noise. The noise floor of the TriboIndenter is less than 0.2nm in displacement and less than 0.1μN in force. This means that the noise can be an issue with indentations made at less than 5μN in force and 10nm in displacement. Drift is typically more of a problem than noise at these loads. The drift correction in the software will help a lot with minor drift issues. If drift and noise are not an issue, the inconsistencies could be sample related. To check this, it is best to check the reproducibility on the standard sample (fused quartz).

A slightly more complex inconsistency is when there is varying hardness and modulus at different indentation loads. Most samples will show varying hardness or modulus as the load is changed. This is a real effect. To verify this, indents should be made in the fused quartz to check the consistency of the

values. If the values are not consistent on fused quartz, then there is a different problem that can be the result of a number of issues:

The tip shape has changed. When the modulus of fused quartz is not showing approximately 70GPa, then the tip calibration is wrong. This is the most common issue when inconsistent hardness and modulus values are under question. It is a good idea to check the calibration of the tip as often as possible. The calibration can be easily checked by making a few indents in fused quartz and verifying the hardness and modulus.

The machine compliance value is wrong. If after performing a tip calibration, the modulus is showing 70GPa, but the hardness is showing a linearly increasing or decreasing trend, the problem may be an incorrect Machine Compliance value. When the machine compliance parameter is set too low, the hardness will show an increase with depth. If the correct value for machine compliance needs to be increased a lot to correct the problem, it is a sign that there is an incorrectly mounted transducer or sample.

The tip is dull. With dull tips, the hardness value may show higher or lower values as the force is decreased. This effect is usually seen when the contact depth approaches about 20% of the nominal radius of the indenter tip. The reason for this is that the indents at these loads are very much elastic, and the hardness value will have a large elastic component, causing it to deviate from the mostly plastic value it has at higher forces.

Imaging

Background Subtraction

A tool in the TriboScan software that can become very useful when looking at images is the Background Subtraction. This feature allows the user to remove any tilt or slope in the sample from the image. Possibly with a tilt to the surface and an offset from the zero point of the scanner may be a problem if the tilt is much larger than the fine surface features of the sample. The colors in the image can become saturated from one side of the image to another. Linear regression fits a regression line to all of the data points across a scan line. These regression lines are then fit together to form a level surface. Linear Regression works well unless there is a deep indent or scratch in the image. When there is a very deep point in the scan line, the regression line is fit too low. Then when the scan lines are put together, the lines with very deep points will show up as white streaks. Zone subtraction uses two zones to find the amount of tilt in a sample. The right and left zones are both 16 pixels wide on the image. From both of these zones, the software calculates the slope and removes it from the image. The left and right zones can be moved independently and should be placed so that they are in areas that are representative of the sample as a whole.

Micro materials Nanotester

The Nanotest measures the movement of a stylus in contact with a surface. For indentation measurements, the stylus is impressed into the surface under the influence of an increasing load; after reaching a pre-determined maximum value, the load is reduced and the penetration depth decreases due to elastic recovery of the deformed material. The depth and load are monitored continuously, which allows both hardness and Young's modulus data to be derived. In the scanning module, a static or increasing load is applied as the specimen is moved perpendicularly to the stylus axis, and variations in topography, scratch resistance or frictional force are indicated. The standard NanoTest set-up allows the mechanical properties of films as thin as 20nm to be determined.

Nanotest system

A tiny heater capable of maintaining 500°C and a miniature thermocouple have been added to the diamond stub, close to the tip itself. With both the diamond and sample at the same temperature, heat flow between them does not occur upon contact, thus preventing instantaneous dimensional changes due to thermal expansion.

The hot stage itself consists of a thermally insulating ceramic block, which is attached to the NanoTest sample holder. With the heater at 500°C, the increase in temperature behind the ceramic block is typically less than 1°C. Temperature controllers with automatic tuning are used for both the main hot stage and the diamond heater.

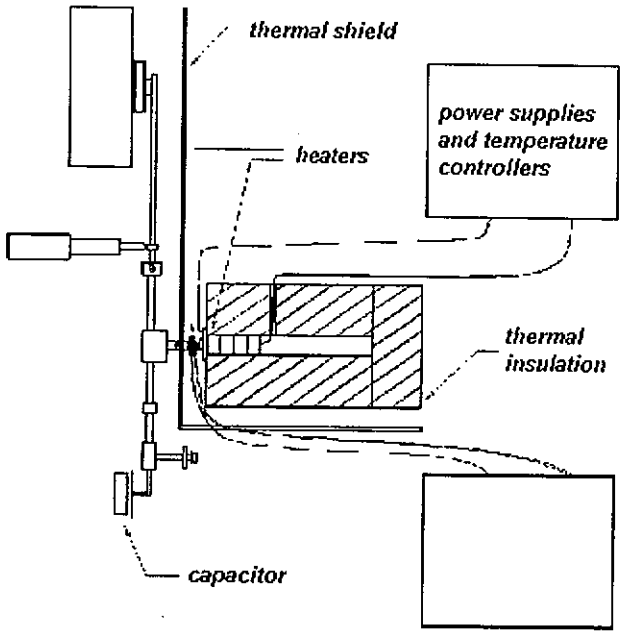

Nanotest indentation analysis

When a material which experiences both elastic and plastic deformation is strained by indentation, the behaviour during the loading-unloading cycle is determined by the degree of imposed strain relative to the yield strain. For a pyramidal indenter, the representative imposed strain is given by:

$$e_r = 0.2 \tan b$$

Where b is the angle between the face of the indenter and the original surface. The yield strain is given by Y/E, where E is Young's modulus and Y is the yield stress. For many indentations:

If $\tan b\ (E/Y) < 2$, the deformation is primarily elastic

If $2 < \tan b\ (E/Y) < 50$, the deformation is elastic + plastic

If $\tan b\ (E/Y) > 50$, the deformation is primarily plastic

Hardness and Modulus: Linear Fitting

The Meyer hardness is defined by $H = P_{max} / A_{max}$ where P_{max} is the maximum load and A_{max} is the projected contact area at maximum load calculated from the contact depth h_c . For a material exhibiting elastic recovery, it is assumed that the contact area between the indenter and the material remains constant and moves elastically during unloading. A further assumption is that the plastic area is always equal to the contact area; in practice, the plastic area may be larger or smaller. For a constant cylindrical contact area, the elastic recovery in this case is described by the equation:

$$P = 2E_r a d_e$$

Where

P = Maximum load

E_r = Reduced modulus

$$1/E_r = (1 - n^2)/E + (1 - n_0^2)/E_0$$

n = Poisson's ratio for the sample

n_0 = Poisson's ratio for the indenter (0.07)

E = Young's modulus for the sample

E_0 = Young's modulus for the indenter (1141 GPa)

a = Radius of contact area

d_e = Elastic deformation

Linear unloading down to the contact depth hc at zero load is predicted. This is never observed since the indent begins to "open", i.e., "a" changes, leading to a departure from linearity which is greater in materials with a higher

$H:E$ ratio. However, the initial part of the curve is reasonably linear for most materials, and the plastic depth is therefore defined by fitting the first 20% of the data points to a straight line, extrapolating this to zero load, and taking the intercept on the depth axis as the final plastic depth.

For a homogeneous material and perfect indenter geometry, an Elastic Recovery Parameter, R, is defined. This, which is indicative of the slope of the unloading curve, is related to the $H:E$ ratio as follows:

$$R = (h_{max} - h_c)/h_c = H(1 - n^2)(k_p)^{0.5}/2E$$

Where k is a diamond geometry factor.

From Eq. $P = 2E_r a d_e$, the unloading slope is given by:

$$C = p^{0.5}/(2E_r A^{0.5})$$

After correction of the data for frame compliance, this allows the modulus of the material to be determined.

Hardness and Modulus: Power Law Fitting

After frame compliance correction, the Depth vs. Load raw data is fitted to a power law expression of the form

$$P = a(h - h_f)^m$$

Where a, h_f and m are constants. This is justified on the basis of elasticity theory. The true contact depth is then determined from the expression:

$$h_c = h_{max} - e\,(CP_{max})$$

Where C is the contact compliance equal to the tangent at maximum load. The value of e depends on the indenter geometry, e.g., for a paraboloid of revolution

it is 0.75. Experimentally, the Berkovitch diamond produces the elastic recovery behaviour expected of a paraboloid of rotation

Spherical indentation

The elastic behaviour of contacting spheres was first described by Heinrich Hertz in 1882. Hertzian analysis predicts a contact circle of radius a given by the equation:

$$a = (3PR/4E^*)^{1/3}$$

Where P is the applied load, R is the radius of the sphere, and E^* is the reduced modulus given by:

$$1/E^* = (1-n_1^2)/E_1 + (1-n_2^2)/E_2$$

Where the subscripts 1 and 2 refer to the two contacting materials.

In static Hertzian contact, the maximum shear stress occurs at a distance of about half the contact radius immediately below the point of contact. Yielding therefore first takes place below the surface, and generally this occurs when

$$P_m = 1.1Y$$

Where P_m is the mean pressure and Y is the yield stress. If the mean pressure is less than this, the contact remains elastic.

An indentation process may produce: (i) a reversible, elastic deformation; (ii) a permanent, plastic deformation; or (iii) both plastic and elastic deformation. The detailed behaviour depends on the ratio of the actual strain to the yield strain of the material. Low ratios (< 2) produce elastic behaviour; high ratios (> 50) produce plastic behaviour. The actual strain is given by tan$b$, where b is the

angle between the indenter and sample surfaces, so it is clear that a spherical indenter will behave in a fundamentally different way from a pyramidal indenter. In the case of a Vickers pyramid, for example, b is constant and the strain is therefore constant (about 8%), regardless of depth. For a spherical indenter, b, and therefore the strain, increases as the indentation depth increases. A series of spherical indentations with progressively higher maximum load can therefore produce results ranging from purely elastic to elastic + plastic, and, furthermore, can yield curves of Stress vs. Strain.

In the NanoTest, multiple load - unload cycles with increasing maximum loads are performed at one point. From this data and the known diamond radius, the contact area is determined and hardness, Young's modulus, stress and strain are calculated. The contact areas are corrected for possible "piling up" or "sinking in" around the contact perimeter.

Diamond Area and Frame Compliance Calibration

No diamond is perfectly sharp, so it is necessary to determine the real contact area as a function of contact depth. The NanoTest has an automatic procedure for this, which utilises results from a series of indentations performed at different loads in fused silica. Using measured contact compliance values and literature values for the properties of fused silica (E = 72 GPa and n = 0.17), Eq. 2 allows a series of contact area values to be calculated. A least squares fitting procedure is then used to obtain a quadratic diamond area function given by A =

$ah_c^2 + bh_c$, where a and b are constants and h_c is the contact depth. An ideal Berkovitch indenter has a contact area given by $A = 24.5h_c^2$.

For the determination of material elastic properties, it is necessary to subtract any small elastic deformation of the instrument itself. In the NanoTest, automatic frame compliance determination is based on elastic recovery data obtained from well-documented reference materials. Again, fused silica is normally used.

Depth profiling of hardness and modulus

The Load-Partial Unload Technique

The NanoTest can be used to determine hardness and Young's modulus as a function of depth at a single point. This is achieved by producing a series of load-unload hysteresis curves with progressively increasing load, but where the indenter remains in contact with the point of interest throughout. This is significantly faster than producing a corresponding series of separate indentations since diamond-specimen contact has to occur only once. To ensure that contact is maintained, only partial unloading is performed. During reloading, the Depth vs. Load data is essentially superimposed on the previous unloading curve until the additional load increment is applied, when further plastic deformation takes place.

A possible alternative approach is known as Continuous Stiffness Measurement. Here, an extremely small sinusoidal oscillation is superimposed on the load ramp and the dynamic response of the contact is determined. Theoretically, this permits the instantaneous stiffness to be determined. However, this technique requires knowledge of 8 parameters, including the instrument damping coefficient. Contact damping and contact frictional effects should also be taken into account, but these parameters are not measurable. Clearly, implementation of the load-unload procedure is relatively straightforward.

In addition, to measure the mechanical properties of normal materials using indentation methods, it is necessary to hold the load periodically in order to allow time-dependent processes to occur. In such cases, continuous stiffness results still show discrete points in curves of Hardness vs. Depth and Modulus vs. Depth.

3.2 Theory on Computer Simulations Research

Molecular dynamics (MD) is a computer simulation technique where the time evolution of a set of interacting atoms is followed by integrating their equations of motion. In molecular dynamics we follow the laws of classical mechanics, and most notably Newton's law:

$$F_i = m_i a_i$$

for each atom i in a system constituted by N atoms. Here, m_i is the atom mass,

$$a_i = \frac{d^2 r_i}{dt^2}$$

its acceleration, and F_i the force acting upon it, due to the interactions with other atoms. Molecular dynamics is a deterministic technique: given an initial set of positions and velocities, the subsequent time evolution is in principle completely determined. In more pictorial terms, atoms will ``move" in the computer, bumping into each other, wandering around (if the system is fluid), oscillating in waves in concert with their neighbors, perhaps evaporating away from the system if there is a free surface, and so on, in a way pretty similar to what atoms in a real substance would do.

The computer calculates a trajectory in a $6N$-dimensional phase space ($3N$ positions and $3N$ momenta). However, such trajectory is usually not particularly relevant by itself. Molecular dynamics is a statistical mechanics method. It is a way to obtain a set of configurations distributed according to some statistical distribution function, or statistical ensemble.

According to statistical physics, physical quantities are represented by averages over configurations distributed according to a certain statistical ensemble. A trajectory obtained by molecular dynamics provides such a set of configurations. Therefore, a measurement of a physical quantity by simulation is simply obtained as an arithmetic average of the various instantaneous values assumed by that quantity during the MD run.

Statistical physics is the link between the microscopic behavior and thermodynamics. In the limit of very long simulation times, one could expect the phase space to be fully sampled, and in that limit this averaging process would yield the thermodynamic properties. In practice, the runs are always of finite length, and one should exert caution to estimate when the sampling may be good (``system at equilibrium") or not. In this way, MD simulations can be used to measure thermodynamic properties and therefore evaluate, say, the phase diagram of a specific material.

Beyond this ``traditional" use, MD is nowadays also used for other purposes, such as studies of non-equilibrium processes, and as an efficient tool for optimization of structures overcoming local energy minima.

To provide information on the dislocated lattice, the concept slip vector is used, which is given by [53],

$$s^{\alpha} = -\frac{1}{n_s} \sum_{\beta \neq \alpha}^{n} (x^{\alpha\beta} - X^{\alpha\beta}),$$

where x and X are the vectors linking the atom α with all its nearest neighbours β in the current and reference positions, n_s is the number of slipped neighbours, and n is the number of nearest neighbours to atom α. Reference position is the arrangement of atomic positions associated with the zero mechanical stress. The term slip vector is used as a synonym for the Burgers vector. The expression will result in the Burgers vector for the slip of adjacent atomic planes, where the atom lies on one of those planes.

The atoms with velocity v_i has some form of energy $E = \frac{1}{2} m v_i^2$.

The Boltzmann equation is given by, $P_{E_i} = \left[e^{-E/kT} \right]$, where k is the Boltzmann constant, T is the temperature.

Shear stress or pressure is given by, $\sigma_{ij} = (\sigma_{11} + \sigma_{12} + \sigma_{33})$ is used to plot the burgers vector. This is necessary to find the core of nucleation.

Temperature changes are usually achieved by enabling a device in the code, which brings the system to a desired temperature by rescaling the velocities, and this may be accomplished by using the equation (Furio Ercolessi [1997]-www.fisica.uniud.it),

$$v\left(t + \frac{\Delta t}{2}\right) = \sqrt{\frac{T_o}{T(t)}} v(t) + \left(\frac{1}{2}\right) a(t) \Delta t$$

Where T_o is the desired temperature and $T(t)$ is the instantaneous temperature.

Several schemes developed to construct many-atom potentials for metals essentially depends on functional form (Furio Ercolessi [1997]-www.fisica.uniud.it),

$$V = \frac{1}{2} \sum_{\substack{i,j=1 \\ (j \neq i)}}^{N} \phi(r_{ij}) + \sum_{i=1}^{N} U(n_i)$$

Where $\phi(r)$ is a two-body part, and $U(n)$ is a function giving the energy of an atom as a function of a generalized coordination n. n for a given atom is in turn constructed as a superposition's of contributions from neighbouring atoms.

The temperature T is directly related to the kinetic energy (Furio Ercolessi [1997]- www.fisica.uniud.it) by the well-known equipartition formula, assigning an average kinetic energy $\frac{k_B T}{2}$ per degree of freedom:

$$K = \frac{3}{2} N k_B T = \Sigma_i \frac{1}{2} m v_i^2$$

An estimate of the temperature is therefore directly obtained from the average kinetic energy K. For practical purposes, it is also common practice to define an ``instantaneous temperature" $T(t)$, proportional to the instantaneous kinetic energy $K(t)$ by a relation analogous to the one above. Simulation uses this equation to accommodate the temperature effect. Where, k is the Boltzmann constant, T is the temperature; N is the total number of atoms.

The average potential energy V is obtained by averaging its instantaneous value, which is usually obtained straightforwardly at the same time as the force computation is made. In case of two body interactions is given by (Furio Ercolessi [1997]- www.fisica.uniud.it),

$$V(t) = \sum_i \sum_{j>i} \phi\left(\left|r_i(t) - r_j(t)\right|\right)$$

The instantaneous kinetic energy is of course given by (Furio Ercolessi [1997]- www.fisica.uniud.it),

$$K(t) = \frac{1}{2} \sum_i m_i [v_i(t)]^2$$

and is therefore extremely easy to compute. We will call K its average on the run.

The number of dislocation loops, $n = \frac{\Delta h_{\max}}{b}$

Where b is the magnitude of burgers vector. Taking b as 0.3 nm approximately and n as 50 approximately.

Since the depth of indentation is typically much less than R, hertzian theory tells us that the contact radius, a, for an axisymmetric indenter with tip R is approximately,

$$\frac{a}{R} = \left(\frac{\delta}{R}\right)^{1/2} = \left(\frac{3P}{4E^{*}R^{2}}\right)^{1/3}$$

Each atom in the substrate interacts with the idealized indenter via the potential [9],

$$V(r) = A\theta(R\text{-}r)(R\text{-}r)^{3}$$

Where R is the radius of the indenter, r is the distance of the atom from indenter sphere center, $\theta(R\text{-}r)$ is the standard step function, A is the force constant. The forces are evaluated from eqn. (Furio Ercolessi [1997]- www.fisica.uniud.it),

$$F_i = -\sum_{j \neq i} \left(\phi'(r_{ij}) + \left[U'(n_i) + U'(n_j)\right]\rho'(r_{ij})\right)\frac{r_{ij}}{r_{ij}}$$

In practice there could be small fluctuations in the total energy, in a typical amount of, say, one part in 10^4 or less. These fluctuations are usually caused by errors in the time integration, and can be reduced in magnitude by reducing the time step if considered excessive.

Slow drifts of the total energy are also sometimes observed in very long runs. Such drifts could also be originated by an excessive Δt. Drifts are more

disturbing than fluctuations because the thermodynamic state of the system is also changing together with the energy, and therefore time averages over the run do not refer to a single state. If drifts over long runs tend to occur, they can be prevented, for instance by breaking the long run into smaller pieces and restoring the energy to the nominal value between one piece and the next. A common mechanism to adjust the energy is to modify the kinetic energy via rescaling of velocities.

A final word of caution: while one may be tempted to achieve ``perfect'' energy conservation by reducing the time step as much as desired, working with an excessively small time step may result in waste of computer time. A practical compromise would probably allow for small energy fluctuations and perhaps slow energy drifts, as a price to pay to work with a reasonably large Δt.

Chapter 4 Experimental Measurements and Results

4.1 Introduction

Experimental studies of the mechanical response of materials to nanoindentation have not been fully undertaken under different thermal loading. The ability to perform nanotest measurements at elevated temperatures opens up significant new possibilities. The temperature response of different metals is still not thoroughly understood. The behavior of the material is different when subjected to temperatures deviating from the normal room temperature. Thorough study of the behaviour of the materials at different temperatures is very important for the design and applications of materials at different operating conditions. Understanding the critical relationships between the temperature and mechanical properties of metals is very important in design and selecting suitable materials for real-life environments depending on the thermal loading.

In the present investigation, the effects of temperature on properties of metals are studied. The experiments are performed with tailor made Berkovitch tip of radius 100 nm at temperatures of 265 K, 388 K, 348 K, 473 K and 623 K. Single-crystals of tungsten, gold, Aluminum and polycrystalline copper are considered for the investigation. The indentation is performed for bcc tungsten, FCC gold on the (111) and (110) crystallographic surfaces, single crystal aluminium with (100) crystallographic orientation and polycrystalline copper at different temperatures. The behaviour of the material during loading and unloading are analyzed to understand the temperature effects on the

reconstruction of the material during the removal of load. Emphases are placed on the defects generation mechanisms during the elastic plastic contact of crystals. Special attention has been devoted to the elastic response before the onset of plastic yield.

4.2 Methodology

The Nanoindentation experimental setup described in chapter 3 is used to perform the experiments. The experiments are performed with tailor-made Berkovitch tip of radius 100 nm at temperatures of 265 K, 388 K, 348 K, 473 K and 623 K, to study the temperature dependence of various metals. To perform the experiment at high temperature, insulating material is used to protect the piezoelectric setup of the indenter. A small heater capable of maintaining a constant temperature has been added to the stage. The hot stage itself consists of a thermally insulating ceramic block, which is attached to the Nanotest sample holder. With the heater at high temperature, the increase in temperature behind the ceramic block is typically less than 1 degree. The sample is placed on the temperature stage made of copper. The temperature stage is capable of producing different temperatures. Flat surfaces away from steps were chosen for nanoindentation by imaging the surface with Atomic Force Microscope (AFM) at 7X magnification to locate a smooth and defect free surface. The sample surface is brought to a constant temperature before the indentation for each experiment. A new attachment is made to circulate the dry nitrogen gas to avoid the ice formation during the low temperature experiments. The loading rate is kept constant for different temperatures experiments. The size of the sample is 5

mm thick and 50mm in diameter. It takes about 15 minutes to reach the required temperature. Amount of force on the sample during imaging is 2μN. The topography and gradient images were captured to show the surface morphology after the indentation. In-situ imaging provides the capability to observe and quantify material damage while minimizing time for material recovery. In the case of thin hard films on soft substrates, for instance, the indentation depth should generally not exceed 10% of the film thickness in order to preclude any influence of the substrate.

It is very difficult to polish the single crystals by normal methods. Instead, the sample is prepared with an advanced technique using the ultra precision machining technique producing a very fine surface. This method does not affect the orientation. But in case of other polishing methods, there is the possibility of changing the orientation of the sample. This method also avoids the problem of surface oxide formation compared to other methods.

4.3 Results for Copper

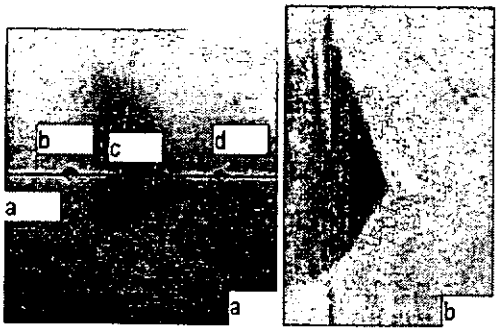

Figure 4.1. AFM images of sample after indentation at 265 K, (a) Topography image at 10μ, (b) gradient image at 10μ.

Figures 4.1(a) and (b) above are the AFM images. Figure 4.1(a) shows hillock formation due to the pile up effect in case of indentation at a load of 10,000 μN and loading rate of 2,000 μN/s. Pile up height is about 25.4 nm. The pile up occurs on all sides near the indented surface at low temperatures, and is due to the restriction to dislocation movements and due to the rotation of the lattice during nanoindentaion. We can also see a wave pattern as the indenter goes down as shown in figure 4.1(b). The positions b, d on the figure shows the topmost regions of pile up. The position c shows the bottom most region of the indentation.

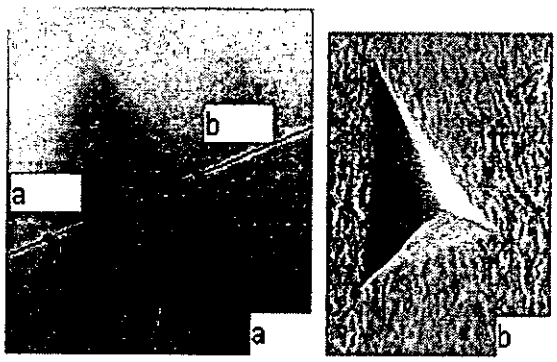

Figure 4.2. AFM images of sample after indentation at 388 K, (a) Topography image at 8μ, (b) gradient image at 8μ.

Figures 4.2(a) and (b) above are the AFM images. Figure 4.2(a) shows that the pile up reduces at high temperature due to the global nature of the relaxation. As evident from the very early occurrence of the initial burst on the graph, the material accommodates inside, instead of more pile up.

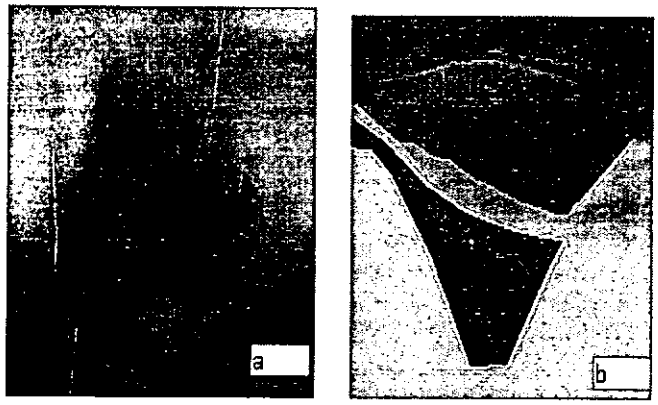

Figure 4.3. 3D view of sample after indentation at 265 K. (a) top view at 4000x2500 nm, side view at 4000x2500 nm. Red colour shows topmost region and sky blue shows pileup area.

Figure 4.3 shows the three-dimensional view of the sample after indentation. Figure a shows the top view at 4000x2500 nm. A clearly visible striped pattern seen on the inside and outside of the surface of indentation may be due to the pressure on the adjacent vertical layers of material. Red colour shows the two extreme regions of the sample after indentation and the patches of sky blue around the indentation shows the hillocks.

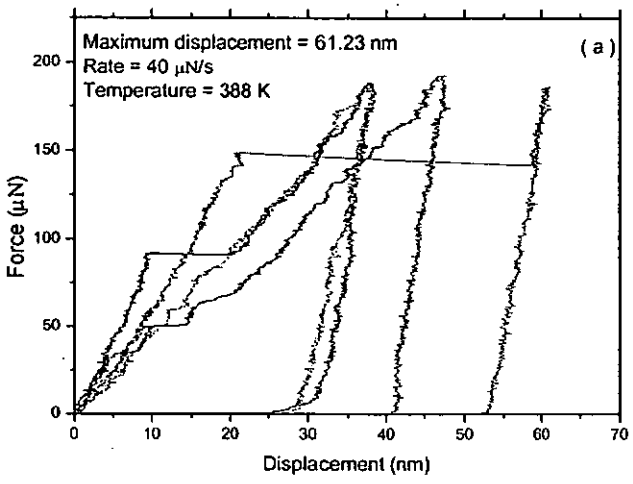

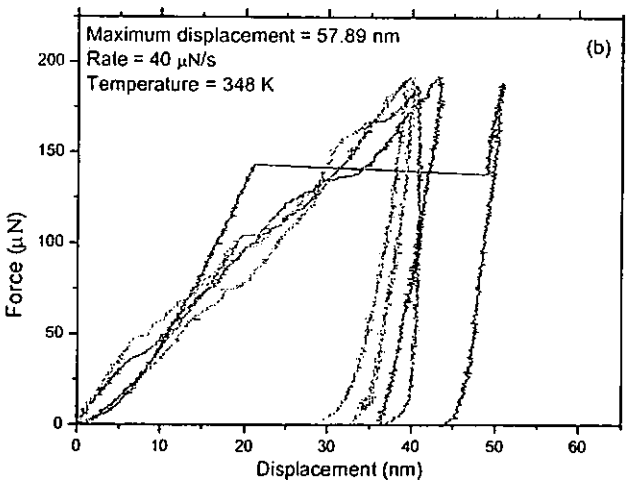

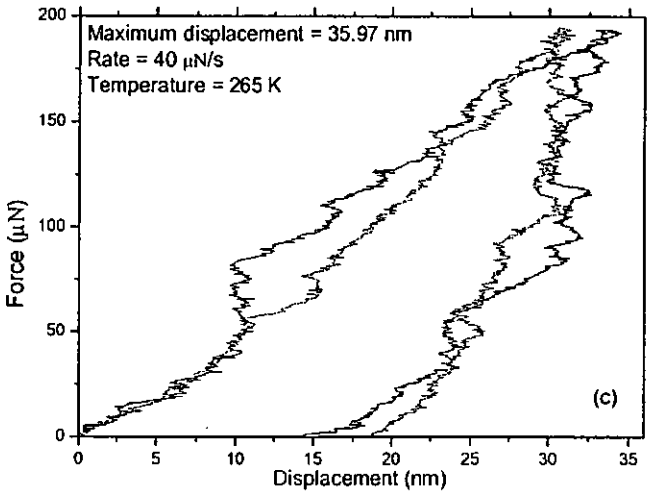

Figure 4.4. Comparison of initial burst at 200μN and 40 μN/s at different temperatures, (a) 388 K, (b) 348 K, (c) 265 K.

Figure 4.4 shows the onset of the first observable strain burst at different temperatures for a given load and loading rate. Different curves in each figure are results of different tests performed under the same conditions. The variation among the curves for same conditions may be due to the different crystallographic orientations of the polycrystalline copper sample. The different locations on the sample have different plastic behavior depending on the crystallographic orientation. Figure 4.4(a) shows that, compare to the lower

temperature cases, the initial strain burst at 388 K occurs at a smaller depth but has a larger displacement. We note with interest that the onset of the first burst occurs at different penetration depths for the same sample under the same testing conditions. This may be due to the different crystallographic orientations of indented grains of the polycrystalline sample. Indeed, theoretical investigations show that different crystallographic surfaces in copper [26] respond substantially differently under nanoindentation. Figure 4.4(b) at 348K shows that the initial strain burst occurs at a penetration depth larger than for the higher temperature experiment. At the same time, the strain burst is smaller. In Figure 4.4(c), at 265 K, the initial burst is not clearly visible. The nanoindentation experiment of Bahr et al [2] shows that the load at which the yield point occurs does not depend on temperature in the range of 300K - 388K. As mentioned by Zimmerman et al [53], both in experimental and theoretical studies, the stacking fault energies show little dependence on temperature below 400 K. The nanoindentation experiment on Al single and polycrystals at room temperature by Gouldstone et al [17] also presents similar results for the initial burst as shown in our results.

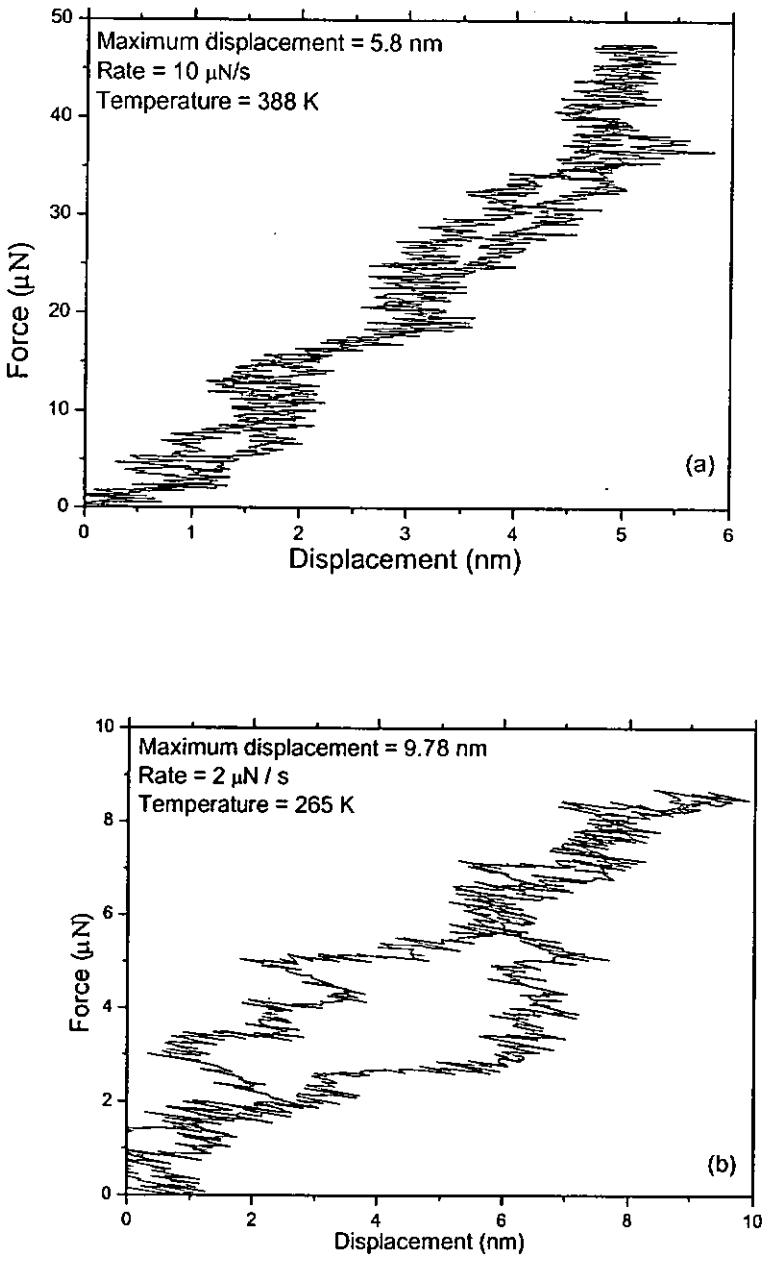

Figure 4.5. Comparison of elasticity range, (a) 388 K, 50 μN, 10 μN/s, (b)265K,10 μN, 2 μN/s.

The elastic range is the maximum deformation of the material (maximum depth) for which the material can regain its original shape completely after indentation. Figure 4.5 (a) and (b) above shows the complete elasticity range at

different temperatures. Figure 4.5(a) at 388 K shows the complete elastic curve if the load is controlled up to 50 μN. The distance reached within the elastic range is about 5 nm. But at 265 K, the elastic curve is obtained only if the loading is limited to 10 μN. The penetration is about 10 nm. This shows the shorter elastic range but high load for high temperatures as previously explained in figure 4.4, but longer elastic range and low load at low temperatures. During the indentation, the accumulated elastic energy in the indented region is partially released by the nucleation of dislocations. Upon retracting the indenter after the first yield, the pressure due to the compressive strain in the defect induces restoring forces that anneal the plastic deformation and the structure regains its original shape.

The nanoindentation experiment on Al single and polycrystals at room temperature by Gouldstone et al [17] also presents a similar pattern of effective elastic region as shown in our results. Also the elastic behaviour on E52100 steel is found from nanoindentation experiments at micro materials company [19] using spherical indenter.

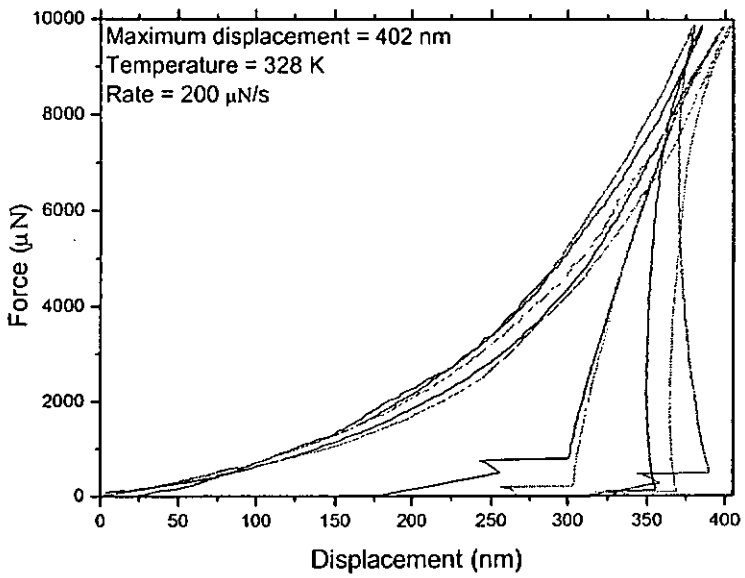

Figure 4.6. Showing the recovery process at the end of unloading at 328 K, 10,000μN, 200μN/s.

Figure 4.6 shows the recovery process at the end of unloading at different temperatures and at maximum load of 10,000μN and 200μN/s. The end of unloading curve in figure 4.6 at 328K shows the sudden release of the strain energy as the material is trying to recover for a short distance. This phenomenon is particularly clear at 328 K. This is not clearly shown at other temperatures.

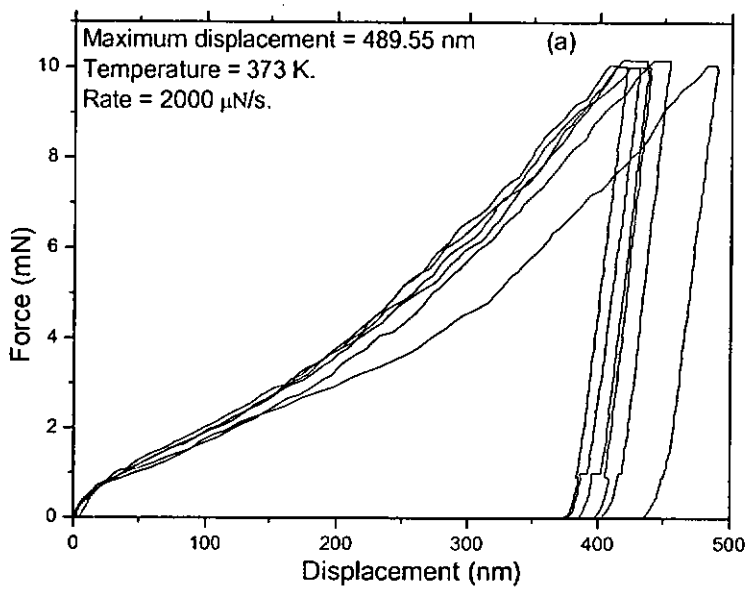
Maximum displacement = 489.55 nm
Temperature = 373 K.
Rate = 2000 μN/s.
(a)
Force (mN)
Displacement (nm)
0
2
4
6
8
10
0
100
200
300
400
500

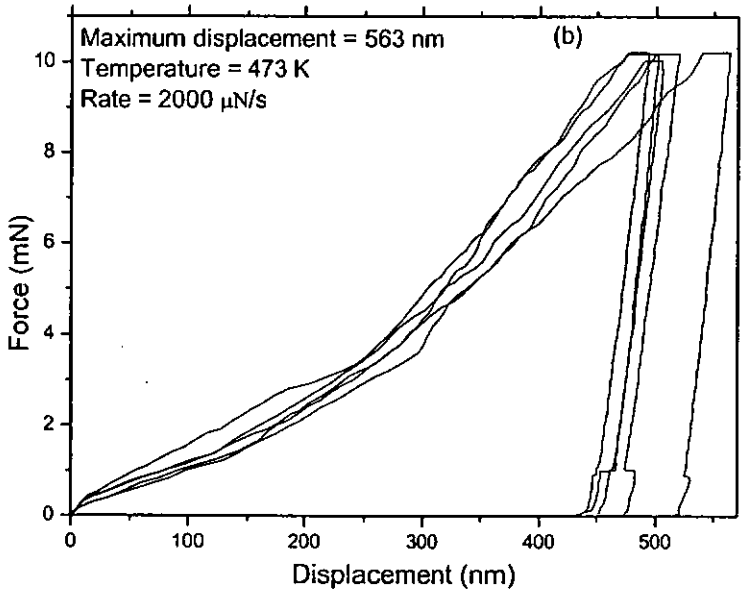
Maximum displacement = 563 nm
Temperature = 473 K
Rate = 2000 μN/s
(b)
Force (mN)
Displacement (nm)
0
2
4
6
8
10
0
100
200
300
400
500

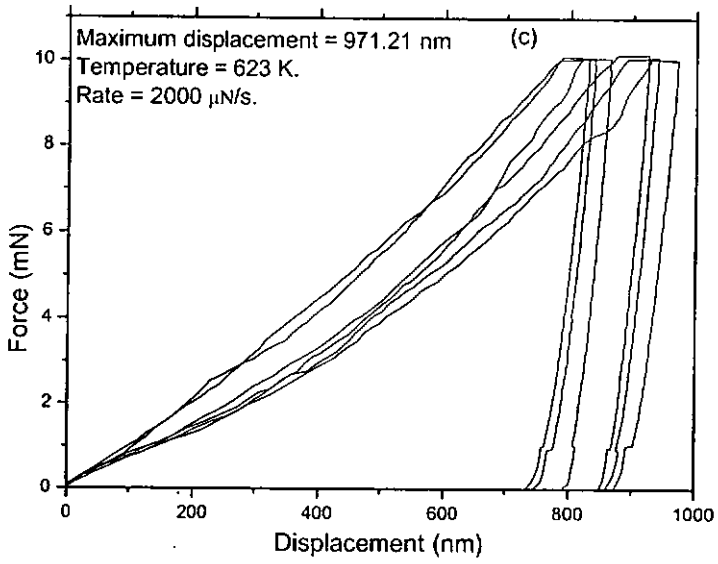

Figure 4.7. Showing the softening effects, (a) 373K, (b) 473K, (c) 623 K.

Figure 4.7 shows the softening effects at different temperatures. The exact data on the amount of softening will enable the proper selection of materials for different thermal loading conditions. The softening effects are due to increase in temperature and these softening effects produce increased plasticity. At high temperatures, the material is subjected to high plastic deformation. But it is a global deformation, instead of local burst causing the dislocations unlike the periodic burst in case of low temperature.

There are clear bursts showing the nucleation of dislocations. The pile up is clearly visible. The pile up of the material is due to the rotation of the lattice during nanoindentation in order to conserve the volume when the indenter is moving into the sample. We can also notice that there is an elastic rebound at the end of loading. The tensile stress can reduce the pile up.

It is clear from the penetration depths read from the curves that significant softening occurred at the higher temperatures. It is also noted that the elastic recovery is reduced at higher temperatures.

Table 4.1. Comparison of data for different temperatures at 1000 μN, 200 μN/s.

Temp/constants	h_{max},nm	$h_{plastic}$,nm	H,Gpa	E,Gpa	S,μN/nm
265 K	94.60	86.03	3.05	124.20	80.33
	101.60	92.96	2.64	153.4	105.90
388 K	120.80	105.96	2.09	64.50	49.80
	125.40	110.94	1.93	63.30	50.76

Table 4.2. Comparison of data for different temperatures at 10,000 μN, 2000 μN/s.

Temp/constants	h_{max}, nm	$h_{plastic}$, nm	H, Gpa	E, Gpa
373 K	437.43	408.92	2.07	106.29
	430.21	399.98	2.14	101.19
	438.99	411.72	2.02	109.33
473 K	505.63	472.34	1.55	78.33
	520.02	482.48	1.52	69.32
	501.41	475.01	1.57	100.06
623 K	940.57	902.38	0.45	36.99
	971.21	928.97	0.43	32.43
	925.00	890.55	0.46	41.58

From table 4.2, for 265 K, 10,000 μN, 2,000 μN/s., it is noticed that the difference between $h_{plastic}$ and h_{max} is 7 nm. But in case of 388 K, it is 30 nm. For 473 K, it is 37 nm. For 623 K, it is 40 nm. This phenomenon shows that the plasticity range increases, as the temperature increases causing an increased failure of the material at high temperatures. In other words, the elastic recovery reduces at higher temperatures.

The hardness decreases and displacement increases as the temperature increases. From table 4.1 it is noted that the difference between $h_{plastic}$ and h_{max} at 388 K for 1000 μN, 200 μN/s, is less than that of 373 K, 10,000 μN and 2000 μN/s. It shows that the loading rate also has an effect on the range of plasticity. Also it is noted that the value of elastic modulus (E) is high when the difference between $h_{plastic}$ and h_{max} and h_{eff} is high. The Hardness (H) does not depend on this difference. The value of Hardness (H) is found to decreases when the displacement (h) is high, as noticed from the table, as also evident from Roger smith et al [38] results. It is also noted that the elastic recovery reduces at higher temperatures. The defect generation and motion causes the plastic deformation, which is reflected in the pile up patterns. The pop-ins shown by the p-h curves corresponds to the formation of dislocations. The contact pressure (nanohardness) increases with decreasing indentation depth.

4.4 Results for Tungsten

The temperature response of properties of tungsten at high temperature has still not been thoroughly understood. Not much research is focused on the tungsten at high temperature as referred by Zimmerman et al [53]. The effect of temperature on the dislocation nucleation process is not well understood. Detailed experimental analysis of the effect of temperature on Tungsten is necessary to understand the behaviour of this metal in real time conditions. The two samples W (111) and W (110) surface orientations are considered for the investigation at various temperatures.

The normal nanoindentation with tailor-made Berkovitch tip of radius 100 nm, on the single crystal tungsten (111) and (110) surface orientations at various temperatures has been conducted, with the aim to study the behaviour at high temperature. The size of the sample is 2mm thick and 9mm in diameter. Amount of force on the sample during imaging is 2μN.

4.4.1 Results for W (111)

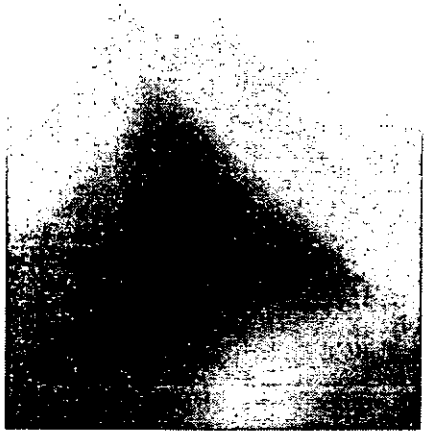

Figure 4.8. AFM image (Topography) showing hillock formation (pile up)

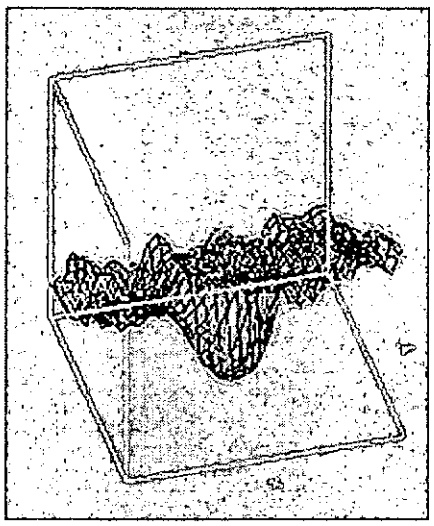

Figure 4.9. 3D view of the sample after indentation. Shows the fracture of the material under the indenter.

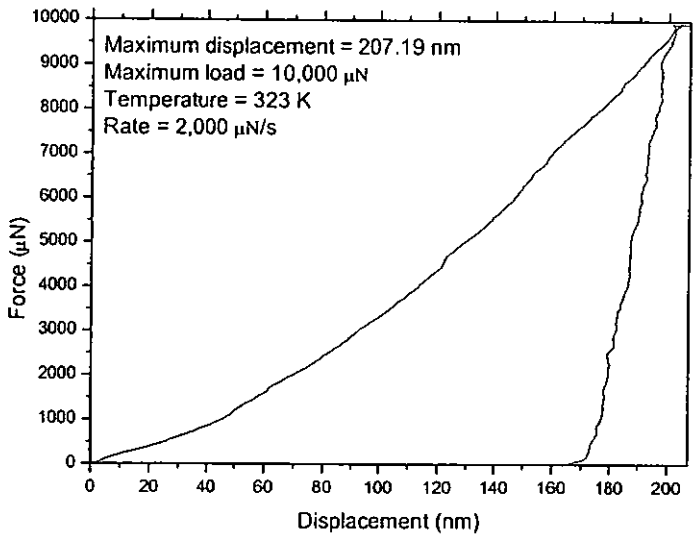

Figure 4.10. Graph showing the loading and unloading pattern at 323 K.

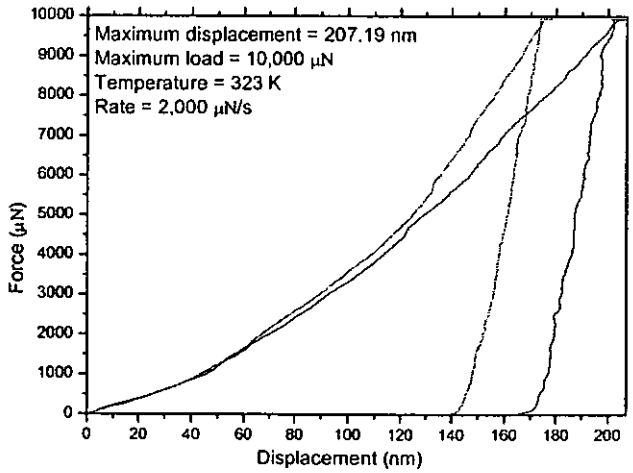

Figure 4.11. Graph showing the periodic burst and strain hardening effects at 323 K.

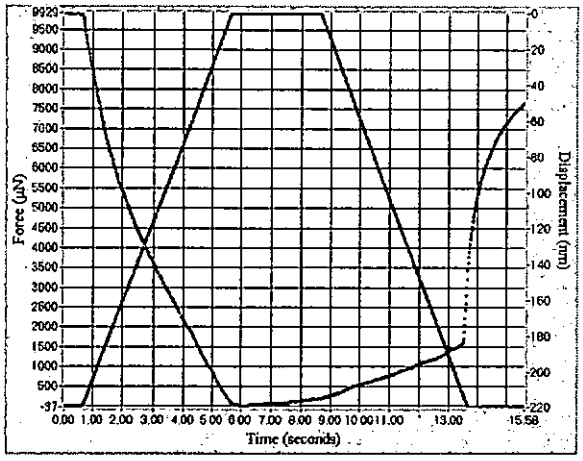

Figure 4.12. Shows the time, displacement, force curve.

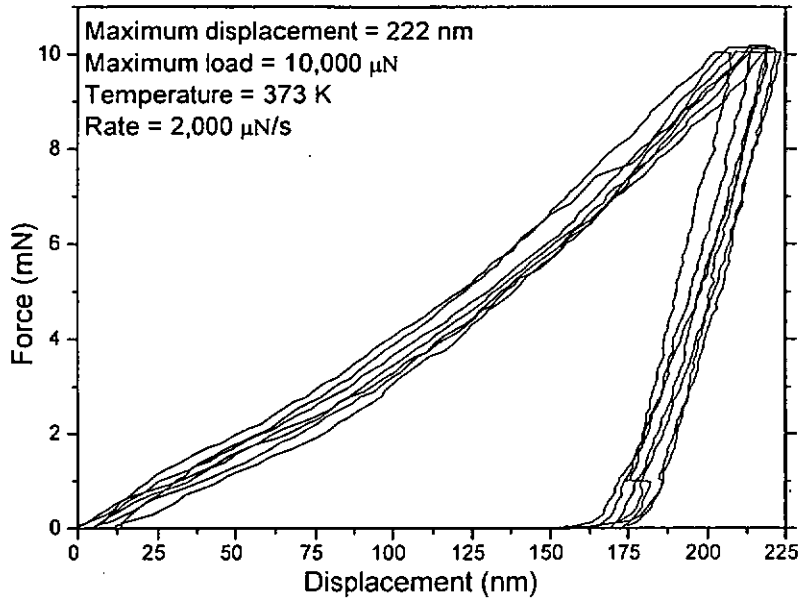

Figure 4.13. Graph showing the loading and unloading pattern at 373 K, 10,000μN, 2,000μN/s, The sudden burst at the end of unloading is noticed from the above graph.

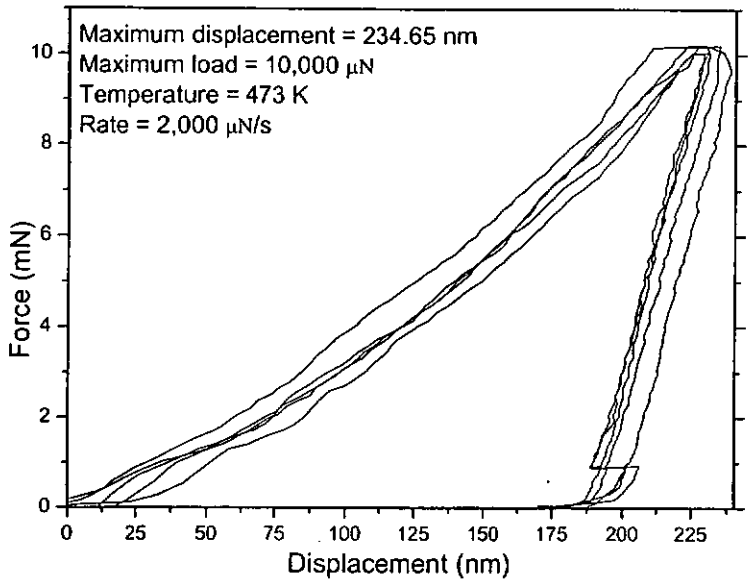

Figure 4.14. Graph showing the loading and unloading pattern at 473 K, 10,000μN, 2,000μN/s, The sudden burst at the end of unloading is noticed from the above graph.

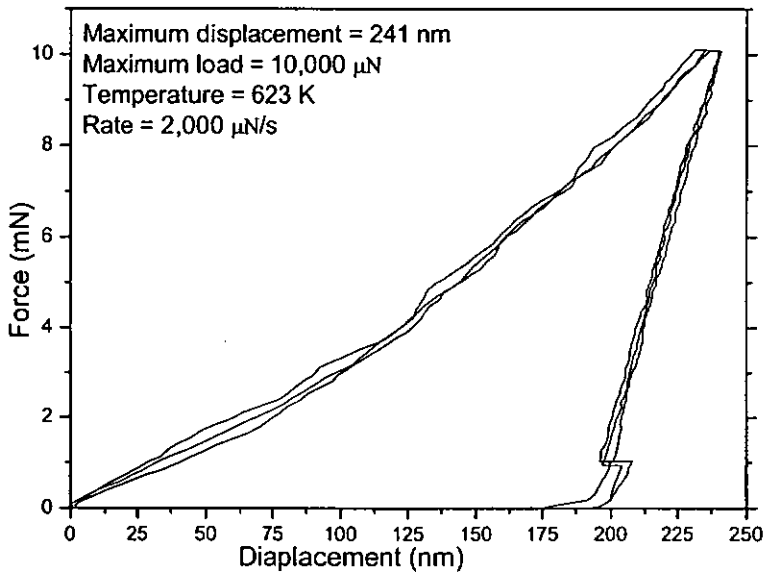

4.15. Graph showing the loading and unloading pattern at 623 K, 10,000μN, 2,000μN/s, The sudden burst at the end of unloading is noticed from the above graph.

Table 4.3. Data at 1000 μN, 200 μN/s.

Temp/constants	h_c,nm	H,Gpa	E,Gpa
265 K	79.7	3.38	236.2
	87.5	2.89	246.5
	85.9	2.98	205.4

The data from the above table shows the effect of force and rate.

Table 4.4. Comparison of data for different temperatures at 10,000 μN, 2,000 μN/s.

Temp/constants	h_{max}, nm	$h_{plastic}$, nm	H, Gpa	E, Gpa
373 K	218.94	190.32	8.46	214.01
	218.6	187.86	8.58	199.76
	220.18	191.35	8.38	211.69
	221.96	197.47	7.92	241.98
	207.26	179.60	9.25	229.99
	214.01	186.54	8.73	226.02
473 K	234.65	200.88	7.68	172.96
	231.05	195.15	8.01	165.32
	229.11	193.27	8.15	167.04
	230.71	197.88	7.94	181.36
623 K	241.06	200.21	7.67	142.28
	240.34	200.67	7.65	146.31
	240	203.89	7.43	158.67

4.4.2 Results for W (110)

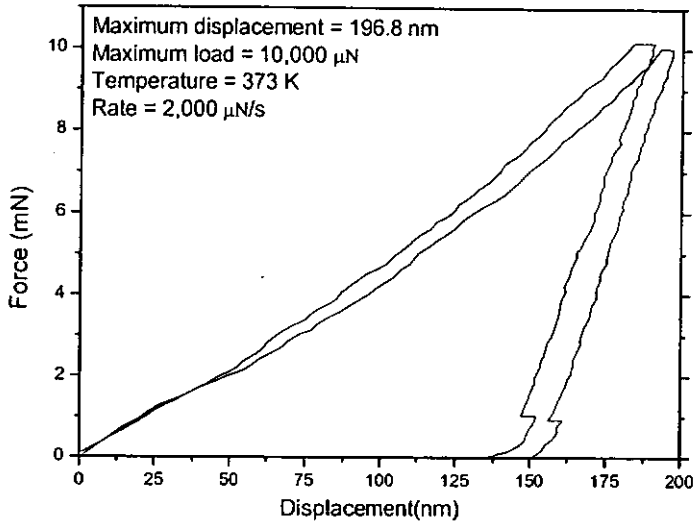

Figure 4.16. Graph showing the loading and unloading pattern at 373 K, 10,000μN, 2,000μN/s, The sudden burst at the end of unloading is noticed from the above graph.

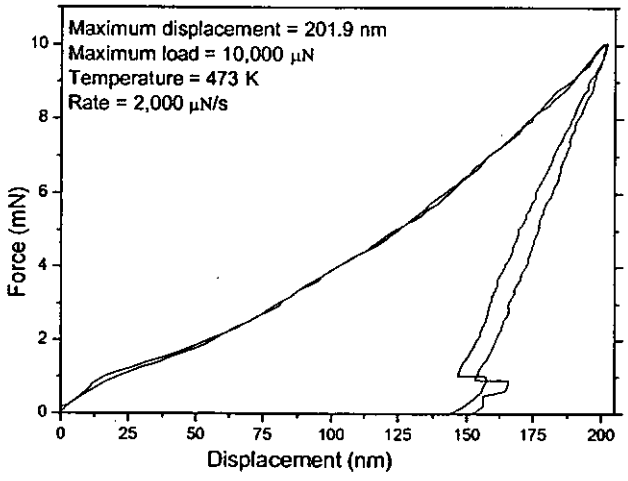

Figure 4.17. Graph showing the loading and unloading pattern at 473 K, 10,000μN, 2,000μN/s, The sudden burst at the end of unloading is noticed from the above graph.

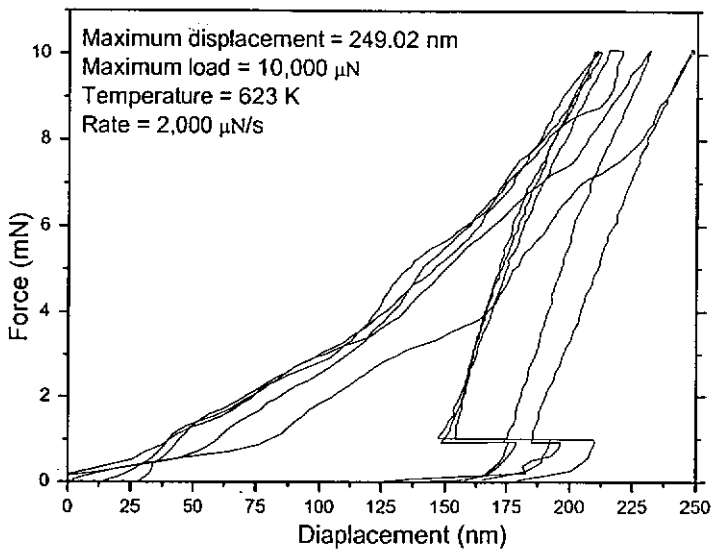

Figure 4.18. Graph showing the loading and unloading pattern at 623 K, 10,000μN, 2,000μN/s, The sudden burst at the end of unloading is noticed from the above graph.

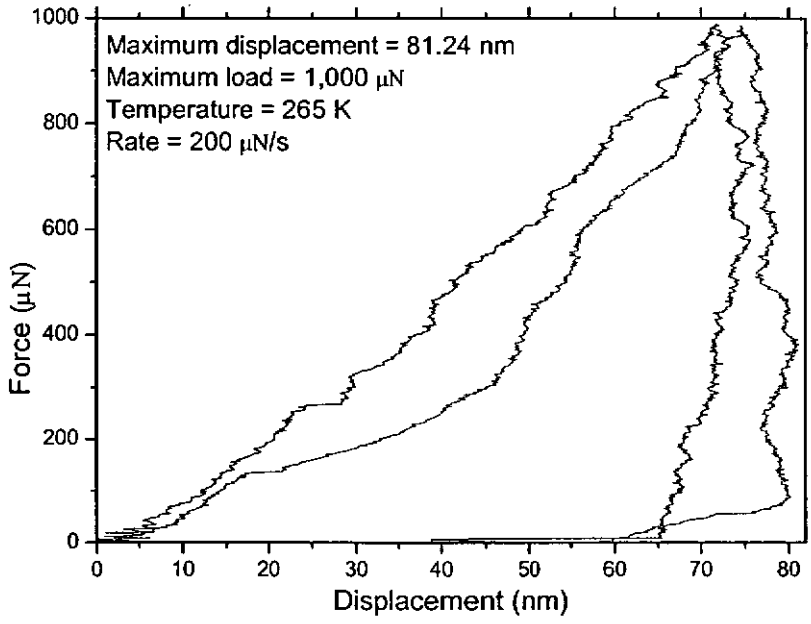

Figure 4.19. Showing the bursts

Table 4.5. Data at 1000 μN, 200 μN/s.

Temp/constants	h_{max},nm	$h_{plastic}$,nm	H,Gpa	E,Gpa
265 K	76.16	72.31	4.02	576.64
	81.24	77.83	3.55	6297.58
	52.48	49.38	7.53	9190.52

The data from the above table shows the effect of force and rate

Table 4.6. Comparison of data for different temperatures at 10,000 μN, 2,000 μN/s.

Temp/constants	h_{max}, nm	$h_{plastic}$, nm	H, Gpa	E, Gpa
373 K	190.62	154.24	12.22	202.16
	196.79	163.75	10.9	209.17
473 K	201.9	163.98	10.91	182.65
	201.29	149.86	12.69	144.8
623 K	249.02	191.92	8.28	105.82
	231.93	172.25	10.01	111.22
	211.49	141.71	14.09	112.84
	212.03	148.37	13.01	118.86
	231.93	172.25	10.01	111.22

Our experimental results show a closer modulus (Gpa) of 410 as also proved by Oliver et al [33] from their nanoindentation experiment on tungsten.

But our results show little difference, as it may be due to the higher temperature applied in our experiments. W (111) shows lower hardness values than W (110) as also evident from Al results from Micromaterials Company [19].

4.5 Results for Aluminum (100)

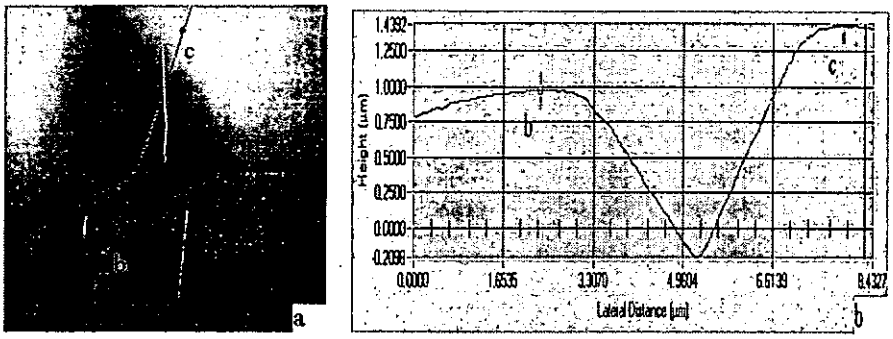

Figure 4.20. (a) 8µ size AFM image at 388 K, (b) Pile-up asymmetry

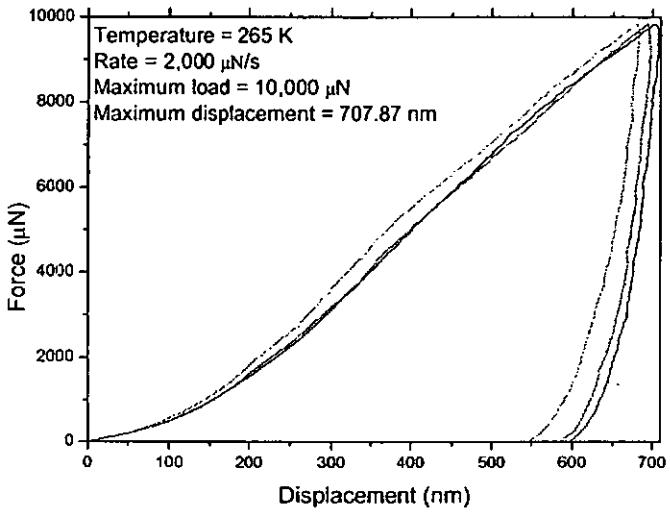

Figure 4.21. Graph showing the softening effect, loading and unloading pattern at 265 K, 10,000µN, 2,000µN/s.

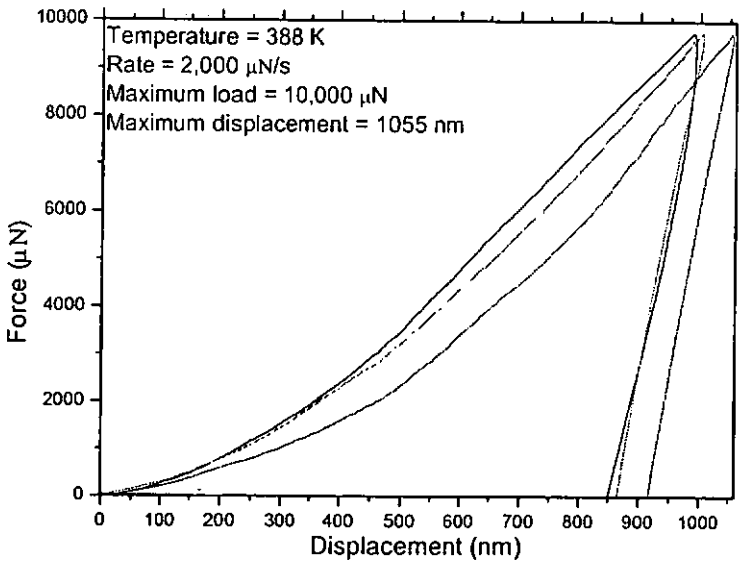

Figure 4.22. Graph showing the softening effect, loading and unloading pattern at 388 K, 10,000μN, 2,000μN/s.

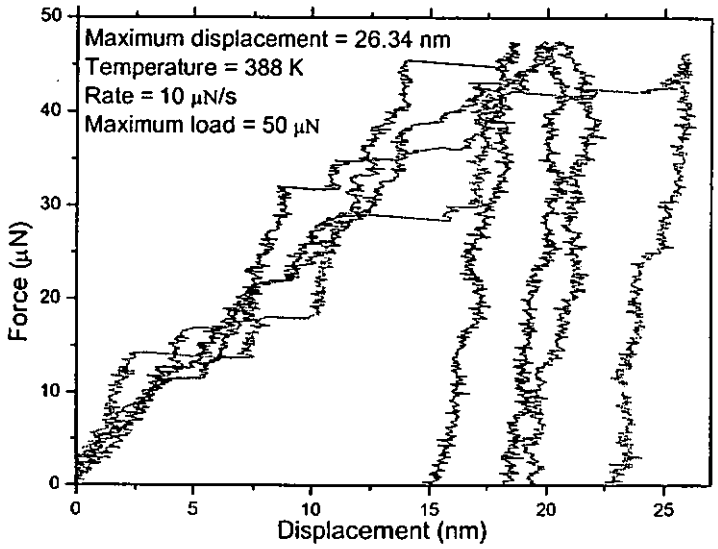

Figure 4.23. Shows initial burst. Maximum load is 50μN and rate is 10 μN/s at 388 K.

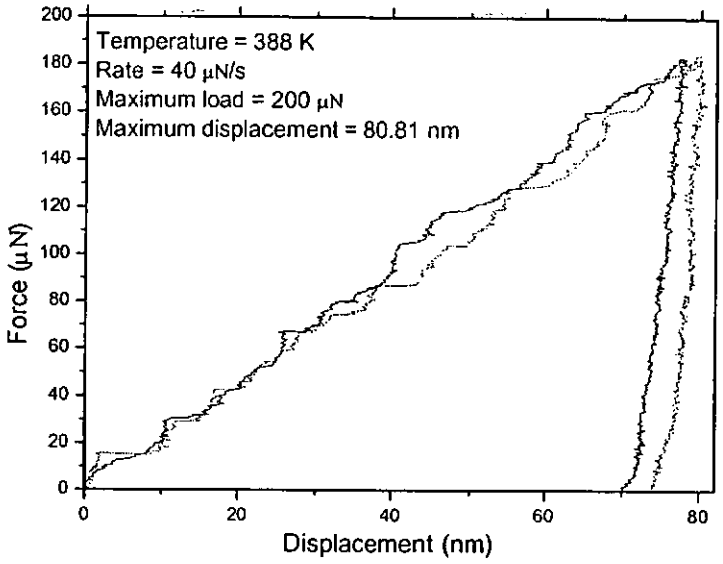

Figure 4.24. Shows initial burst. Maximum load is 200 and the rate is 40μN/s at 388K.

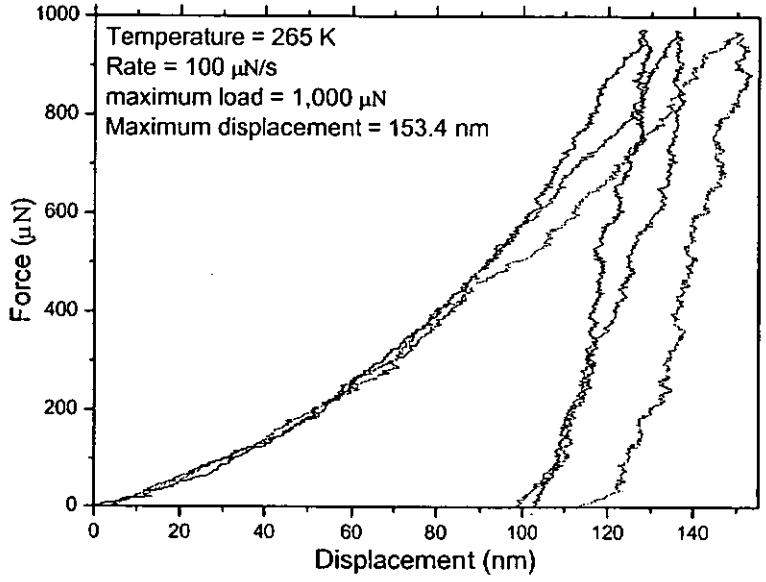

Figure 4.25. Shows burst. Maximum load is 1000μN and the rate is 100 μN/s at 265 K

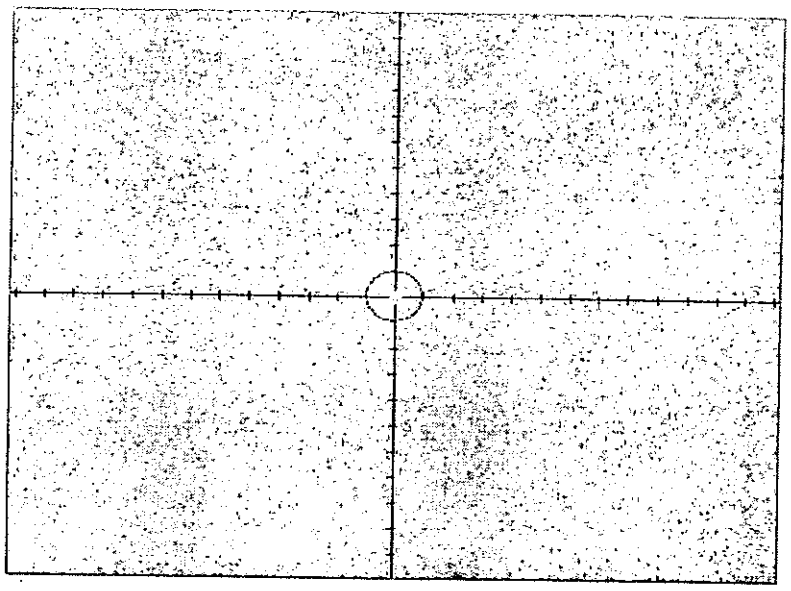

Figure 4.26. Shows the shear band formation around the indenter at 265 K. The ring formation reduces as the maximum load increases.

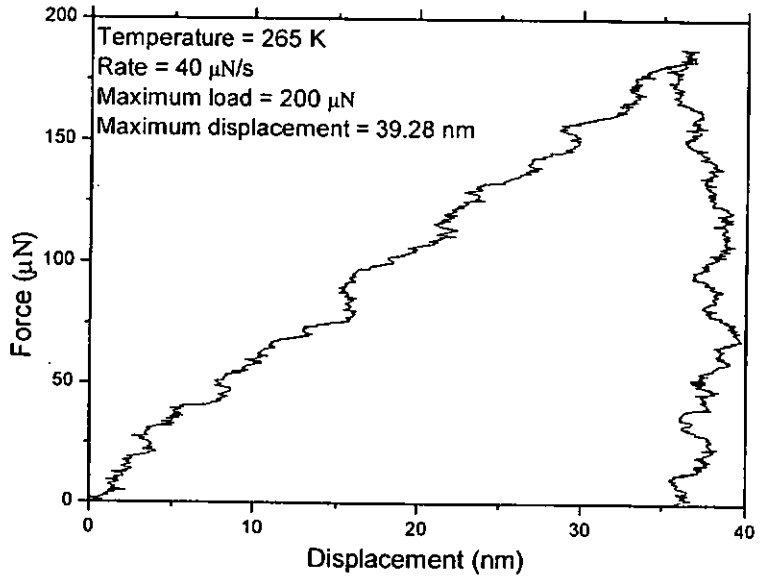

Figure 4.27. Shows loading and unloading curve at 265 K, 200 μN, 40 μN/s.

Table 4.7. Comparison of data for different temperatures at 200 μN, 40 μN/s.

Temp\constants	h_{max}, nm	H, Gpa	E, Gpa
265 K	68.34	1.3	631.48
	90.03	0.82	41.67
	79.94	0.96	25.65
388 K	128.2	0.26	273.9
	112.3	0.36	1194
	95	0.47	840.16

Table 4.8. Comparison of data for different temperatures at 10,000 μN, 2000 μN/s.

Temp\constants	h_{max}, nm	H, Gpa	E, Gpa
265 K	707.87	0.76	54.64
	668.26	0.87	93.92
	697.82	0.77	53.66
	683.13	0.83	43.1
388 K	992.3	0.42	16.5
	1054.9	0.4	12.1
	1004.2	0.44	12.8

At high temperature the hardness and modulus reduces due to softening, as it is also evident from the increase in the depth of indentation for the same

loading conditions. Pileup around an indentation is clearly observed. The recovery process shows that the energy is stored in the material after the plastic deformation. It seems that the load at which yielding occurs is independent of temperature between room temperature and 388 K as also evident from Bahr et al [2] results.

4.6 Results for Gold

4.6.1 Results for Au (111)

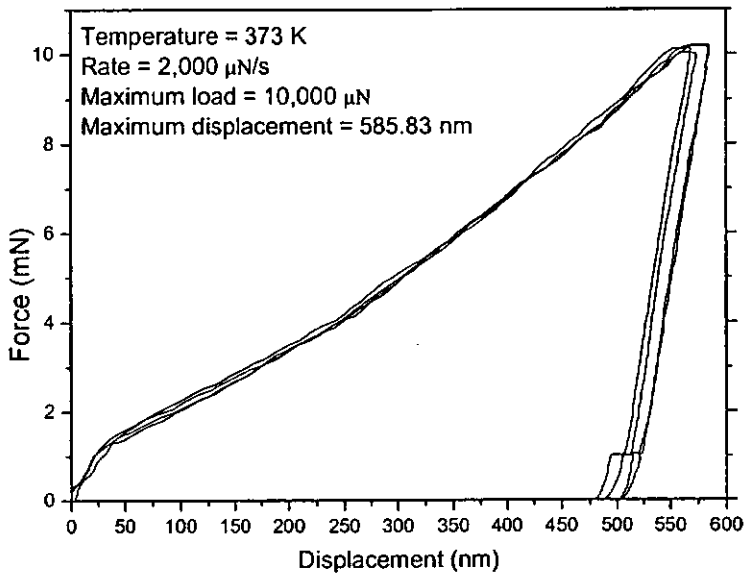

Figure 4.28. Graph showing the loading and unloading pattern at 373 K, 10,000μN, 2000μN/s, The sudden burst at the end of unloading is noticed from the above graph.

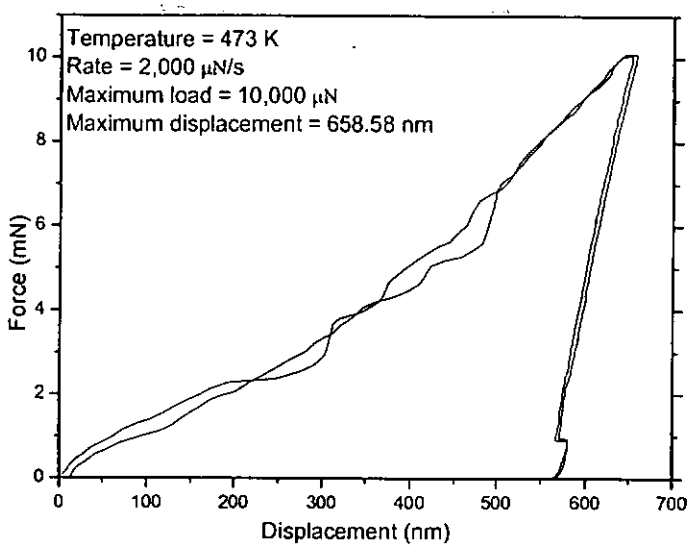

Figure 4.29. Graph showing the loading and unloading pattern at 473 K, 10,000μN, 2000μN/s, The sudden burst at the end of unloading is noticed from the above graph.

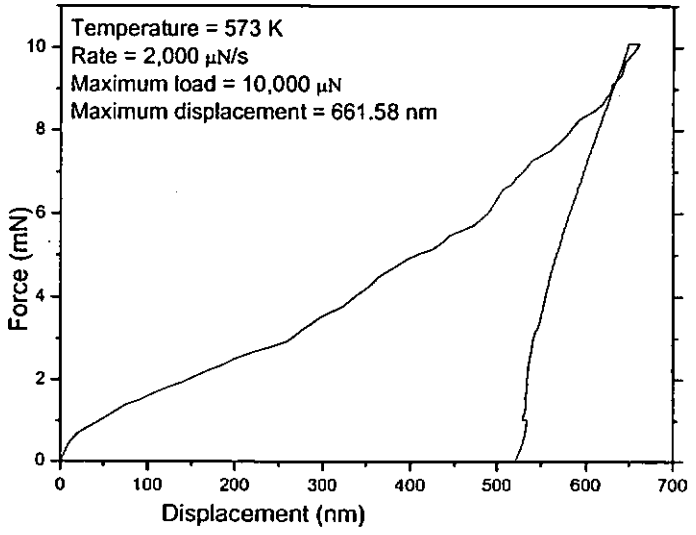

Figure 4.30. Graph showing the loading and unloading pattern at 573 K, 10,000μN, 2000μN/s, The sudden burst at the end of unloading is noticed from the above graph.

Table 4.9. Comparison of data for different temperatures at 10,000 μN, 2000 μN/s.

Temp/constants	h_{max}, nm	$h_{plastic}$, nm	H, Gpa	E, Gpa
373 K	584.13	528.22	1.28	42.58
	569.06	515.07	1.33	44.99
	573.94	518.42	1.31	43.14
	590.45	542.76	1.20	48.24
	585.83	535.73	1.25	47.03
473 K	653.18	569.14	1.1	26.10
	658.58	576.62	1.07	26.42
573 K	661.58	514.34	1.33	16.4

4.6.2 Results for Au(110)

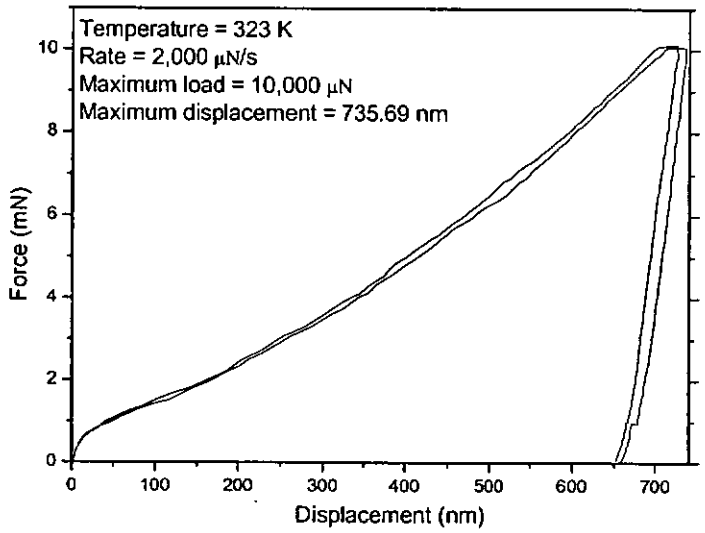

Figure 4.31. Graph showing the loading and unloading pattern at 323 K, 10,000μN, 2000μN/s, The sudden burst at the end of unloading is noticed from the above graph.

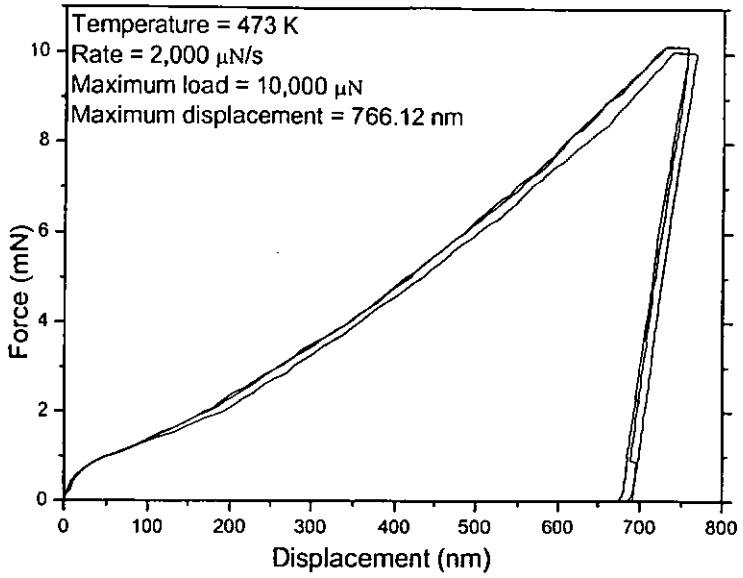

Figure 4.32. Graph showing the loading and unloading pattern at 373 K, 10,000μN, 2000μN/s, The sudden burst at the end of unloading is noticed from the above graph.

Table 4.10 Comparison of data for different temperatures at 10,000 μN, 2000 μN/s.

Temp/constants	h_{max}, nm	$h_{plastic}$, nm	H, Gpa	E, Gpa
323 K	726.41	675.28	0.79	36.57
	735.69	696.72	0.74	46.39
373 K	756.10	689.93	0.76	27.76
	755.55	693.22	0.76	29.46
	766.12	701.03	0.73	27.51

The elastic recovery of gold is small compared to other metals. It is clear from the penetration depths read from the curves that significant softening

occurred at the higher temperatures. Reductions in modulus also occurred. It is also interesting to note that at higher temperature, the curvature in the unloading curve has disappeared. This curvature is indicative of elastic recovery within the indentation itself.

4.7 Results Analyses and Discussions

Copper

The temperature dependency experiments show very interesting results. The complete effective elastic range is found. The onset of the first burst is measured. The onset of plastic deformation is noticed from the periodic bursts. The strain hardening effects, softening effects, strain release effects are noticed. The difference in pile up is also found for different temperatures. The new phenomena of material under the indenter, bouncing back at the end of unloading were clearly noticed. From the difference in depth for different temperatures, it is noticed that there is significant increase in depth at higher temperature. The hardness and elastic modulus also dropped at higher temperatures.

As shown in tables 4.1 and 4.2, as the temperature changes, the hardness and modulus changes significantly. At higher temperatures the hardness and modulus reduces due to softening, as it is also evident from the increase in the depth of indentation for the same loading conditions. Observation of material pileup around an indentation can be correlated to mechanical properties, such as yield stress. This recovery process shows that the energy is stored in the material

after the plastic deformation. It seems that the load at which yielding occurs is independent of temperature between room temperature and 388 K as also evident from Bahr et al [2] results. This supports the fact that the rate of nucleation may be altered, but the basic criteria to initiate a loop remain independent of temperature. The depth increases as the temperature increases. As evident from the experiment, the rate of indentation also affects the modulus and the hardness value of the material. The modulus is high when the difference between h_c , h_{eff}, h_{max} is high. But the hardness does not depend on this difference. The hardness is found to increase significantly as the indentation depth is reduced.

It is also noted that the elastic recovery is small as the temperatures goes up. As mentioned by Zimmerman et al [53], in both experimental and theoretical studies, the stacking fault energies show little dependence on temperature below 400 K. It is also noted that the elastic recovery reduces at higher temperatures. The defect generation and motion causes the plastic deformation, which is reflected in the pile up patterns. The pop-ins shown by the *p-h* curves corresponds to the formation of dislocations. The contact pressure (nanohardness) increases with decreasing indentation depth. A transition from elastic to fully plastic deformation was observed in the load range investigated.

From Figure 4.2, it is found that the clear pile up reduces at high temperature due to the global relaxation. Figure 4.3(a) shows the top view at 4000x2500 nm. A clearly visible striped pattern seen on the inside and outside of the surface of the indentation may be due the pressure on the adjacent vertical layers of material that causes this accumulation.

From table 4.2, for 265 K, 10,000 μN, 2000 μN/s., it is noticed that the difference between $h_{plastic}$ and h_{max} is 7 nm. But in case of 388 K, it is 30 nm. For 473 K, it is 37 nm. For 623 K, it is 40 nm. This phenomenon shows that the plasticity range increases, as the temperature increases, causing an increased failure of the material at high temperatures. In other words, the elastic recovery reduces at higher temperatures.

The hardness decreases and displacement increases as the temperature increases. From table 4.1 it is noted that the difference between $h_{plastic}$ and h_{max} at 388 K for 1000 μN, 200 μN/s, is less than that of 10,000 μN, 2,000 μN/s at 388K. It shows that the Loading rate also has effect on the range of plasticity. Also it is noted that the value of elastic modulus (E) high when the difference between $h_{plastic}$ and h_{max} and h_{eff} is high. The Hardness (H) does not depend on this difference. The value of Hardness (H) is found to decreases when the Displacement (h) is high, as noticed from the table, as also evident from the results of Roger smith et al [38].

During the indentation, the accumulated elastic energy in the indented region is partially released by the nucleation of dislocations. Upon retracting the indenter after the first yield, the pressure due to the compressive strain in the defect induces restoring forces that anneals the plastic deformation. Further indentation results in a second yield produced by the generation of dislocation loops.

Tungsten

Clear bursts are seen showing the nucleation of dislocations. A transition from elastic to fully plastic deformation was observed in the load range investigated. The pile up is clearly visible. The figure 4.19 for W (110) shows periodic bursts. It is noticed that the load displacement is not linear. At higher peak loads, the indentation contact in tungsten is not just elastic. Our experiment shows a modulus (Gpa) of 410, similar to that found by Oliver et al [33] from their nanoindentation experiment on tungsten. Our results show little difference. It may be due to the higher temperature applied in our experiments. Tungsten is chosen to illustrate this behaviour because of its isotropic elastic behaviour at low loads. W (111) shows lower hardness values than W(110).

There is no clear crack formation on the surface of the sample. The hardness values are very close to the previous experimental results of Oliver et al [33] on tungsten. We also notice that there is an elastic rebound at the end of loading, as the unloading curve starts at a depth less than the maximum depth.

Aluminium

The complete elastic range is found. The onset of the first burst is measured. The onset of plastic deformation is noticed from the periodic bursts. From the difference in depth for different temperatures, it is noticed that there is significant increase in depth at higher temperature. The hardness and elastic modulus also dropped at higher temperatures. The nanoindentation experiment

on Al single and polycrystals at room temperature by Gouldstone et al [17] also presents similar results for the initial burst as shown in our results.

As shown in tables 4.7 and 4.8, as the temperature changes, the hardness and modulus changes significantly. At high temperature the hardness and modulus reduction due to softening, as it is also evident from the increase in the depth of indentation for the same loading conditions. Pileup around an indentation is clearly observed. The recovery process shows that the energy is stored in the material after the plastic deformation. It seems that the load at which yielding occurs is independent of temperature between room temperature and 388 K as also evident from Bahr et al [2] results. The depth increases as the temperature increases. As evident from the experiment, the rate of indentation also affects the modulus and the hardness value of the material. The modulus is high when the difference between h_c , h_{eff}, h_{max} is high. But the hardness does not depend on this difference. The hardness is found to increase significantly as the indentation depth is reduced. A transition from elastic to fully plastic deformation was observed. Figure 4.25 shows the shear band formation around the indenter at 265 K. This ring formation reduces as the maximum load increases.

Gold

The elastic recovery of gold is small compared to other metals. This makes it an extreme case for modulus determination. It is clear from the penetration depths read from the curves that significant softening occurred at the higher temperatures. As shown in the table of results, reductions in modulus also

occurred. It is also interesting to note that at higher temperature, the curvature in the unloading curve has disappeared. This curvature is indicative of elastic recovery within the indentation itself. Finally, in all cases creep occurred at maximum load. The amount of creep, which is shown clearly by a gap between the loading and unloading curves, increases markedly with temperature. The amount of creep increased markedly with temperature. Indentations performed by the Micromaterials Company [19] at room temperature, 473 and 673 K using a Berkovitch indenter with maximum load of 50 mN and loading rate of 2.6 mN/s also show similar results. The hardness for (111) orientation is higher compared to (110) as it is also found for Al.

Jumps in the curves are observed at the end of unloading from higher loads. Possible causes may be the relocation of materials at the end of unloading, or phase transformation. Further investigation is needed to find out.

Significant noise in the loading and unloading curves is observed at lower temperatures. This can be avoided by suitable improvements in the testing system. The temperature of the sample stage is controlled to $< 0.002°$. Virtually zero added noise. These inconsistencies are usually exaggerated at lower loads. The noise floor of the TriboIndenter is less than 0.2nm in displacement and less than $0.1\mu N$ in force.

The pile up of material for different temperatures can be investigated further to find the transition temperature at which the pile up changes as the temperature changes. The AFM profile of the surface before the indentation is

required as a reference in order to compare the pile up profile after the indentation. The actual mechanism operating at the jump to the right and left in the unloading curve at higher loading is not completely understood as this is a new phenomenon. The noise in the loading and unloading curves at low temperature must be reduced by proper temperature control. Temperature control below room temperature can be improved by cooling to a lower level and then increase to the required temperature. An improved temperature control facility must be implemented in the testing system in order to maintain a steady temperature on the sample, to avoid expension and contraction due to temperature fluctuation. The testing environment should be perfectly sealed from the environment for the better temperature control.

The experiments for high-strength metals can be done at higher temperatures close to the recrystallization temperature with an experimental system that has a higher temperatures facility. The peak load and loading rate must be increased for high-strngth materials. The thermal drift problem at higher temperatures can be avoided by considering suitable techniques. A suitable system is necessary to be attached to the testing system to control ice formation on the sample during low temperature experiments. The small variations in the penetration depths in the *P-h* curves for same testing conditions must be avoided in case of single crystal.

Chapter 5 Computer Simulation Results

5.1 Introduction

Computer simulation helps with the understanding of the behaviour of the materials at the nanoscale, and to identify the controlling parameters in their behaviour. Normally the resistance of the material directly relates to the behaviour at the atomic level. There are many applications of nanoscale processing of materials. Our simulation aims to study the behaviour FCC structures in general. Both the behaviour of material during loading and unloading are analyzed to understand the recovery of the material during unloading. The results are compared for various temperatures. It helps to study the atomic rearrangements. The simulation on the copper (111) surface is performed and the various behaviour of the material was investigated. The simulation was performed under various temperatures on the substrate.

5.2 Methodology

The simulation of the copper (111) surface is performed and the various behaviours of the material were investigated. The simulation was performed at various temperatures with a spherical indenter. The interaction between the indenter and the substrate is modeled with a repulsive potential. For the substrate, Embedded Atom Method (EAM) is used to model the substrate. Periodic boundary conditions are applied for the substrate. The substrate is modeled with lateral dimensions of 14x16x7 nm. The maximum depth of the

indenter is 1.3 nm. The radius of the indenter is 3.12 nm. There are 192000 atoms in the substrate. The rate of indentation is 0.0013nm per time step. The velocity is 6.5 m/s. The cut off distance is 0.255 nm. The repulsive potential is used to model the interactions between the indenter and the substrate. Depending on the crystal orientation, the atoms near the surface are found to be disturbed to different degrees as the indenter approaches the material. Simulation is carried out at different temperatures: 0 K, 348 K, 475 K, 950 K. Max depth of indentation is 1.3 nm, 1.87nm.

5.3 Results

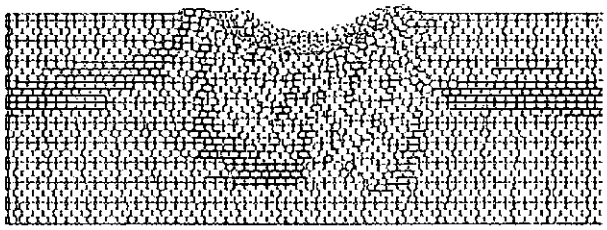

Figure 5.1. The hillocks due to pile up.

Figure 5.1, which is at 0 K, shows the pile up of the material above the surface of the substrate. The pile up on the surface around the indenter is due to the release of compression beneath the indenter due to the conservation of volume during micro plastic deformation (bursts). The rotation of the lattice during nanoindentation also accounts for the pile up. The first burst occurs when

the maximum shear stress at the tip of the indenter reaches the theoretical shear strength.

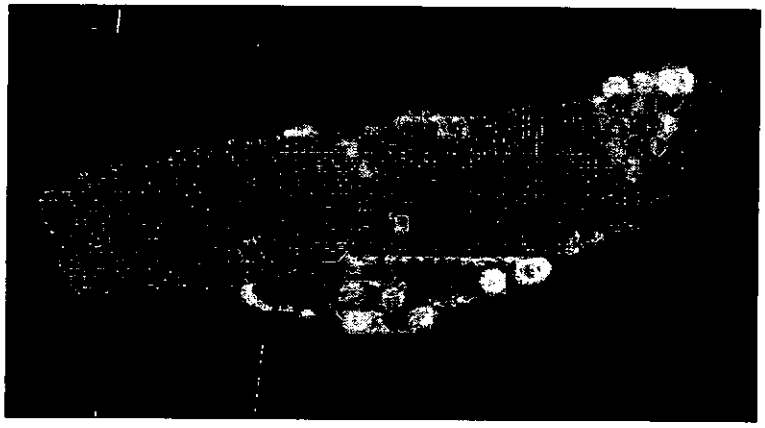

Figure 5.2. The pile up of atoms at h=0.985nm.

Figure 5.2, shows the part of the substrate around the indenter. The red colour shows the pile of atoms. Also, an isolated hillock away from the indenter is found.

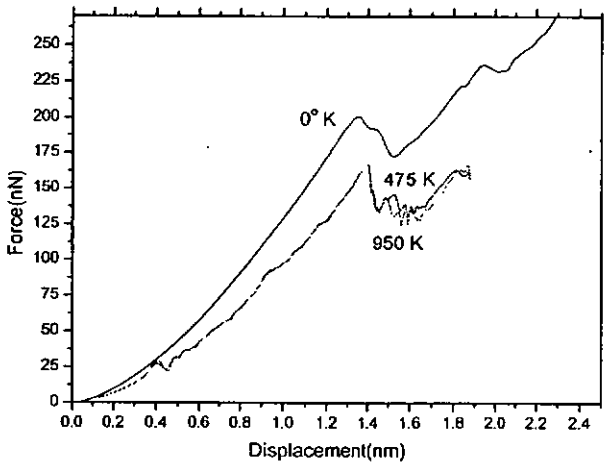

Figure 5.3. Loading pattern and softening effect at different temperatures.

From figure 5.3, the graph at higher temperatures shows the phenomenon of load drop at smaller penetration depth, illustrating that this happens even without oxide layer on the surface as also proved by Gerberich et al [16]. The load drop occurs at smaller penetration depth at higher temperatures. But this phenomenon is not noticed at 0 K. It is evident from figure 5.3 that the *P-h* curve for 450 K and 950 K is overlapping showing that there is not much effect above a critical value. This overlapping in curve occurs after approximately 348 K. Also the curves at higher temperatures shows that there is a load drop at smaller penetration depth. This may be caused by the pile up of atoms around the indenter. Beyond 348 K, the curves for 475 K and 950 K overlap. The microstructure shown in figures 5.6 and 5.8 at 475 K and 950 K also shows the similar deformation.

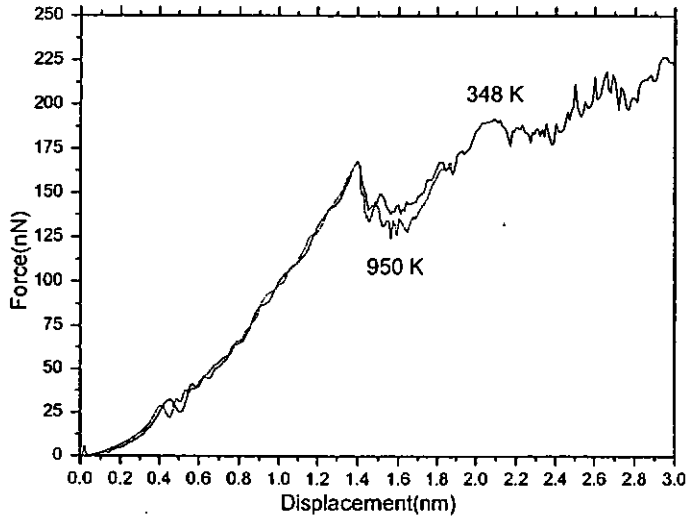

Figure 5.4. Loading pattern at 348 K and 950 K.

From figure 5.4, large fluctuations in the curves are noticed at 348 K. The phenomenon of load drop at higher temperatures at smaller penetration

depth is also noticed at 348 K. The curves also show the softening effect at higher temperatures.

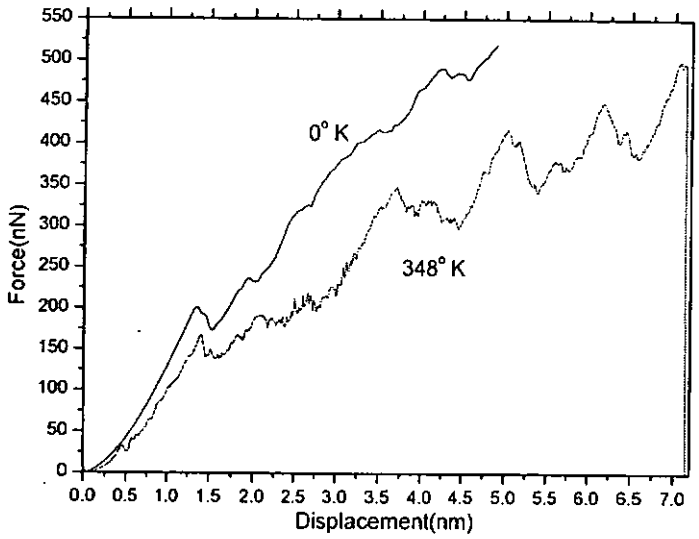

Figure 5.5. Loading pattern at 0 K and 348 K.

As shown in figure 5.5, the loading curve at 0 K and 348 K shows the softening effect. The softening effect is also noticed from nanoindentation experiments at various temperatures. Large drop in load is noticed at the same penetration depth. It seems that the temperature does not affect the point of plastic deformation. But the curve at 348 K shows that there is a small drop in load at a smaller penetration depth, indicating that there is some dislocation even at smaller penetration depth.

475 K, h=0.25nm 950 K, h=0.25nm

Figure 5.6. Illustrating load drop at smaller penetration depth.

A small load drop in the *P-h* curve noticed at these temperatures corresponds to the displacement of atoms as shown in figure 5.6. But there are no displaced atoms at 0 K, which is evident from the smooth curve as shown in figure 5.3. After 348 K, the curves are overlapping for 475 K and 950 K as seen from figure 5.3. Figure 5.8 also shows similar deformation structure at these temperatures, illustrating the overlapping nature form *P-h* curves.

0 K 348 K 475 K

Figure 5.7. Microstructure at h=0.39nm.

Figure 5.7 and 5.8 shows that the microstructure at a penetration depth of h=0.39nm. Microstructure 475 K is similar to that of 950 K at h=0.5 nm, showing elastic behaviour.

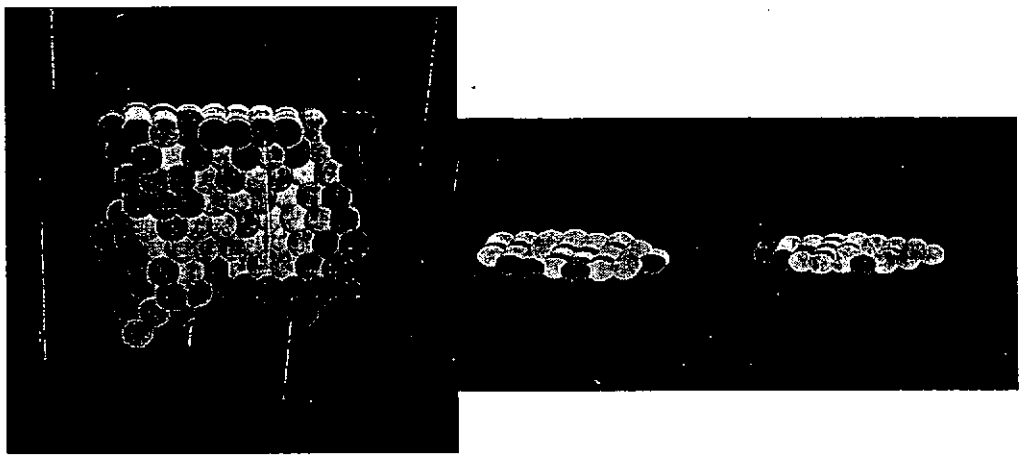

0 K, h=0.41nm 475 K, h=0.5nm 950 K, h=0.5nm

Figure 5.8. Microstructure at different temperatures.

After 348 K, the curves are overlapping for 475 K and 950 K as seen from figure 5.3. Figure 5.8 also shows similar deformation structure at these temperatures, illustrating the overlapping nature form *P-h* curves. Structure offers resistance for large dislocation even before *h*=0.5nm for 475 K and 950 K. But for 0 K displacement is found even at *h*=0.41nm. The structure for 475 K and 950 K looks similar as also evident from the graph. The graph also shows that graph around 450 K closely follows 950 K proving that there is no effect of temperature after a critical value. As mentioned by Zimmerman et al [53] both in experimental and theoretical studies, the stacking fault energies show little dependence on temperature below 400 K. It is found from figure 5.3 that *P-h* curve for 450 K and 950 K is overlapping showing the similarity in the deforming nature of microstructure after a certain critical temperature.

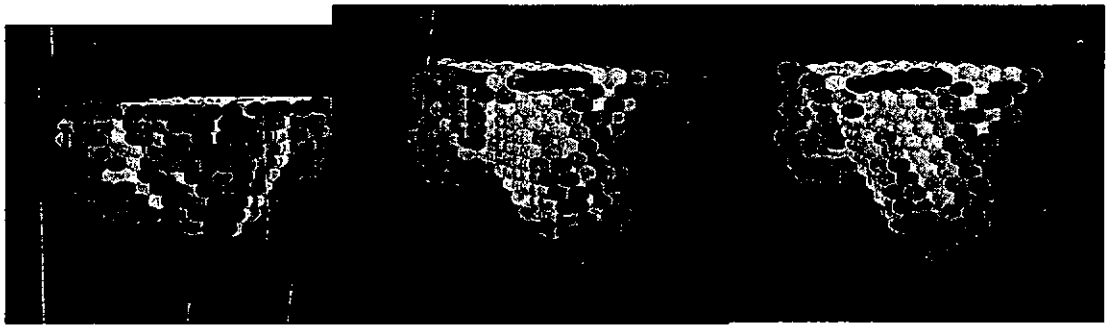

0 K, *h*=0.54nm. 475 K, *h*=0.51nm. 950 K, *h*=0.51nm

Figure 5.9. Microstructure at different temperatures.

Figure 5.9, shows that the microstructure at 475 and 950 K is similar, illustrating that the deformation of structure is not affected by temperature until a certain critical temperature and until a certain critical penetration depth only. This is also proved from the *P-h* curves as shown in figure 5.3. But after this critical depth, the deformation pattern is not similar as shown in figure 5.10.

From figure 5.9, at 0 K, even at h=0.54nm, no large deformation is found. Only the region under indenter becomes amorphous. At the higher temperature simulations, clear sign of dislocations are noticed. At penetration larger than h=0.5 nm, at higher temperatures, there is sudden and clear deformation. But from figure 5.8 at h=0.5 nm, no dislocations are seen at 475 K and 950 K.

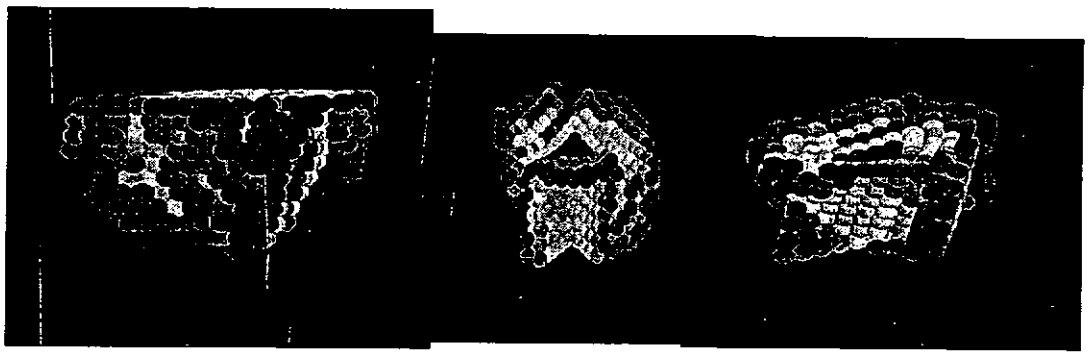

0 K, h=0.54nm. 475 K, h=0.54nm. 950 K, h=0.54nm

Figure 5.10. Microstructure at different temperatures.

Also the figure 5.10, at 0 K, even at h=0.54nm, no large deformation is found. Only the region under indenter becomes amorphous. At the higher temperature simulations, clear sign of dislocations are noticed. At penetration larger than h=0.5 nm, at higher temperatures, there is sudden and clear deformation. But from previous figure at h=0.5 nm, no dislocations are seen at 475 K and 950 K. Here we notice that the similarity in deformation at 475 and 950 K is not seen, illustrating that this phenomenon occurs only up to certain penetration depth.

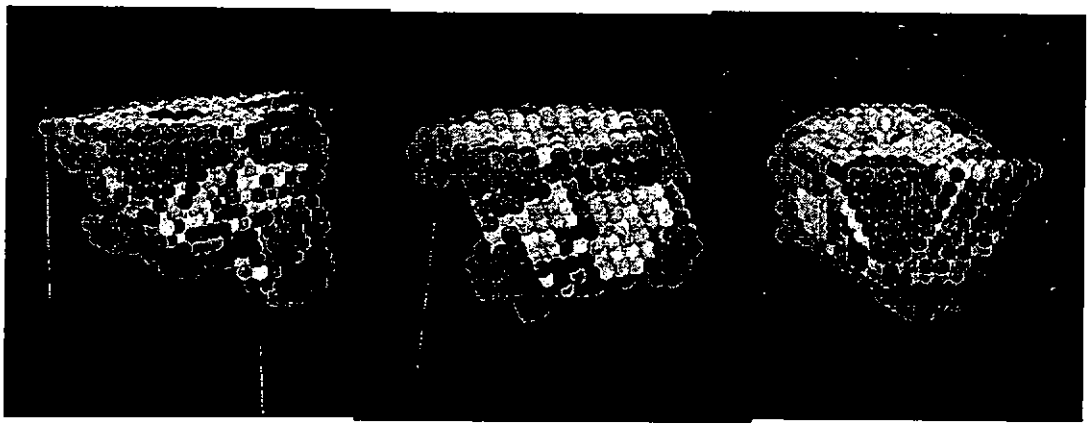

0 K, h=0.78nm 475 K, h=0.78nm 950 K, h=0.78nm

Figure 5.11. Microstructure at different temperatures.

From figure 5.11 at higher temperatures, initially the dislocation develops in one of the [110]/(111) directions, and changes to other slip system as compared to the figure 5.10. But for 0 K, dislocation develops in a particular [110]/(111) gradually.

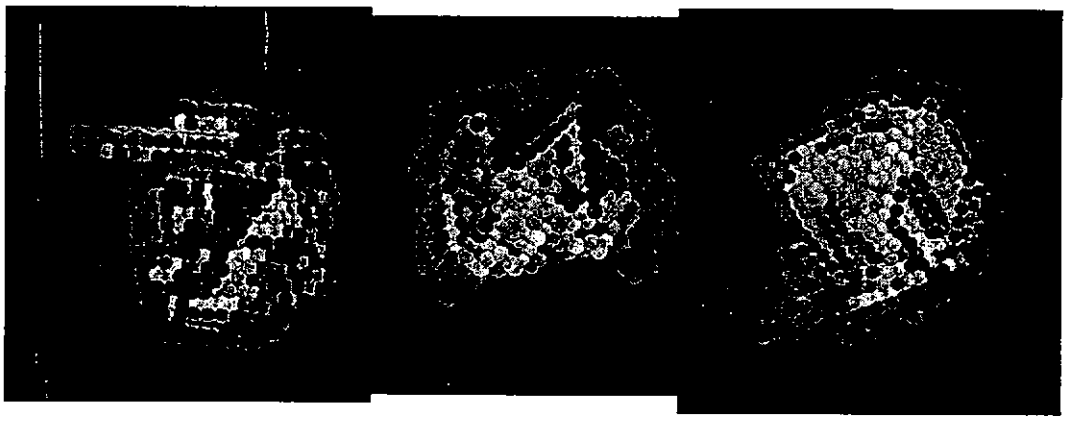

0 K, h=0.78nm 475 K, h=0.78nm 950 K, h=0.78nm

Figure 5.12. Microstructure in bottom view.

Figure 5.12 is the bottom view of the microstructure shown in figure 5.11 at the same penetration depth of h=0.78 nm. This clearly shows the

microstructure deformation beneath the indenter. It is found that the varying nature of shear deformation in different directions for different temperatures.

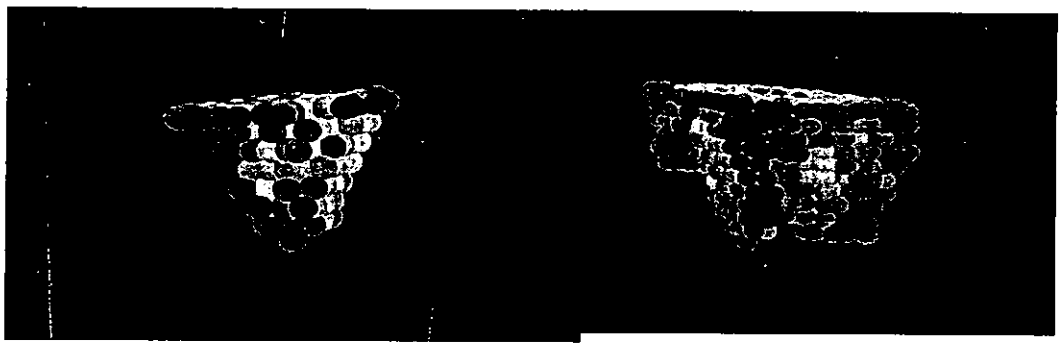

h=0.41nm *h*=0.54nm

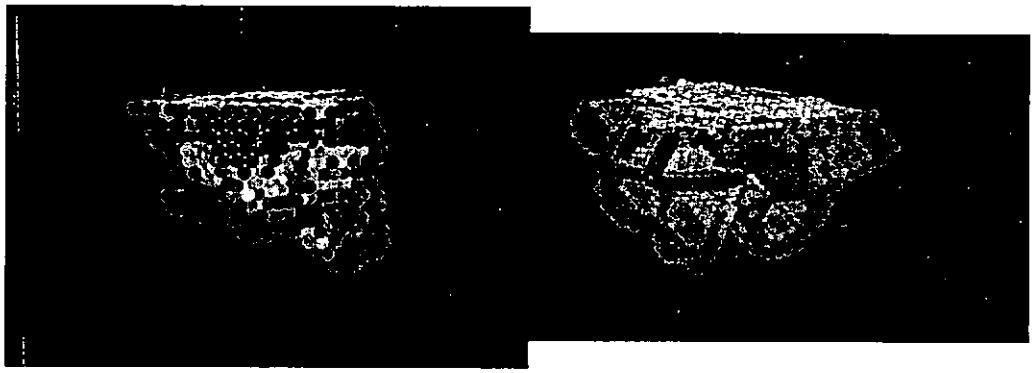

h=0.78nm *h*=1.3nm

Figure 5.13. Dislocation Mechanism at 0 K during loading.

The microstructure at various penetration depths as shown in figure 5.13, reveals the different stages of deformation. It is found that the deformation is higher as the depth increases.

h=1.29nm *h*=1.27nm

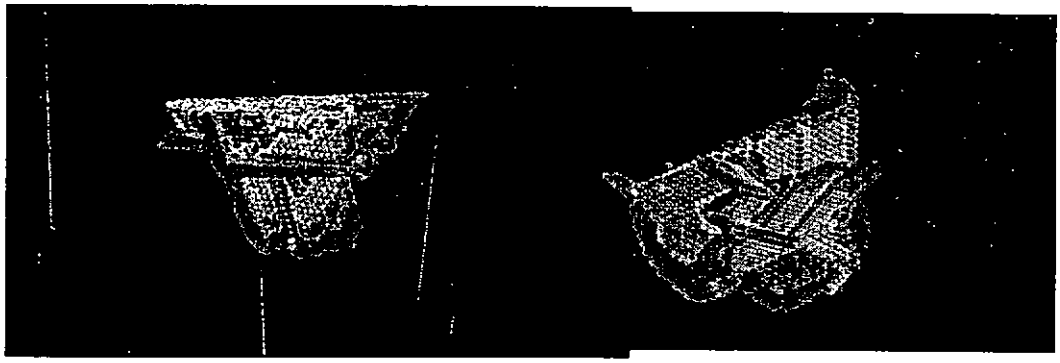

h=1.12nm *h*=1.12 nm(bottom)

Figure 5.14. Dislocation mechanism at 0 K during unloading

The microstructure in figure 5.14 clearly shows the deformation of the structure at larger penetration depths during unloading. The side view of the microstructure at *h*=1.29 nm and 1.27 nm, shows some form of rearrangement as the indenter retracts. But when the indenter retracts to *h*=1.12 nm, we notice the shear deformation of the structure in other directions. This may be due to the release of energy under the indenter, causing the material to deform in other directions. Figure 5.14 also shows the bottom view of microstructure at *h*= 1.12 nm. It clearly shows the shear deformation.

h=1.29nm *h*=1.29nm

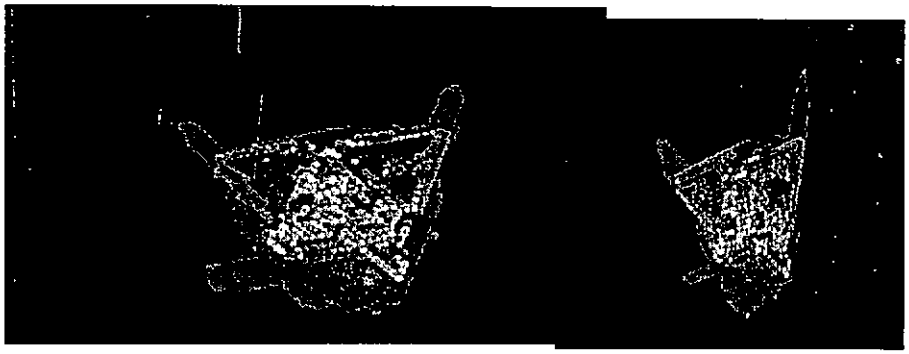

h=1.12nm(bottom) *h*=0.0013nm(bottom)

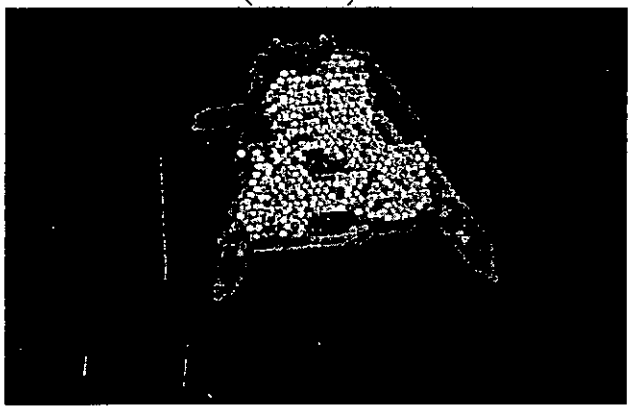

h=0.0013nm

Figure 5.15. Microstructure at 0 K during unloading.

From figure 5.15 at 0 K it is noticed that during unloading, the dislocation in other [110]/(11$\bar{1}$) systems grows further simultaneously, but, dislocation in one of the other [110]/ (111) system reduces. At *h*=1.3nm, dislocation in <110>{111} grows simultaneously. The bottom and top view of microstructure at *h*= 0.0013 nm is almost at the end of unloading. We found larger number of dislocation movements that is not recovered. This shows the plastic deformation nature of the structure at the end of unloading.

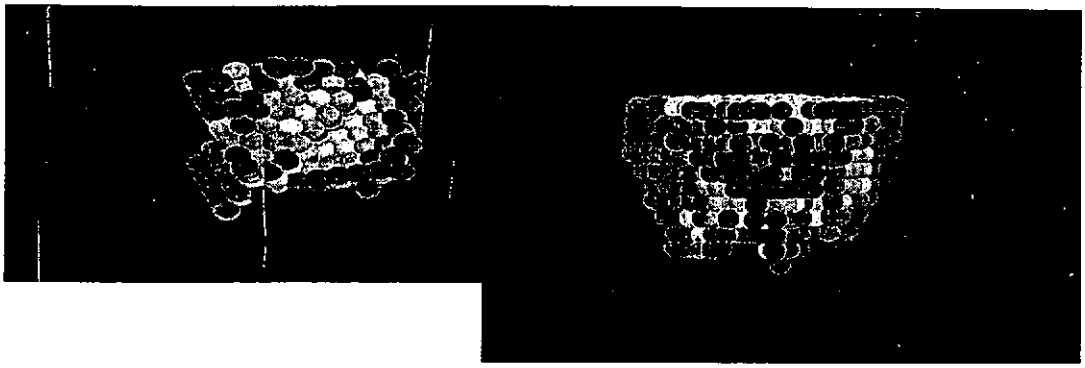

h=0.41nm *h*=0.54nm

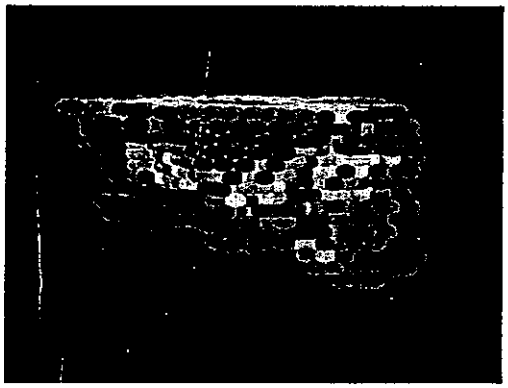

h=0.78nm

Figure 5.16. Dislocation behaviour at 0 K

Figure 5.16 at different penetration depths is shown to illustrate the nature of deformation during the loading at 0 K. It shows the different stages of deformation. Initially the area under the indenter looks amorphous without a clear direction of deformation. The embrittlement behaviour at 0 K may be the reason. This is also found in the nanoindentation experiments at 265 K. At *h*=0.78 nm, clear shear deformation is found in a particular direction.

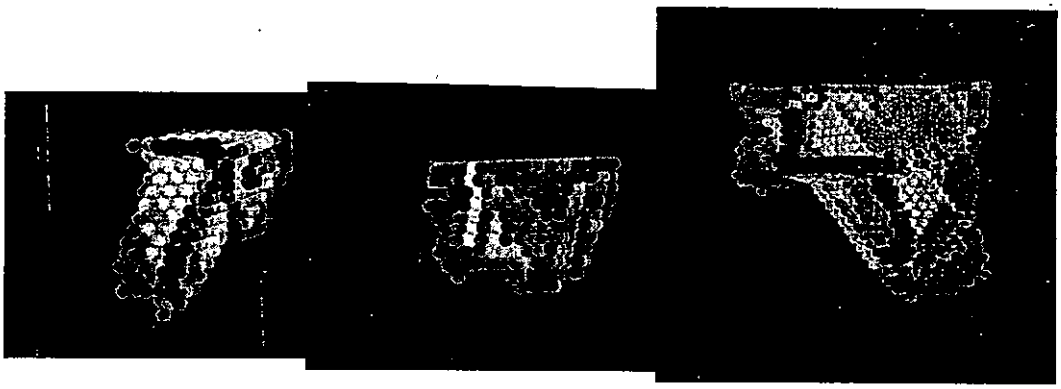

h=0.41nm *h*=0.54nm *h*=0.78nm

Figure 5.17. Dislocation behaviour at 348 K

Figure 5.17 at different penetration depths is shown to illustrate the nature of deformation during the loading at 348 K. we found that microstructure at *h*=0.41 nm shows clear and large deformation in a particular direction as compared to 0 K, which is amorphous. It shows that the structure relaxes globally in a particular direction without offering much resistance.

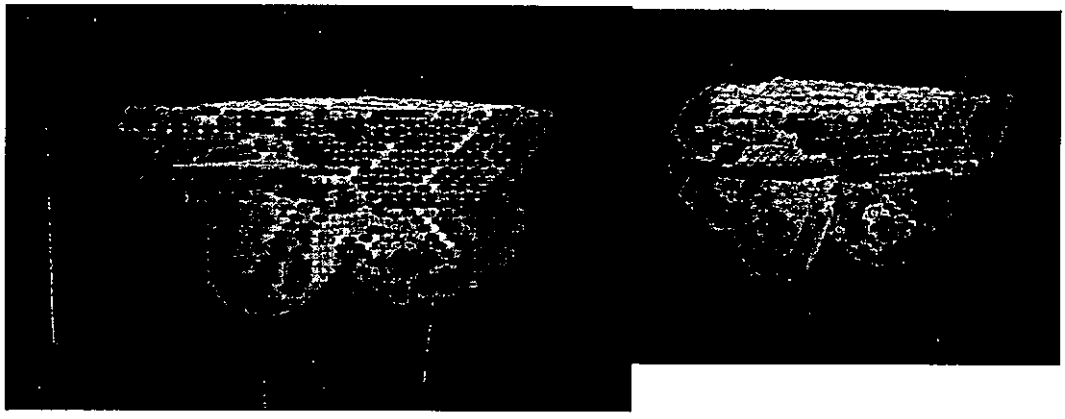

h=1.14nm *h*=1.2nm

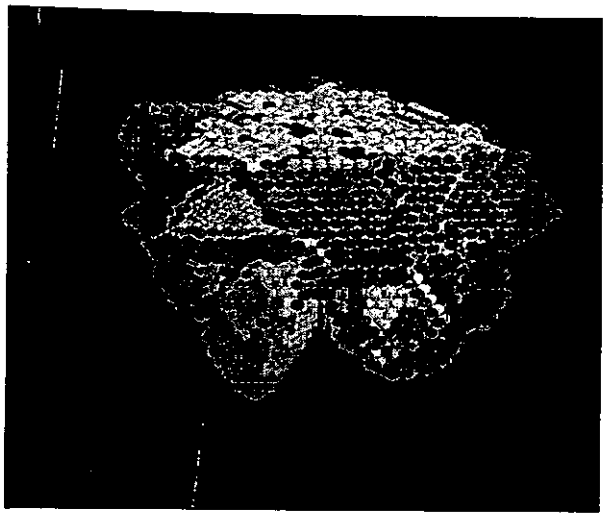

h=1.3nm

Figure 5.18. Dislocation behaviour at 0 K at higher depth.

Figure 5.18 at larger penetration depths is shown to illustrate the nature of deformation during the loading at 0 K. As the penetration depth is large, the microstructure exhibits clear and large deformation in a particular direction as compared to smaller penetration depth as shown in figure 5.13, which is amorphous. But these deformations tend to be plastic as seen in figure 5.15.

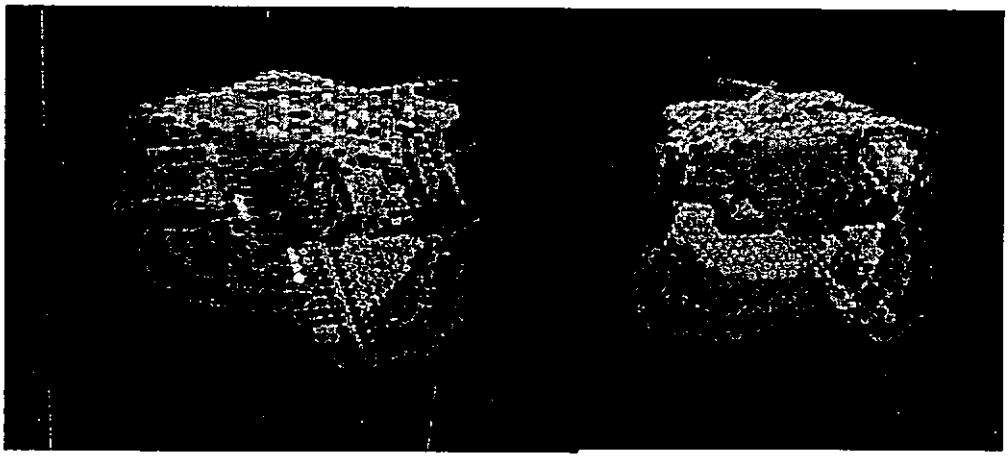

h=1.14nm *h*=1.2nm

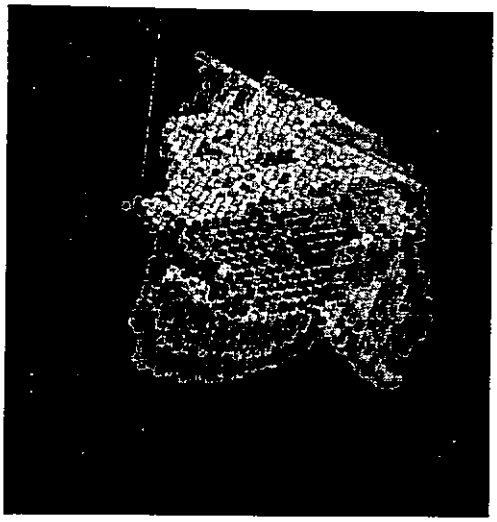

h=1.3nm

Figure 5.19.Dislocation behaviour at 348 K at higher depth.

From figure 5.19 at *h*=1.1nm, the dislocation is large in both 348 K and 475 K, but not at 0 K. But from figure 5.11 at higher temperatures, initially the dislocation develops in one of the [110]/(111) directions, and changes to other slip system as compared to the figure 5.10. But for 0 K, dislocation develops in a particular [110]/(111) gradually. From figure 5.15 at 0 K, it is noticed that during unloading, the dislocation in other [110]/(111) systems grows further simultaneously, but, dislocation in one of the other [110]/ (111) system reduces. At *h*=1.3nm, dislocation in <110>{111} grows simultaneously.

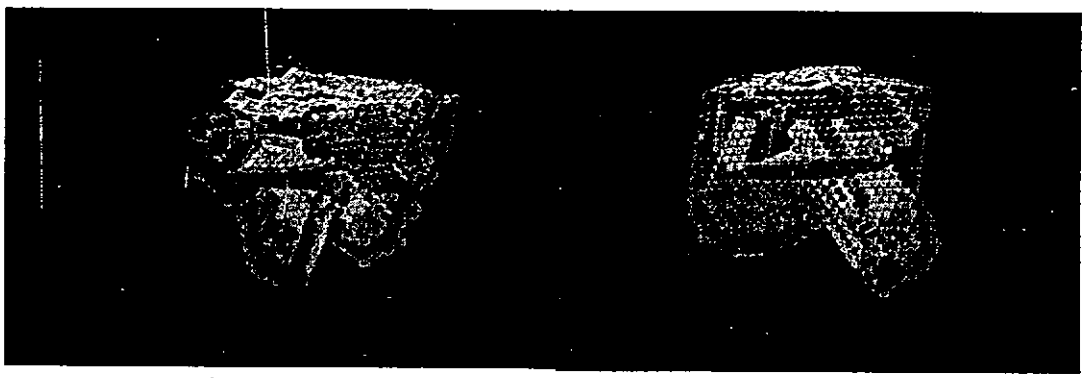

h=1.14nm, 0 K *h*=0.985nm, 348 K

Figure 5.20. Maximum dislocation with out considering the substrate effect.

Figure 5.20 is shown to illustrate the deformation at a larger penetration depth and to compare the microstructure at 0 K and 348 K. The shear deformation at these penetration depths must be plastic. As the depth is small compared to the thickness of the substrate, effect of the reaction force from the substrate may be neglected.

Bottom view

Figure 5.21. Dislocations at h=2.05nm and 348 K.

Figure 5.21 shows the deformation of the substrate at h=2.05nm and 348 K. As the penetration depth is larger, it is appropriate to considering the substrate effect. The substrate may offer reaction force at the bottom. The reaction force may also affect the deformation of the microstructure. The figure 5.21 shows the top and the bottom view. From the cross section of the bottom view, it is found that, there are isolated displacements away from the indentation area. This may also be related to the hillocks noticed in figure 5.2.

5.4 Results Analyses and Discussions

Computer simulations reveal the behavior of the materials at the nanoscale at different temperatures. Normally the resistance of the material directly relates to the behaviour at the atomistic level. The simulation results of copper represents the general behaviour of FCC structures in general. Both the behaviour of material during and unloading are analyzed to understand the reconstruction of the material during the removal of load. The results are compared with various temperatures. The atomic rearrangements are studied after the indentation at various temperatures.

Colour coding

The computer simulation results show the deformed crystal structure under and around the indentation. The differently colored atoms have crystal environments that are different from that of the regular lattice, as measured by the slip vector. The color represents the magnitude of the slip vector. A red color shows the maximum value and the blue color represents the minimum value. The black colored area in simulation figures represent the atoms that are relatively undisplaced with respect to the perfect crystal lattice, i.e., with a slip vector whose magnitude is below minimum, and is not shown. Only atoms above the minimum slip magnitudes are shown. The slip vector is given by, $s^{\alpha} = -\frac{1}{n_s}\sum_{\beta \neq \alpha}^{n} (x^{\alpha\beta} - X^{\alpha\beta})$, where x and X are the vectors linking the atom α with all its nearest neighbors β in the current and reference positions, n_s is the number of slipped neighbors, and n is the number of nearest neighbors to atom α. Reference position is the arrangement of atomic positions associated with the

zero mechanical stress. The atom in blue color along the edges of the deformed structure represent the dislocation moving on the slip plane shown by two layers of atoms causing the shear deformation called the stacking fault. In case of low temperature, we cannot notice a clear dislocation. The structure at higher temperatures clearly shows the dislocation.

From figure 5.15 at 0 K it is noticed that during unloading, the dislocation in other [110]/(111) systems grows further simultaneously, but, dislocation in one of the other [110]/ (111) system reduces. At h=1.3nm, dislocation in <110>{111} grows simultaneously. From figure 5.19 at h=1.1nm, the dislocation is large in both 348 K and 475 K, but not at 0 K.

Both plastic deformation and the work hardening effects are indicated. The microstructure analysis for the substrate at temperature 0 K shows that hillock forms near the indentation above the surface of the substrate. The formation of the hillocks may be due to the conservation of volume, release of compression beneath the indenter, conservation of volume in the thin film during micro plastic deformation (bursts) and rotation of the lattice during nanoindentation.

From the *P-h* curves as shown in figures 5.4 and 5.5, it is noticed that periodic load drops are observed. The bursts are caused by stress relaxation under the indenter due to the nucleation and glide of dislocations. The displacement regions are discontinuous and away from the indenter area. The displacements also propagate to the lower surface. We also notice the isolated

displacements away from the indentation. This may be due to the reaction force at the bottom of the substrate. The structure around the indenter becomes amorphous.

The *P-h* curves in simulation shows significant noise due to temperature effects. Shows multiple discrete reductions in load that can be directly related to a discrete dislocation activity involving dislocation nucleation or reorganization of the existing dislocation structures. The atomic activities such as shuffling and stress-assisted free volume migration are aided by temperature.

The partial dislocation reactions lead to a number of dislocation lock structures. Exhibits several surface parallel stacking fault planes just below the sample surface. Initial slip led to a wedge shaped dislocation loop structure. The initial slip structure consists of partial dislocations.

The computer simulation can be extended to include other metals for a better interpretation of results. The force drop in the loading curve at a smaller penetration depth at higher temperatures can be analyzed further by following the structure changes at this location to identify the various reasons causing this phenomenon. The analyses at higher temperatures for hard metals can be performed, as experimental investigation at very high temperatures is not possible, as these facilities are not available at present.

Chapter 6 Conclusions and Suggestions for Future Research

6.1 Conclusions

The temperature dependency experiments show very interesting results. The experimental results of different metals at different temperatures represents the general behaviour of FCC and BCC structures in general. Both the behaviour of material during loading and unloading are analyzed to understand the recovery of the material during unloading. The results for different temperatures are compared.

Our experiments clearly show the onset of the first strain burst, the onset of plastic deformation in connection with the periodic bursts, and the strain hardening/softening/release effects. The hardness and elastic modulus are smaller at higher temperatures. This softening phenomenon corresponds to the increase of indentation depth for the same loading conditions. The elastic recovery reduces at higher temperatures. The pop-ins shown by the *p-h* curves correspond to the formation of dislocations. The contact pressure (nanohardness) increases with decreasing indentation depth. We attribute the temperature dependence to the increased dislocation mobility and the reduced dislocation density as the temperature increases. Pileup around an indentation is clearly observed.

The onset of the first burst is measured. The onset of plastic deformation is identified from the periodic bursts. The difference in pile up is also found for different temperatures. The new phenomena of material under the indenter, bouncing back at the end of unloading were clearly noticed. From the difference in depth for different temperatures, it is found that there is significant increase in depth at higher temperature. The hardness and elastic modulus also dropped at higher temperatures. The rate of indentation also affects the modulus and the hardness value of the material. The hardness is found to increase significantly as the indentation depth is reduced. It is noted that the plastic deformation is higher at higher temperatures. Our experiment shows a modulus (Gpa) of 410, similar to that found by Oliver et al [33] from their nanoindentation experiment on tungsten. Our results show little difference. It may be due to the higher temperature applied in our experiments. W (111) shows higher hardness values than W (110) as also evident from Al results from Micromaterials Company [19].

In case of aluminum, the onset of the first burst is measured. The onset of plastic deformation is noticed from the periodic bursts. There is significant increase in depth at higher temperature. At higher temperatures the hardness and modulus reduces due to softening. Pileup around an indentation is clearly observed. It seems that the load at which yielding occurs is independent of temperature between room temperature and 388 K as also evident from Bahr et al [2] results. The hardness is found to increase significantly as the indentation depth is reduced. The transition from elastic to fully plastic deformation was observed. Figure 4.26 shows the shear band formation around the indenter at 265 K. This ring formation reduces as the maximum load increases.

The elastic recovery of gold is small compared to other metals. Significant softening occurred at the higher temperatures. It is also interesting to note that at higher temperature, the curvature in the unloading curve has disappeared. This curvature is indicative of elastic recovery within the indentation itself. The hardness for (111) orientation is higher compared to (110). Gold is found to regain all plasticity. Generally, in case of all metals, the hardness of (111) orientation is higher than (110). There is ring formation.

Computer simulations results show that the curves at higher temperatures shows that there is a load drop at smaller penetration depth. This may be caused by the pile up of atoms around the indenter. But this phenomenon is not noticed at 0 K. It is evident from figure 5.3 that the *P-h* curve for 450 K and 950 K is overlapping showing that there is not much effect above a critical value. This overlapping in curve occurs after approximately 348 K. The microstructure shown in figures 5.6 and 5.8 at 475 K and 950 K also shows the similar deformation. The *P-h* curves in simulation shows significant noise due to temperature effects. Shows multiple discrete reductions in load that can be directly related to a discrete dislocation activity involving dislocation nucleation or reorganization of the existing dislocation structures.

The partial dislocation reactions lead to a number of dislocation lock structures. Exhibits several surface parallel stacking fault planes just below the sample surface. Initial slip led to a wedge shaped dislocation loop structure. The initial slip structure consists of partial dislocations. Both plastic deformation and

the work hardening effects are indicated. Pile up of atoms is found around the indented surface. The *P-h* curves show periodic load drops. The bursts are caused by stress relaxation under the indenter due to the nucleation and glide of dislocations. The displacement regions are discontinuous and away from the indenter area. The displacements also propagate to the lower surface. We also notice the isolated displacements away from the indentation. This may be due to the reaction force at the bottom of the substrate. The structure around the indenter becomes amorphous. It is clear from the penetration depths that significant softening occurred at high temperatures. Temperature effects on the material are softening of the substrate. At low temperature, structure withstands higher load, the ductile behaviour at higher temperature.

6.2 Suggestions for Future Research

1. Theoretical models can be established for the relationship between the temperature and mechanical properties of metals helping in design and selecting suitable materials for real-life environments depending on the thermal loading.
2. Thermal loading can be increased to higher values for hard metals.
3. Analysis can be extended to cryogenic temperatures, as there are many applications at this temperature.
4. Temperature effect on the orientation of crystals can be found.
5. Obtain relationship between the temperature and the rate of loading.

References

[1] Anil Gannepalli and Surya K. Mallapragada, (2002), Atomistic studies of defect nucleation during nanoindentation of Au(001), Physical Review B, **66** 104103.

[2] Bahr, D. F., Wilson, D.E., and Crowson, D.A, (1999), Energy considerations regarding yield Points during indentation, J. Mater. Res., **14**(6) 2269.

[3] Ben, D. Beake and James, F. Smith, (2002), High-temperature nanoindentation testing of fused silica and other materials, Philosophical Magazine A, **82**(10) 2179–2186.

[4] Bradby, J. E., Williams, J. S., and Swain, M. V., (2003), *In situ* electrical characterization of phase transformation in Si during indentation, Physical Review B, **67** 085205.

[5] Branagan, D J., Tang, Y L., Sergueeva, A V., and Mukherjee, A K., (2003), Low-Temperature superplasticity in a nanocomposite iron alloy derived from a metallic glass Nanotechnology **14** 1216-1222.

[6] Carrasco, E., Rodriguez de la fuente, O., Gonzalez, M. A., and Rojo, J. M., (2003), Dislocation cross slip and formation of terraces around nanoindentations in Au(001), Physical Review B, **68** 180102.

[7] Chung, Jen Lu., Bogy, D.B., (1994), International journal of solid structures, 0020-7683(94) 00194-4, 1759-1771.

[8] Corcoran, S. G., Colton, R. J., Lilleodden, E. T., and Gerberich, W. W., (1997), Anomalous Plastic deformation at surfaces: Nanoindentation of gold single crystals, Rapid Communications, Physical Review B, **55**(24) R16057.

[9] Cynthia L. Kelchner, Plimpton, S. J., and Hamilton, J. C., (1998), Dislocation nucleation and the Defect structure during surface indentation, Physics review-B, **58**(17).

[10] David Christopher, Roger Smith, and Asta Richter, (2001), Atomistic modeling of Nanoindentation in iron and silver, Nanotechnology, **12** 372-383.

[11] Dawn A. Bonnell, (2003), Materials in nanotechnology: New structures, new properties, new complexity, J. Vac. Sci. Technol. A, **21**(5) S194-S206

[12] De La Figuera, J., Pohl, K., Rodriguez de la Fuente, Schmid, A. K., Bartelt, N. C., Carter, C. B., and Hwang, R. Q., (2001), Direct observation of misfit dislocation glide on surfaces, Physical Review Letters, **86**(17) 3819.

[13] Feichtinger, D., Derlet, P. M., Van Swygenhoven, H., (2003), Atomistic simulations of spherical indentations in nanocrystalline gold, Physical Review B, **67** 024113.

[14] Fivel, M., Verdier, M., Canova, G., (1997), 3D simulation of a nanoindentation test at a mesoscopic scale, Materials science & Engineering, **A234-236** 923-926.

[15] Fraxedas, J., Garcia Manyes, S., Gorostiza, P., and Sanz, F., (2002), Nanoindentation: Toward the sensing of atomic interactions, PNAS, **99**(8) 5228-5232.

[16] Gerberich, W. W., Nelson, J. C., Lilleodden, E. T., Anderson, P., and Wyrobek, J. T., (1996), Indentation induced dislocation nucleation: The initial Yield Point, Acta mater., **44**(9) 3585-3598.

[17] Gouldstone, A., Koh, H. J., Zeng, K. Y., Giannakopoulos, A. E., and Suresh, S., (2000), discrete and continuous deformation during nanoindentation of thin films, Acta mater., **48**, 2277-2295.

[18] Hebbache, M., (2003), Nanoindentation: Depth dependence of silicon hardness studied within contact theory, Physical Review B, **68** 125310.

[19] High temperature NanoTesting, MICRO MATERIALS measuring nanotechnology - http://freespace.virgin.net/micro.materials/

[20] Ju Li, Krystyn J. Van Vliet, Ting Zhu, Sidney Yip, and Subra Suresh, (2002), Atomistic mechanisms governing elastic limit and incipient plasticity in crystals, Nature, **418**, 307-310.

[21] Kalia, R. K., Vashishta, P., Woodward, C., Rao, S. I., Kajihara, S., and Dimiduk, D. M., Computational Assisted Development of High temperature Structural Materials, www.hpcmo.hpc.mil/Htdocs/UGC/UGC98/papers/1c_chal/ .

[22] Kallman, Jeffrey S., De Groot, Anthony, J., Hoover, Carol G., Hoover, William G., Lee, Susanne M., and Wooten, Frederick., (1995), Visualization techniques for molecular dynamics, IEEE Computer Graphics and Applications, **15**(6) 72-77.

[23] Kiely, J. D., Jarausch, J. F., Houston, J.E., and Russell, P. E., (1999), Initial Stages of yield in Nanoindentation, Journal of material Research, **14**(6) 2219.

[24] Kim, J. -J., Choi, Y., Suresh, S., and Argon, A. S., (2002), Nanocrystallization during nanoindentation of a Bulk Amorphous metal alloy at Room temperature, Science, **295** 654-657.

[25] Komanduri, R., Chandrasekar, N., Raff, L. M., (2000), MD Simulation of indentation and Scratching of single crystal aluminum, WEAR, **240** 113-143.

[26] Krystyn J. Van Vliet, Ju Li, Ting Zhu, Sidney Yip, and Subra Suresh, (2033), Quantifying the early stages of plasticity through nanoscale experiments and simulation, Physical Review B, **67** 104105.

[27] Liang, H. Y., Woo, C. H., Hanchen Huang, Ngan, A. H.W., and Yu, T. X., (2003), Dislocation nucleation in the initial stage during nanoindentation, Philosophical Magazine, **83**(31–34) 3609–3622.

[28] Liang, H. Y., Woo, C. H., Hanchen Huang, (26-29 July 2004), Crystallographic Effects on Nano-plasticity on copper Surfaces, International Conference Computational and Experimental Engineering and Science, Madeire, Portugal.

[29] Liang, H. Y., Woo, C. H., Hanchen Huang, Ngan, A. H.W., and Yu, T. X., (2004), Crystalline plasticity on Copper (001), (110), and (111) Surfaces during nanoindentation, Computer Modeling in Engineering and Science (in press)

[30] Lorenz, D., Zeckzer, A., Hilpert, U., Grau, P., Johansen, H., and Leipner, H. S., (2003), Pop-in effect as homogeneous nucleation of dislocations during nanoindentation, Physical Review B, **67** 172101.

[31] Lu L., Sui M L., and Lu K., (2000), Superplastic extensibility of nanocrystalline copper at room temperature Science **287** 1463-6

[32] Mao S X., (2003) Indentation on nanocrystalline copper by AFM diamond tip, private communications

[33] Oliver, W.C. and Pharr, G.M, (1992), An improved technique for determining hardness and elastic modulus using load and displacement sensing indentation experiments, J. Mater. Res., 7(6) 1569.

[34] Reith, M., and Schommers, W., (2002), Computational Engineering of Metallic Nanostructures and Nanomachines, Journal of Nanoscience and Nanotechnology, **2**(6) 679-685.

[35] Richard P. Vinci, Stefanie A. Forrest, and John C. Bravman, (2002), Effect of interface conditions on yield behaviour of passivated copper thin films, J. Mater. Res., **17**(7) 1863-1870.

[36] Rodriguez de la fuente, O., Zimmerman, J. A., Gonzalez, M. A., de la Figuera, J., Hamilton, J. C., Woei Wu Pai, and Rojo, J. M., (2002), Dislocation emission around nanoindentations on a (001) FCC Metal Surface studied by scanning tunneling microscopy and atomistic Simulations, Phy. Rev. Let., **88**(3) 036101-1.

[37] Rodriguez de la fuente, O., Zimmerman, J. A., Gonzalez, M. A., de la Figuera, J., Hamilton, J. C., Woei Wu Pai, and Rojo, J. M., (2002), Dislocation emission around nanoindentations on a (001) FCC Metal Surface studied by scanning tunneling microscopy and atomistic Simulations, Phy. Rev. Let., 88(3) 036101-1.

[38] Roger Smith, Christopher, D., and Kenny, S. D., (2003), Defect generation and pileup of atoms during nanoindentation of Fe single crystals Phys. Rev. B, **67** 245405

[39] Shenderova, O., Mewkill, J., and Brenner, D. W., (2000), Nanoindentation as a probe of nanoscale residual stresses: Atomic simulation results, Molecular simulation, **25** 81-91.

[40] Smith, J. F and Zhang, S., (2000), High temperature nanoscale mechanical property measurements, Surface Engineering, **16**(2) 143-146.

[41] Suresh, S., Nieh, T.G., and Choi, B.W., (1999), Scripta Materiala, **41**(9) 951-957.

[42] Swain, M.V., and Mencik, J., (1994), Mechanical property characterization of thin films using spherical tipped indenters, Thin Solid Films, **253**(1-2) 204-211.

[43] Tokushi Kizuka, (1998), Atomic process of point contact in gold studied by time-resolved High Resolution transmission electron microscopy, Physical Review Letters, 81(20) 4448.

[44] Wang, Y. M. and Ma, E., (2003), Temperature and strain rate effects on the strength and ductility of nanostructured copper Appl. Phys. Lett., **83**(15) 3165.

[45] William W. Gerberich, Natalia I. Tymiak, and Donald E. Kramer, (2001), Mat. Res. Soc. Symp. Proc., **649**.

[46] Xavier Lafontan, Christophe Le Touze, Beatrice Wenk, Inna Kolesnik, Francis Pressecq, Guy Perez, Jean-Marc Nicot, Muriel Dardalhon and Sebastien Rigo, Environmental test bench for reliability studies: Influence of the temperature on RF switches with metallic membranes.

[47] Xiao Dong Zhang, (2003), Temperature dependence of the structure and mechanical properties of TI-SI-N coatings ME Graduate student Conference.

[48] Xin-Ling Ma and Wei Yang, (2003), Molecular dynamics simulation on burst and arrest of stacking faults in nanocrystalline Cu under nanoindentation Nanotechnology **14** 1208-1215.

[49] Yonenaga, I., Hoshi, T., and Usui, A., (2000), High Temperature hardness of Bulk Single Crystal GaN in comparison with other wide-gap materials J. Phys: Condens. Matter, **12** 10319-10323.

[50] Yongsheng Leng, Guiping yang, Yuanzhong Hu, and Linqing zheng, (2000), Computer experiments on the nanoindentation: A molecular dynamics approach to the elastoplastic contact of metal copper, Journal of Material Science, **35** 2061-2067.

[51] Yoonjoon Choi, Krystyn J. Van Vliet, Ju Li, and Subra Suresh, (2003), Size effects on the onset of plastic deformation during nanoindentation of thin films and patterned lines, J. Appl. Phys., **94**(9) 6050.

[52] Yu I. Golovin and Dub, S. N., (2003), Stepwise transition from elastic to elastoplastic deformation at the initial stage of nanoindentation, Doklady Phys.48 612-614.

[53] Zimmerman, J. A., Kelchner, C. L., Klein, P. A., Hamilton, J. C., Foiles, S. M., (2001), Surface Step effects on Nanoindentation, Phy.Rev.Let., **87**(16) 165507-1.

[54] Zou, Z. Q., Dong, Z. C., Trifonov, A. S., and Nejo, H., (2002), Atomistic resolution imaging of a single-crystal Cu (100) surface by scanning tunneling microscopy in ultrahigh vacuum at room temperature, J. Vac. Sci. Technol. B, **20**(4) 1567.